

**BINARIES IN THE FORMATION OF MULTIPLE
POPULATIONS**

BINARY-EJECTED ENRICHMENT FOR MULTIPLE POPULATIONS
IN GLOBULAR CLUSTERS

By MICHELLE NGUYEN, B.Sc.

A Thesis Submitted to the School of Graduate Studies in Partial Fulfillment
of the Requirements for
the Degree Master of Science

McMaster University © Copyright by Michelle Nguyen, August 2023

McMaster University

MASTER OF SCIENCE (2023)

Hamilton, Ontario, Canada (Physics & Astronomy)

TITLE: Binary-ejected enrichment for multiple populations in glob-
ular clusters

AUTHOR: Michelle Nguyen
B.Sc. (Astrophysics),
McMaster University, Hamilton, Canada

SUPERVISOR: Alison Sills

NUMBER OF PAGES: xiv, 193

Lay Abstract

The majority of stars form in star clusters. Globular clusters are the oldest and most massive type of star cluster. Formerly thought to be made of stars of the same age and chemical composition, nearly all observed globular clusters are now known to host multiple populations. About half of their stars form from similar material as isolated stars. The other half show signs of enrichment. How enriched stars get their enriching material is an open problem in cluster formation. Pairs of stars orbiting each other as binaries were proposed to eject the material needed to form these stars. We model 408 binaries to find that some systems eject large amounts of enrichment, especially when the stars are more massive. The rarity of these systems suggests binaries can explain the variations seen in multiple populations between clusters but cannot fully explain the large fraction of enriched stars seen.

Abstract

Globular clusters are not simple stellar populations. Practically all globular clusters show multiple populations (MPs), where at the same metallicity $[\text{Fe}/\text{H}]$, approximately half of their stars are enriched by the products of high-temperature hydrogen burning relative to the rest that show field-like abundances. The source of enrichment for forming the enriched population is an unresolved problem. Interacting massive binaries are an underexplored proposed source of enrichment. Many assessments of the theory are based on only one modelled binary. We simulate a suite of metal-intermediate, $[\text{Fe}/\text{H}] = -1.44$, interacting binaries with initial primary masses of $10 \leq M_1 \leq 40 M_\odot$, with mass ratios $0.15 \leq q \leq 0.9$, over periods ranging from about 2 to 700 days using MESA. Our simulations show that binaries at higher masses, higher mass ratios, and near our upper period limit tend to be the most enriching with ejecta showing HeNaCNOAlMg variations consistent with hot-H burning. Some binaries do not eject material, suggesting binary mass loss can contribute to the dilution of enrichment. As a realistic population, binaries within our parameter space eject about ten times as much mass as they would as single stars. Ejection occurs on timescales of about 11 Myr, consistent with observed and theoretical limits on the age spreads for MPs. Our systems are rare, making them more suited to explaining the stochastic nature of MPs but not the large fraction of enriched stars. Spreads in He, N, Na, C, and Al for our ejecta could reasonably explain the observed spreads in clusters. Reduced variation

in O and Mg suggests more massive binaries should be investigated. A multi-scale approach to cluster formation with multiple types of enrichment sources is a necessary next step for validating MP formation scenarios.

Acknowledgements

Thank you, Alison Sills, for your continued support and guidance over the years. For cultivating a welcoming environment and for providing the challenge I needed. It has truly been a pleasure to learn throughout this project, even when other bits of life were much less than so. I greatly appreciate the opportunity you have given me.

Thank you to my committee members, Doug Welch and Ryan Cloutier, for your input, advice, and perspectives.

Thanks to Claude Cournoyer-Cloutier, Jeremy Karam, and Marta Reina-Campos for your help and questions and feedback and more. To you and to my office-mates: may your futures be as kind and bright as you are (i.e. very).

To my family: if you are reading this, that's unsettling as this is meant to be a reminder to myself. Your support means the world to me.

We acknowledge the support of the Natural Sciences and Engineering Research Council of Canada (NSERC).

Table of Contents

Lay Abstract	iii
Abstract	iv
Acknowledgements	vi
Abbreviations	xiii
1 Introduction	1
1.1 Multiple populations	3
1.2 Formation theories of multiple populations	13
1.3 Binaries in context of multiple populations	19
1.4 This work	25
2 Methods	27
2.1 General overview	27
2.2 Physical prescriptions	30
2.3 Binary prescriptions	40
2.4 Parameter space for models	43
2.5 Simulations	45

3	Results	55
3.1	Yields of alpha-enhanced binaries	55
3.2	Expected yields from a binary population	91
3.3	Comparison with solar-scaled binary yields	101
3.4	Envelope ejection in alpha-enhanced binaries	105
4	Summary and discussion	112
4.1	Grids of binary models	113
4.2	Suitability of massive binaries as sources of enrichment	117
4.3	Caveats and additional considerations	125
4.4	Future work	127
A	Base inlists and files	131
B	Tables of runs	156
C	Probabilities over the interpolated parameter space	177

List of Figures

1.1	Colour-magnitude diagram of NGC 6752	5
1.2	Abundance correlations and anti-correlations in NGC 6752	8
1.3	Mass-age plane of clusters showing MPs	11
1.4	Abundances in NGC 104 (47 Tuc) compared to dilution models	23
2.1	Parameter space of all runs	48
2.2	Single star, solar-scaled stellar tracks	49
2.3	Single star, alpha-enhanced stellar tracks	50
2.4	Radius evolution of sample single star	52
3.1	Status of alpha-enhanced binary simulations	56
3.2	Relative enrichment of alpha-enhanced binary ejecta	57
3.3	Mass ejected in HeNaCNO for alpha-enhanced binaries	58
3.4	Enrichment as a function of the initial system mass lost, with initial primary mass	61
3.5	Enrichment as a function of the initial system mass lost, with initial mass ratio	62
3.6	Na-N and Na-O relations for alpha-enhanced binary ejecta	68
3.7	C-N and C-O relations for alpha-enhanced binary ejecta	69
3.8	Enrichment thresholds in sodium abundance	70

3.9	Initial primary mass distributions for enriching and non-enriching binaries .	72
3.10	Mass ratio distributions for enriching and non-enriching binaries	73
3.11	Initial period distributions for enriching and non-enriching binaries	74
3.12	Fractions of system mass lost for enriching and non-enriching binaries . . .	75
3.13	Time evolution of mass and Roche lobe filling for a sample binary	77
3.14	Onset of RLOF for initial primary mass and orbital period	78
3.15	Fraction of mass lost and sodium levels for different RLOF onset times . . .	79
3.16	Timescale distributions for enriching and non-enriching binaries	80
3.17	Helium enhancement compared to oxygen and sodium	82
3.18	Relationship between iron and helium enhancement	83
3.19	C+N+O abundance as a function of helium abundance	85
3.20	Sodium and lithium relationship in alpha-enhanced binary ejecta	86
3.21	Lithium abundance distributions for enriching and non-enriching binaries .	87
3.22	Lithium abundance distributions for more massive and less massive binaries	88
3.23	Al-N and Al-Mg relations for binary ejecta	90
3.24	Isotopic magnesium ratios as a function of helium abundance	91
3.25	Mass-binned probabilities over the cubic and interpolated parameter spaces	96
3.26	Percentiles, means, and extremes of abundances	97
3.27	Percentiles, means, and extremes of changes in abundances	98
3.28	Status of solar-scaled binary runs	102
3.29	Enrichment of solar-scaled binary runs	103
3.30	Na-N and Na-O relations for solar-scaled binary ejecta	104
3.31	Mass lost with and without additional envelope ejection	106
3.32	Na-N and Na-O relations with and without additional envelope ejection . .	107

3.33 O and Na relations with helium abundance with and without additional envelope ejection	107
3.34 Ejected mass considering maximum or no additional envelope ejections . .	109
3.35 Na-N and Na-O relations for maximum or no additional envelope ejections .	110
3.36 O and Na compared to helium abundance for maximum or no additional envelope ejections	110
3.37 Parameter space of binaries considered for envelope ejection calculations, with anomalies	111
C.1 Maps of the interpolated parameter space	178

List of Tables

2.1	Alpha-enhancement levels	33
3.1	Enrichments observed in alpha-enhanced binary models, for all tracked elements	66
3.2	Enrichment of Mg isotopes in binary ejecta	90
3.3	Percentiles, means, and extremes of abundances	98
3.4	Percentiles, means, and extremes of changes in abundances	99
B.1	List of the alpha-enhanced binaries	166
B.2	List of the solar-scaled binaries	176

Abbreviations

AGB	Asymptotic giant branch
APOGEE	Apache Point Observatory Galactic Evolution Experiment
BaSTI	A Bag of Stellar Tracks and Isochrones
CMD	Colour-magnitude diagram
CPM	Convective premixing
DSEP	Dartmouth Stellar Evolution Program
FRMS	Fast-rotating massive star
GC	Globular cluster
GMC	Giant molecular cloud
IMF	Initial mass function
IQR	Interquartile range
LTE	Local thermodynamic equilibrium
MESA	Modules for Experiments in Stellar Astrophysics

MIST	MESA Isochrones and Stellar Tracks
MLT	Mixing-length theory
MP	Multiple population
MS	Main sequence
NACRE	Nuclear Astrophysics Compilation of REaction rates
OC	Open cluster
RGB	Red giant branch
RLOF	Roche lobe overflow
SDSS	Sloan Digital Sky Survey
SMS	Supermassive star
SN	Supernova
SSP	Simple/single stellar population
VMS	Very massive star
YMC	Young massive cluster
ZAMS	Zero-age main sequence

Chapter 1

Introduction

Star clusters are the site of star formation and a building block in forming galaxies (Hopkins, 2012; Krause et al., 2020). Particularly evident with high mass stars, less than 10% of isolated or field stars possibly formed outside of a cluster (Hopkins, 2012; de Wit, W. J. et al., 2005; Chandar et al., 2017). Estimates of the fraction of galaxy stars forming in compact or gravitationally bound observed star clusters range from 10 ~ 80% (Adamo et al., 2020b; Chandar et al., 2017), though these values are subject to uncertainties (see Adamo et al., 2020a). Consistently, Lahén et al. (2020) find a range in the fraction of star formation in clusters to be 20% early in their simulated dwarf galaxy merger to 80% during the subsequent starburst.

Most generally, star clusters are spatial overdensities of stars (Krumholz et al., 2019). To make distinctions between stellar associations and star clusters, clusters are generally adopted as groups of more than 12 stars (Krause et al., 2020; Krumholz et al., 2019). A distinction at the more massive end of clusters from galaxies is that star clusters are not dominated by dark matter (Krause et al., 2020). Star clusters in the Milky Way are divided into two classifications: open and globular. In contrast to open clusters (OCs), which are

typically lower mass and tend to be younger, globular clusters (GCs) are as massive as roughly $10^7 M_{\odot}$ and can be nearly as old as the universe (Krumholz et al., 2019; Bastian & Lardo, 2018). Having formed near the earliest conditions of star formation to at least a few Gyr later, GCs serve as valuable tools for testing our understanding of the physical processes and histories of cluster formation and evolution (Krause et al., 2020). By extension, they also inform us of star formation and galaxy formation, existing as an active intersection of these scales.

The distinction between OCs and GCs is not definite, with the classes showing overlap in their properties (Cassisi & Salaris, 2020; Krumholz et al., 2019). For example, young massive clusters (YMCs) can be younger than ~ 100 Myr and more massive than $\sim 10^4 M_{\odot}$, overlapping in mass with most definitions of GCs (Krumholz et al., 2019). YMCs have been treated as part of the OCs, as precursors to GC(-like) objects, and as a separate class (Krumholz et al., 2019; Cai et al., 2019; Banerjee, 2021; Banerjee et al., 2020; Gvozdenko et al., 2022).

Globular clusters have been used to infer the hierarchical assembly history of galaxies, investigate the presence of galaxy interactions, and study the initial mass function (IMF) of stars (Monty et al., 2023; Koch & Côté, 2019; Deger et al., 2022; Buzzo et al., 2023; Baumgardt et al., 2023). This inference depends on assumptions about the stellar population of a cluster. In the past, globular clusters were thought of as simple/single stellar populations (SSPs), consisting of stars born from the same material at the same time (Bastian & Lardo, 2018). Both observations and simulations have disproved this model of globular clusters. GCs host stellar populations that show variations in age, metallicity, and chemical composition (Piotto, 2009; Milone & Marino, 2022; Li et al., 2017; Goudfrooij et al., 2017; Monty et al., 2023; Binks et al., 2022; McKenzie & Bekki, 2021; Brown & Gnedin, 2022).

Often, globular clusters are still treated as SSPs for simplicity, particularly for determining their ages and metallicities (e.g. Dickson et al., 2023; Adamo et al., 2023; Ying et al., 2023). Current approaches consider variations in age, metallicity, and rarely chemical abundances, through fitting multiple models of SSPs synthesized with different properties (e.g. Milone et al., 2023; Squicciarini et al., 2021; Cadelano et al., 2022; McKenzie & Bekki, 2021). Some of the major challenges in cluster formation and evolution theory are in explaining the origins of these deviations from the SSP model, compelling constraints from both observations and models. A more complete understanding of the intricacies of globular clusters informs the insight they provide on other scales of astrophysics.

1.1 Multiple populations

We focus on the complexity of globular clusters referred to as multiple populations (MPs), which has remained unresolved for decades (Bastian & Lardo, 2018; Jang et al., 2022). Nearly all globular clusters show star-to-star chemical variations, apparent both in photometry and spectroscopy (e.g. Milone et al., 2017; Salgado et al., 2022). Photometric differences can be apparent as a spread of stars in three-band combination colour-magnitude diagrams (CMDs) (Bastian & Lardo, 2018).

Colours, as in standard CMDs, are generally the difference in magnitudes measured in two different bands (Sekiguchi & Fukugita, 2000). Measured magnitudes, m , correspond to the flux, F , that passes through a given wavelength filter (band)

$$m \propto -2.5 \log F. \tag{1.1.1}$$

These are often corrected for extrinsic effects like reddening from foreground dust absorption

and re-emission of the spectra, and the zero point from the instruments used. As the overall spectrum of a star follows a blackbody curve of an effective temperature, alongside composition-dependent emission and absorption features, various magnitude differences can return details about the sources of these effects: surface temperature, metallicity, gravity, and chemical composition (Jang et al., 2022; Sekiguchi & Fukugita, 2000; Cassisi & Salaris, 2020; Bruzual & Charlot, 2003; Ramírez & Meléndez, 2005). Careful analysis of photometry can reveal diverse properties of the star.

The position of stars on CMDs depends primarily on their mass and evolutionary phase as stars move throughout the CMD during their lifetime on stellar tracks (e.g. Choi et al., 2016).

Some three (or higher number) colour combinations make light-element abundance variations apparent (Bastian & Lardo, 2018). These colour combinations are sometimes referred to as pseudo-colour combinations as unlike typical two-band colours, they do not directly characterize the apparent colour of the star. An example is colour in (U,B,I) computed as $(U - B) - (B - I)$, a difference of two typical colours, which is sensitive to nitrogen abundance (Jang et al., 2022). This index applies to RGB stars where the sensitivity of $(U - B)$ of light element abundances and $(B - I)$ to helium abundance leads to the difference $(U - B) - (B - I)$ varying mostly with nitrogen (Monelli et al., 2013). Figure 1.1 shows the CMD of stars in NGC 6752. Highlighted as large, coloured points are stars showing splitting in their $(U - B) - (B - I)$ colour.

Different multi-band colours are sensitive to different elements and may depend on the mass or evolutionary phase of the stars being measured (Jang et al., 2022). These spreads in photometry are generally corroborated by direct spectroscopic measurements of light elements (Bastian & Lardo, 2018; Milone & Marino, 2022).

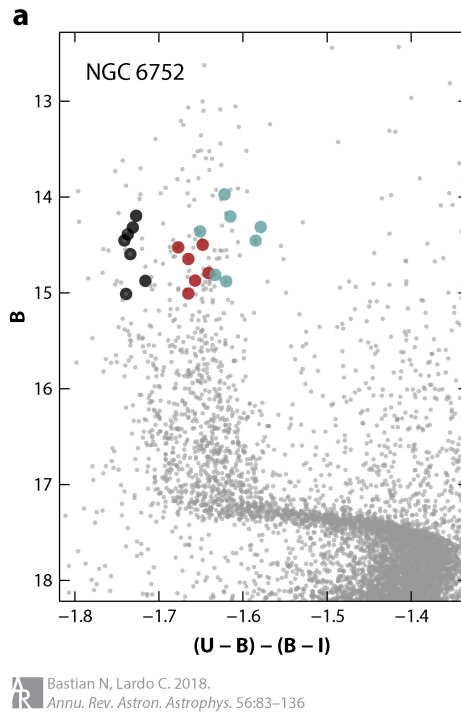


Figure 1.1: Reproduction of figure 1a from Bastian & Lardo (2018), permission requested through Annu. Rev. Colour-magnitude diagram of stars in the globular cluster NGC 6752, which hosts MPs. The colour on the x-axis is the three-colour combination $C_{U,B,I}$. Magnitude is shown in the B-band. RGB stars in this cluster are highlighted as large coloured points. Photometry plotted by Bastian & Lardo (2018) was provided by Peter Stetson.

1.1.1 Abundance anomalies in multiple populations

Cluster stars fall roughly equally into two groups based on these abundance differences, forming MPs (Bastian & Lardo, 2018). One group of stars is similar in composition to field stars of the same metallicity (Bastian & Lardo, 2018). $[\text{Fe}/\text{H}]$ refers to the relative abundance of iron to hydrogen where for N_X being the number of atoms/ions of species X, and subscript \odot indicates the abundance in the Sun

$$[\text{Fe}/\text{H}] = \log_{10} \left(\frac{N_{\text{Fe}}/N_{\text{Fe},\odot}}{N_{\text{H}}/N_{\text{H},\odot}} \right). \quad (1.1.2)$$

The other group is chemically anomalous, typically with enhanced levels of He, N, Na and depleted C, and O (Bastian & Lardo, 2018). He abundances are only measured directly in cool stars, requiring complex corrections, and are otherwise inferred from photometry and stellar evolution models (Carretta & Bragaglia, 2021; Bastian & Lardo, 2018). We refer to the anomalous class of cluster stars as the enriched population. Additionally, these elements show correlations and anti-correlations in their abundances such as N-Na correlation and Na-O anti-correlation (Bastian & Lardo, 2018). The detection of these relationships has been considered synonymous with the detection of MPs (Carretta et al., 2015). These (anti-)correlations appear due to the nature of the reactions involved in producing or destroying their constituents, such as the CNO-cycle and the NeNa chain (Bastian & Lardo, 2018).

Essentially, enriched population abundance anomalies are consistent with the products of high-temperature H burning, occurring at $T \gtrsim 40 - 50 \times 10^6$ K for the commonly observed abundance trends (Bastian & Lardo, 2018; Langer et al., 1993; Adelberger et al., 2011).

We refer to the presence of these products in excess as enrichment, although some elements are depleted and others are enhanced. Conditions are met in the core of massive

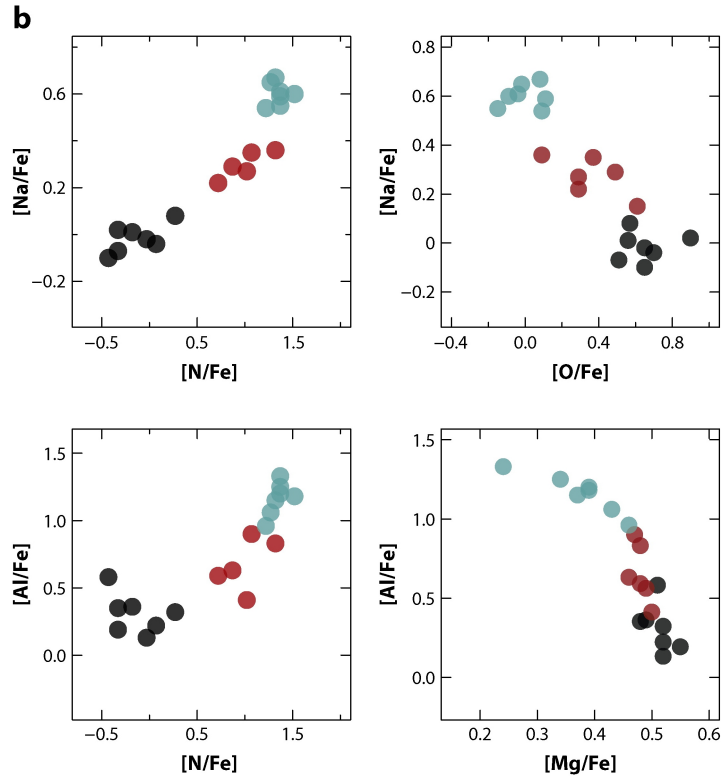
stars ($\gtrsim 8 M_{\odot}$) or at the bottom of the convective envelope of asymptotic giant branch (AGB) stars ($3\sim 8 M_{\odot}$) (Gratton et al., 2019). The pressure of massive stars allows sufficient temperatures to be reached in their cores during their main sequence (MS). The asymptotic giant branch is an evolutionary phase of intermediate-mass stars, past their core-H burning main sequence, and past the burning of H in an inner shell, where an outer hydrogen shell burning occurs with an inner He burning shell (Carroll & Ostlie, 2017). The H-burning shell absorbs energy from the inner layer, raising its temperature.

For MP-hosting clusters exhibiting multi-modal [Fe/H] distributions, an enriched and an unenriched population are present at each metallicity (Gratton et al., 2019; Johnson et al., 2015).

Al, Si, K, Ca, Sc enhancement and Mg depletion, have sometimes been observed in enriched populations (Carretta & Bragaglia, 2021; Bastian & Lardo, 2018). Some of these heavier element variations may only be observed in a smaller fraction of stars in the GCs (Gratton et al., 2019). Occasionally Al-Mg, and rarely Si-F, anti-correlation have also been observed (Gratton et al., 2019; Cassisi & Salaris, 2020). The Al and Mg variations are associated with the AlMg chain reactions. These require higher activation temperatures $\gtrsim 70 \times 10^6 \text{K}$.

In figure 1.2 we show the light element abundance variations for the RGB stars of NGC 6752, shown in figure 1.1. These stars exhibit positive Na-N and Al-N correlations alongside anti-correlated Na-O and Al-Mg. The least enriched stars are shown as black points, having low [Na/Fe] and [Al/Fe], while the most enriched stars are in turquoise. The group of red points shows intermediate enrichment.

Enriched material is present in low-mass stellar interiors for clusters with MPs, where they cannot be produced (Bastian & Lardo, 2018). Generally, members of the enriched




 Bastian N, Lardo C. 2018.
Annu. Rev. Astron. Astrophys. 56:83–136

Figure 1.2: Reproduction of figure 1b from Bastian & Lardo (2018), permission requested through *Annu. Rev.* Correlations and anti-correlations of abundances of RGB stars in the globular cluster NGC 6752, which hosts MPs. The same stars highlighted in figure 1.1 are shown. Spectroscopic measurements plotted by Bastian & Lardo (2018) are from Yong et al. (2005) and Yong et al. (2015). The photometric spreads seen in figure 1.1 directly correspond to abundance spreads in light elements.

population and the unenriched population exist throughout the CMD, i.e. for stars of different masses (Bastian & Lardo, 2018; Milone & Marino, 2022). As such, abundance variations cannot be explained by the mixing of evolutionary material bringing hot-H burning products from the core to the surface of the star. This suggests that stars in enriched populations formed out of gas previously enriched by other sources.

Some clusters show variations in even heavier elements, known as neutron capture elements with atomic numbers $Z > 30$ (Molero et al., 2023). Neutron capture refers to nuclear reactions where a heavier nucleus “absorbs” a neutron going up in atomic number. These can be produced through rapid-neutron capture (*r*-process) or slow-neutron capture (*s*-process). The *r*-process contrasts to *s*-process as it happens more rapidly than the associated decay (Schiappacasse-Ulloa & Lucatello, 2023). Neutron capture requires higher energies/temperatures than the production of aforementioned elements (He, N, Na, O, etc.), though *s*-process elements could be produced in AGB stars and massive stars, with each producing different components (Magrini et al., 2018; Pignatari et al., 2010). Determining the cross-sections of the relevant reactions is an active field (e.g. Dietz et al., 2023; Skowronski et al., 2023; Erbacher et al., 2023). Nucleosynthesis of *r*-process elements is an extremely uncertain process but is associated with binary neutron star mergers more recently, as well as Type II supernovae (SNe) (Kullmann et al., 2023; Magrini et al., 2018). Ratios of neutron capture elements have been proposed as an avenue for discerning the sources of enrichment for MPs (Rain et al., 2019; Muñoz et al., 2018). However, due to the uncertainties in some of these reaction rates and the relative rarity of observations, we suggest matching light-element abundance variations to be the main requirement for an enrichment source, with neutron capture elements a future concern.

Several clusters hosting MPs also show variation in Li abundance, which is readily

destroyed at the high temperatures reached by an enriching source that impacts N, Na, and Al, for example (Bastian & Lardo, 2018). Its fragility above $\sim 2.5 \times 10^6$ K, with dependence on age and mass, makes it a potentially valuable constraint for determining the chemical enrichment sources of MPs (Randich & Magrini, 2021; D’Antona & Ventura, 2010). It is not consistent from cluster to cluster if the unenriched stars or the enriched stars have higher Li abundances (Milone & Marino, 2022). Many clusters show similar Li abundance between both populations (Bastian & Lardo, 2018). AGB stars could potentially produce Li through the Cameron-Fowler mechanism to counteract the Li depletion, which is not expected for more massive stars (Bastian & Lardo, 2018; Milone & Marino, 2022; Cameron & Fowler, 1971). The Cameron-Fowler mechanism refers to the mixing of the entire envelope outside of the He-burning shell induced by flashes of He-shell burning (Cameron & Fowler, 1971).

1.1.2 Characteristics of MPs and their hosts

Some observational studies indicate that there may be “discrete” sub-populations in MPs in globular clusters (e.g. Simpson et al., 2012; D’Antona et al., 2022). However, we note that Valle et al. (2022) used three robust clustering methods on RGB measurements of NGC 2808 to determine the number of populations hosted. They found that only two groups, one at the enriched end and one at the unenriched end, were the best fit. As Valle et al. (2022) describe, this is in contrast to previous publications which often relied on by-eye judgments of distributions showing “substructure”. Where statistical clustering methods were used, Valle et al. (2022) note these works would typically fail to account for uncertainties and optimization in the grouping. Given a lack of demonstrable robustness of MPs containing discrete sub-populations, beyond a group of unenriched and enriched stars, we do not consider “discreteness” of enrichment to be a necessity of an enrichment source.

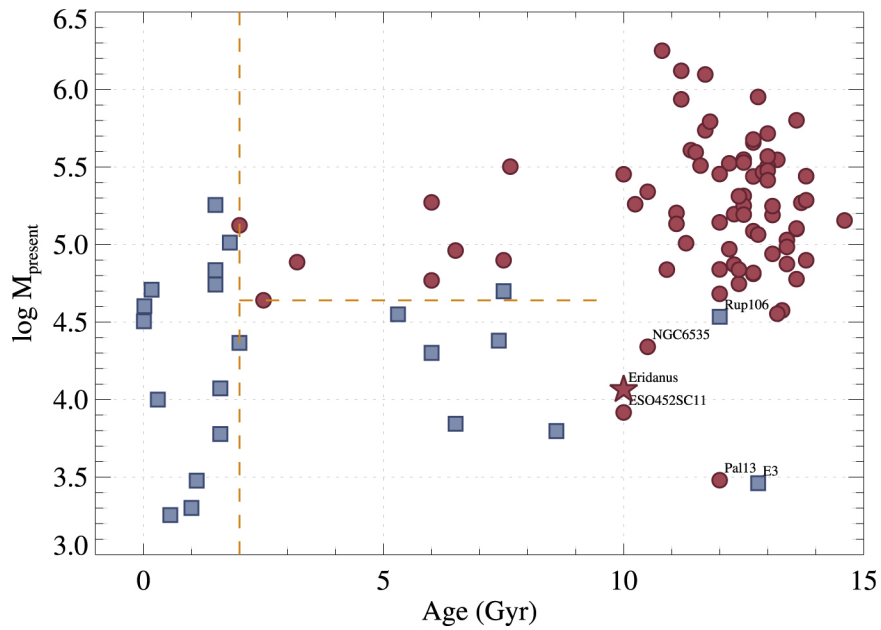


Figure 1.3: Reproduction of figure 7 from Wang et al. (2023), showing the present-day mass and age of clusters where MPs have (red circles and star) and have not been detected (blue squares). The figure has been reproduced under the terms of CC 4.0 (<https://creativecommons.org/licenses/by/4.0/>).

The presence of MPs is used to distinguish globular clusters from open clusters due to their ubiquity in the massive and old observed clusters (Bastian & Lardo, 2018; Gratton et al., 2019). These light abundance spreads are not typically seen in young open clusters (Bastian & Lardo, 2018). Some exceptions to this rule include the young cluster NGC 1783 (1.5 Gyr), and the low-mass clusters Palomar 13 and Eridanus (Cadelano et al., 2022; Tang et al., 2021; Wang et al., 2023). Neither the limit in cluster age nor cluster mass for where MPs are observed are sharp (Carretta & Bragaglia, 2021; Gratton et al., 2019). We share a figure from Wang et al. (2023) in figure 1.3 to show how this is the case. This suggests that GC formation follows a common pathway, both in the early and late universe and links present-day YMCs to old GCs (Forbes et al., 2018).

As their name suggests, GCs were named for their globular appearance in the sky, where their old age and mass leads to a relaxed, gravitationally bound system. Nonetheless, it has been suggested that the presence of MPs be the qualifier of a star cluster as a GC rather than age and mass (Milone & Marino, 2022; Gratton et al., 2019). This would alter the range of what a GC is to lower ages at the high mass end and to lower masses at the older end of the typical classification of a GC, blurring the distinction between OCs and GCs (Li et al., 2019; Bastian & Lardo, 2018; Gratton et al., 2019). A lack of clear distinction may be warranted if the formation process of MPs is universal. Clusters are increasingly treated as a continuum rather than having distinct classifications (Bastian & Pfeffer, 2022, see introduction). As such, a complete understanding of MPs and how they arise in different cluster environments is paramount to the field of cluster formation.

1.2 Formation theories of multiple populations

Currently, our understanding of the formation of the MPs is unsettled (see Bastian & Lardo, 2018). Within a cluster, chemical variations associated with MPs are present at the same $[\text{Fe}/\text{H}]$ and their populations show no (large) age spread and are present throughout the entire CMD (Gratton et al., 2019; Bastian & Lardo, 2018). If multiple populations were to arise from mergers of different clusters, significant age spreads and metallicity spreads are expected, particularly if they arise from progenitors with different chemical evolution histories (e.g. McKenzie & Bekki, 2018). Similarly, enrichment from SNe is expected to cause variations in the iron abundances (Wirth et al., 2021). If the SNe resulted from the unenriched population: an age difference between populations is also expected. The depletion of O observed is also inconsistent with the enrichment of MPs arising from SN nucleosynthesis, as SNe would enhance $[\text{O}/\text{Fe}]$ above the levels seen (Gratton et al., 2019). This favours the self-enrichment scenario where objects within the cluster enrich gas that goes on to form an enriched population (Bastian & Lardo, 2018). These objects are referred to as polluters and they must undergo high-temperature H-burning before releasing this material into the cluster (Schiappacasse-Ulloa & Lucatello, 2023). He-burning (or more advanced burning) must not have processed the enriching material, since this would deplete He and enhance O and C, destroying the observed abundance trends. The enriched population in these scenarios are often treated as distinct generations of stars whereby the enriched population arises as a second generation out of material released by the first, unenriched, population (e.g. Lahén et al., 2023; Renzini et al., 2022; Huerta-Martinez et al., 2023).

1.2.1 Age differences between enriched and unenriched populations

Current observations seem at odds with the idea that MPs correspond to distinct generations separated by more than $10 \sim 20$ Myr (Gratton et al., 2019; Bastian & Lardo, 2018). Measured age differences between unenriched and enriched populations are consistent (within one σ) with the clusters being coeval. Two recently studied examples are NGC 2121 (-6 ± 12 Myr) and NGC 1978 (1 ± 20 Myr) (Saracino et al., 2020; Martocchia et al., 2018). Comparisons between unenriched and enriched population ages may be complicated by the He enhancement seen in the enriched population, though not all observations are sensitive to this difference (Saracino et al., 2020). Higher He abundances usually lead to faster evolution which may be degenerate with an age difference between populations (Oliveira et al., 2020). The level of degeneracy varies, but we note that a helium spread of 0.003 in NGC 6717 changes the estimated age difference from 0.7 Gyr to 0.3 Gyr for Oliveira et al. (2020). The abundances of C, N, and O also impact stellar evolution and the age estimates of stellar populations (see, e.g. VandenBerg, 2023). In particular, He enhancement at moderate or higher levels is suggested to lead to skipping of the AGB in intermediate-mass stars, both by observations and theory (Lapenna et al., 2016; Charbonnel et al., 2013; Chantreau et al., 2016). MP property measurements, such as enriched population fraction or ages, in the AGB stars may not be representative of the properties seen in other phases or of the underlying initial properties of MPs. Determining age differences in older clusters $\gtrsim 10$ Gyr is subject to intrinsic errors of ~ 500 Myr, but values are also consistent, within uncertainty, of the populations being coeval (Oliveira et al., 2020).

In this work, we do not assume that the enriched stars are a subsequent generation of unenriched stars. However, we do consider the implications this assumption or the assumption that the populations are coeval would have for our results.

1.2.2 The mass budget problem

One of the unresolved issues is obtaining enough enriched gas to produce the enriched population, which can make up 40~90% of the total cluster (Carretta & Bragaglia, 2021; Winter & Clarke, 2023). This issue is referred to as the mass budget problem. A generous estimate of the initial amount of the required enriched star mass produced by intermediate-mass stars, in the AGB range, is roughly 5% (Bastian & Lardo, 2018). Winds of single, fast-rotating massive stars (FRMS) are also estimated to have a similar contribution (Bastian & Lardo, 2018). The contention may be partly alleviated by the initial mass function (IMF) differing in the past and by depletion of unenriched stars (Bastian & Lardo, 2018; Baumgardt et al., 2023). Results from (Baumgardt et al., 2023) suggest a factor of two increase in massive stars relative to low-mass stars is possible. Observations and cosmological zoom-in simulations suggest that GCs form with at most 4 ~ 5 times the mass they are today (Bastian & Lardo, 2018; Reina-Campos et al., 2018). It is not expected that this purely affects unenriched stars, so Cabrera-Ziri et al. (2015) suggest at least a factor of 30 increase in the initial enriched fraction predicted by AGB pollution is necessary. Models of galaxy evolution and constraints from observations do not support the extreme losses or preferences for forming polluters required for fully reconciling these predicted initial enriched fractions with the fractions observed in clusters today.

Generally, MP formation theories invoke mixing or dilution of enriched yields with primordial gas (Bastian & Lardo, 2018). This generally means that enrichment takes place before significant gas is lost from the cluster through SN, introducing constraints from cluster formation (Gratton et al., 2019). To be consistent with the observed abundance ratios in clusters exhibiting metallicity spreads (particularly ω Cen), core-collapse SNe that result from the evolution of massive stars is preferred as the constraint (Renzini, 2008). The

first core-collapse SNe may be expected to occur about 3 ~ 8 Myr after the birth of the first stars (Bastian & Lardo, 2018; Wirth et al., 2021). SNe will alter the [Fe/H] of the remaining gas, contributing to a metallicity spread (Renzini, 2008; Jiménez et al., 2021). As not all GCs with MPs have observed metallicity spreads, especially between their populations, enrichment must be possible before the first SNe (Bastian & Lardo, 2018). We note that estimates of the timing of the first core-collapse SNe depend on single 1d stellar evolution models. However, models of binary stars predict longer lifetimes before SNe (Eldridge et al., 2013). It is also expected that 3d magneto-hydrodynamical simulations are needed to capture the physics in the late evolution of massive stars and the SN explosion (Rizzuti et al., 2023; Keller & Kruijssen, 2022). Observational estimates of the time before the first core-collapse SNe are relatively uncertain (e.g. Castrillo et al., 2021).

1.2.3 Properties of multiple populations in different clusters

The properties of MPs vary from cluster to cluster, with some trends appearing based on global properties such as cluster mass or cluster age (Bastian & Lardo, 2018). In particular, both the width of the abundance spreads and the fraction of stars part of the enriched population tend to increase with cluster mass and age (Milone & Marino, 2022). Helium spreads for a sample of 57 GCs were determined by Milone et al. (2018), who found these spreads were largely correlated with cluster mass and properties that scale with cluster mass. Comparisons of clusters also seem to exhibit different levels of enrichment in different elements in their MPs (Bastian & Lardo, 2018). This has led to the naming of MP-sensitive photometric pseudocolour-colour diagrams as “chromosome maps” as they are characteristic to their cluster and are only partly characterized by properties like cluster metallicity (e.g. Jang et al., 2022). Spreads of abundance (anti-)correlations in MPs can

be described by the interquartile range (IQR) of their abundances in stars (Carretta, 2019). This refers to the range between the 25th and 75th percentile. Accounting for variation with the total absolute magnitude, concentration, and horizontal branch properties of the cluster, Carretta (2019) still finds a cluster-to-cluster variation of the IQR. Thus, the formation mechanisms of MPs must be both stochastic and dependent on their host environment.

1.2.4 Enrichment sources

The predominant theories invoke mass loss from massive stars or AGB winds (Bastian & Lardo, 2018). Of the theories involving massive stars, FRMS and very massive stars (VMS, $10^2 M_{\odot} \lesssim M$) or supermassive stars (SMS, $10^3 M_{\odot} \lesssim M$) have been frequently considered.

FRMS rely on the mixing and increased mass loss through winds that are induced by rotation to act as an enrichment source (Decressin et al., 2007a). The mixing from rotation helps bring up hot-H burning products to the surface of the star, where they can be ejected (Decressin et al., 2007a). VMS and SMS can have extreme mass loss rates due to their high luminosities (Bastian & Lardo, 2018).

Single sources of enrichment fail to reproduce the required total mass and abundance trends (Bastian & Lardo, 2018). For example, both AGB stars and FRMS are estimated to eject $\lesssim 10\%$ of the mass required for the enriched population as discussed earlier (Bastian & Lardo, 2018; de Mink et al., 2009). A major concern with enrichment through AGB stars is that this requires a delay of ~ 30 Myr before they enrich the cluster (Bastian & Lardo, 2018). As their enrichment has a positive Na-O correlation, dilution is necessary to reproduce the observed anti-correlation (Bastian & Lardo, 2018). As SNe and massive star evolution and winds take place prior to AGB enrichment, the gas from these sources must be ejected to prevent a metallicity spread. Gas of the same abundances as unenriched stars

must be accreted by the cluster after AGBs have released enriched material. In contrast to models invoking massive stars, it is not clear that dilution will easily take place since it depends on a timed accretion of gas (Bastian & Lardo, 2018). The timing of star formation from AGB products also subjects it to SNe feedback, worsening the mass-budget problem for AGB enrichment (Bekki, 2017).

AGB and FRMS yields may not produce the Al-Mg anti-correlation seen in some clusters. Decressin et al. (2007a) find that the required reaction is only reached near the end of the MS in their model and require an increase in the reaction cross-section at lower temperatures to explain an Al-Mg anti-correlation. AGB yields may produce the anti-correlation as they reach sufficient temperatures, but overall yields of AGB stars are sensitive to uncertain mixing physics (Bastian & Lardo, 2018; D’Antona & Ventura, 2010; Decressin et al., 2009; Bastian et al., 2015).

Recently, supermassive stars have been proposed as sources of enrichment in a new scheme by Gieles et al. (2018). In their scenario, SMS can form over a range of metallicities through stellar collisions as the GC accretes mass during its early phases. In large enough clusters, an SMS with sufficient mass to undergo the MgAl reactions at ZAMS can form, creating the observed Al-Mg relations that other sources of enrichment fail to explain. Constant accretion of fuel for hot-H burning and full convection is necessary to alleviate the mass budget and limit products to the early MS phase, in what they call the ‘conveyor belt’ mechanism. If this mechanism works for a few Myr, the mass budget problem could be alleviated and the enriched population would be coeval with the unenriched population. Additional constraints are needed from both observations and theoretical work to determine how feasible SMS are as enrichment sources. In particular, the existence of SMS is speculative (Bastian & Lardo, 2018).

Formerly, SMS without the ‘conveyor belt’ were predicted to undergo hot-H burning for a limited amount of time to prevent overproduction of He (Bastian & Lardo, 2018). This limited the mass that could be produced by SMS for enrichment.

1.3 Binaries in context of multiple populations

Another scheme of self-enrichment, proposed by de Mink et al. (2009), relies on close, interacting, massive binaries as a source of enriching material. From their simulation of a binary with initial masses of 20 and 15 M_{\odot} and an initial period of 12 days, ejected slow winds from the system qualitatively matched abundance anomalies of enrichment. Namely, the winds had enhanced He, N, Na, and Al alongside depleted C and O. Extrapolating from their system and under the generous assumption that all massive stars are part of an interacting binary, their expected contribution from binary ejecta was larger than that of AGB stars and FRMS combined ($\sim 13\%$ of initial cluster stellar mass).

Their model used binary evolution code described by Petrovic et al. (2005) and Yoon et al. (2006) for modelling self-consistent mass transfer. They adopted the same initial composition and the same reaction rates as Decressin et al. (2007a) and find that similarly to the FRMS and other massive star-based models, their binary fails to reproduce the correct Mg and Al abundance spreads. de Mink et al. (2009) suggest this can be resolved with more massive or wider binaries, where mass transfer would occur at later stages where the MgAl reactions would have taken place.

1.3.1 Binary mass transfer

The mechanism of enrichment through massive interacting binaries relies on the effects of non-conservative mass transfer. In a binary star system, the initially more massive primary star can interact with the secondary when in a close enough orbit. Evolution pushes its radius beyond the equipotential surface, the Roche lobe, leading to mass being accreted onto the secondary (Eggleton, 1983). This is referred to as Roche lobe overflow (RLOF). The mass transfer also involves an accretion of angular momentum, causing the secondary to spin up. As the secondary spins faster, accretion becomes less and less efficient as the secondary would break up with faster rotation (Paxton et al., 2019; de Mink et al., 2009). If the primary continues RLOF, then the additional mass gets ejected out of the system, often either as a jet or part of a circumbinary toroid (Lu et al., 2023). The resulting winds are slow enough to be expected to stay within the cluster for future star formation (de Mink et al., 2009). A large portion of RLOF is expected to be ejected from the system, particularly in wide and massive systems, and possibly with lower mass ratios $q = M_2/M_1 \leq 1$ (Petrovic et al., 2005; Shao & Li, 2016; Sen et al., 2022). These systems will also tend to undergo mass transfer at a later evolutionary stage, so enrichment products (particularly heavier ones) can more readily be ejected (de Mink et al., 2009). The combination of rotation of the primary from tidal interactions and accretion of the outer layers of the primary by the secondary can preferentially select enriched material that would otherwise remain in deeper layers (de Mink et al., 2009). A binary may undergo multiple phases of mass transfer during its lifetime, as was the case for the binary simulated by de Mink et al. (2009). As mass transfer impacts the subsequent evolution of the stars, yields can deviate from what may be expected from single-star evolution (Farmer et al., 2023, 2021). This may contribute to the stochasticity of enrichment from interacting massive binaries.

1.3.2 Potentially significant contribution from binaries

Perhaps the greatest advantage of interacting binaries as an enrichment source is in the context of the mass budget problem, as de Mink et al. (2009) suggest a larger contribution of mass from massive binary ejecta compared to AGB and FRMS yields is possible. Binaries constitute over half the stars in young clusters, although this is not the case in present-day GCs Gratton et al. (2019); Portegies Zwart et al. (2010). If YMCs are treated as analogous to the progenitors of GCs it is expected that early-on GCs hosted a considerable binary population. Dynamical interactions may have led to their disruption over time, however, the existence of binaries in clusters has major implications for cluster formation and evolution. Primordial binaries have been shown to impact the dynamical properties of the cluster over time (e.g. Wang et al., 2022). Populations of binaries also form readily through the dynamical interactions within young star clusters (Cournoyer-Cloutier et al., 2021; Torniamenti et al., 2021). Considering binaries in spectra and stellar population synthesis, particularly in young and intermediate-age clusters, provides better matches to observations (Eldridge & Stanway, 2009; Rui et al., 2021; Milone et al., 2012a). The evolution of binaries including the effects of mass transfer has demonstrable effects on synthetic stellar populations and their CMDs (Wang et al., 2020).

Over 90% of O ($\gtrsim 16M_{\odot}$) and B-type (M_{\odot}) primary stars are in binaries or higher order multiples and are more likely than low-mass stars to be part of close binaries (Offner et al., 2023; Duchêne & Kraus, 2013). At least one phase of mass transfer is expected for the majority of massive stars (Sana et al., 2012; Sana, 2022). As such, the massive stars that are expected to be contributors to enrichment are likely to be part of interacting multiple systems. This is especially supported by dynamical interactions in the dense environment of clusters acting to tighten and create binaries (Heggie, 1975). Non-conservative mass transfer

is an effective mechanism for ejecting the enriched envelope of the primary compared to single stars, particularly at the high-mass end (e.g. Farmer et al., 2021).

1.3.3 Modelling multiple populations with binary yields

Implementing a sub-grid model of continuous enrichment based on the yields from de Mink et al. (2009), 3d radiative hydrodynamical simulations of YMC formation by Howard et al. (2019) produced realistic He spreads. As Howard et al. (2019) find enriched and unenriched stars form (nearly) simultaneously within a giant molecular cloud (GMC) acting as a gas reservoir, with the early ejection of enrichment from interacting massive binaries, their scheme agrees with the (nearly) coeval populations and avoids the mass-budget problem.

Bastian et al. (2015) considered the Na-O abundance trends that could be produced by modelled enrichment source yields with dilution by primordial material. We present a figure from their work showing a comparison to the cluster NGC 104 in figure 1.4. The comparisons included AGB stars (based on Ventura et al., 2013; D’Ercole et al., 2010; Doherty et al., 2014), FRMS (Decressin et al., 2007b), and interacting binaries (de Mink et al., 2009). They suggest binaries match the expected He spread best for the required Na-O spread, but note that all yields lead to higher He spreads than generally observed. The mass fraction of helium Y had a predicted spread of $\Delta Y \sim 0.03$, though many clusters have smaller $\Delta Y \sim 0.01$. Based on the yields of de Mink et al. (2009), however, Bastian et al. (2015) consider the spread in $[O/Fe]$ to be too narrow for the spread in $[Na/Fe]$ to match observations. We note that some clusters exhibit narrower spreads in $[O/Fe]$ (e.g. Muñoz et al., 2020) than the ones considered by Bastian et al. (2015).

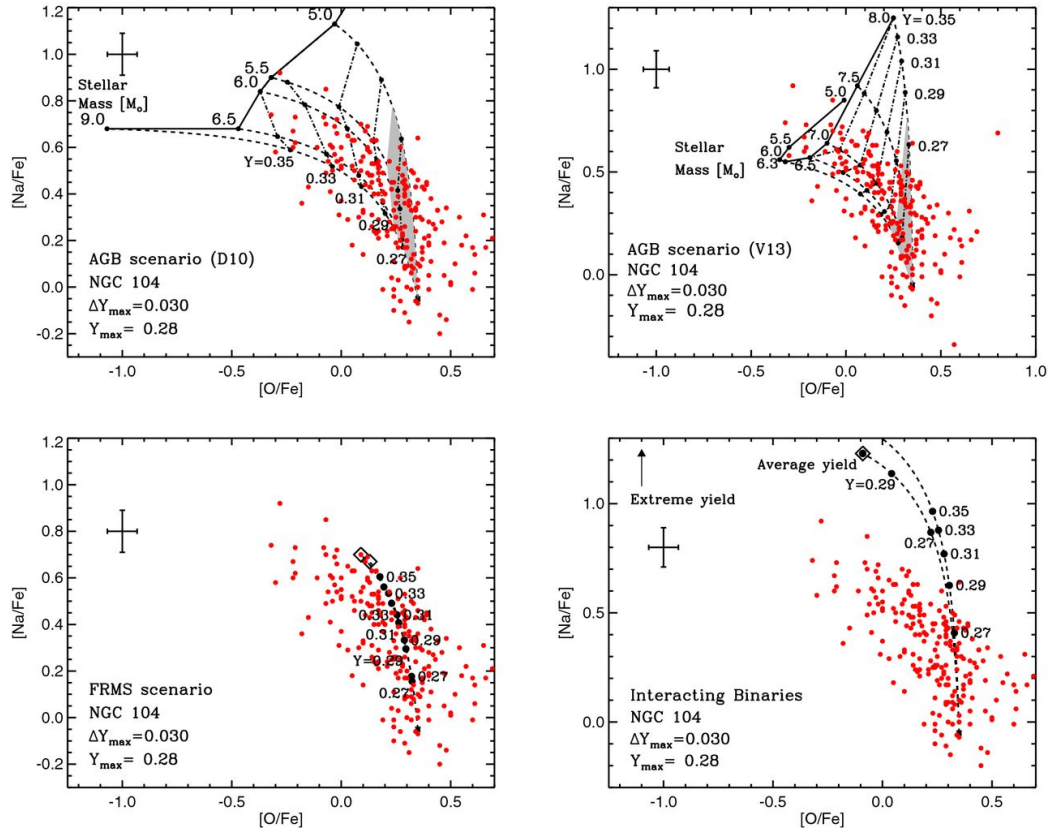


Figure 1.4: Reproduction of figure 1 from Bastian et al. (2015), reproduced according to MNRAS policies. Comparisons of the abundances observed in NGC 104 (47 Tuc, red points) from Roediger et al. (2014); di Criscienzo et al. (2010); Milone et al. (2012b) and Gratton et al. (2013) to models. Solid lines for the top panels and diamonds for the bottom panels show the predicted yields from models. The dashed lines indicate the effect of dilution and dashed-dotted lines indicate constant helium mass fraction Y . Black points and their annotations indicate the Y of the material. For the top two panels, a grey-shaded region indicates the material with He abundances matching the maximum spread observed in NGC 104. Each panel uses yields from a different source, (for the AGB, D10, D’Ercole et al., 2010 and V13, Ventura et al., 2013; for FRMS, Decressin et al., 2007a; for interacting binaries, de Mink et al., 2009).

1.3.4 On a complete picture of multiple population formation

Combinations of several sources tend to explain theory better, and it is as expected since all objects exist in a cluster simultaneously (Gratton et al., 2019; Sills & Glebbeek, 2010). It is clear that if no particular enrichment source produces enough mass for the observed fraction of enriched stars in MPs, the mass budget problem can be (partly) alleviated by considering the total contributed mass from multiple types of sources. Regarding abundance trends, Bastian et al. (2015) independently compared the ability of yields from different enrichment sources with dilution to observed abundance trends, finding no model sufficiently described observed MPs. Based on their results, we suggest a combination of polluters could simultaneously explain observed Na-O correlations and stochasticity. Larger spreads in O from AGB stars and SMS can alleviate the narrow ranges seen in massive stars, both interacting binaries and FRMS. The excessively large spreads in He seen with enrichment in other sources, will be dampened by the smaller He spreads observed in binary ejecta. The mixing of abundances from various enrichment sources better explains the observed correlations and anti-correlations (Sills & Glebbeek, 2010).

However, the high helium spreads associated with all sources suggest that no combination of sources dependent on hot-H burning and self-enrichment can produce the observed characteristics of MPs. If the self-enrichment model does hold, the variation of Li abundances in MPs suggests destruction by massive stars and production by AGB stars could both play a role in generating MPs.

Single star polluters like AGB stars and FRMS have been modelled and studied extensively over the past couple of decades (Milone & Marino, 2022; Bastian & Lardo, 2018; Gratton et al., 2019, for reviews). Comparatively, massive interacting binaries have not, with many assessments depending on the one system simulated by de Mink et al. (2009)

(e.g. Bastian et al., 2015; Howard et al., 2019). This theory has had relatively little follow-up since its initial proposal, warranting a deeper study as the problem of MPs remains unresolved. As projected by Bastian et al. (2015), the dependence of interacting binary yields on parameters like mass ratio, evolutionary phase of the stars during mass transfer, primary mass, and period, can introduce stochasticity. This also suggests that an assessment of the contribution of binaries to the formation of MPs requires a comprehensive study of the variation of binary yields over parameter space.

1.4 This work

We investigate what role binaries may play in multiple populations, extending beyond the single binary simulated by de Mink et al. (2009). This work presents the results of simulating two grids of 204 binaries each, with primary masses ranging from 10-40 M_{\odot} . We describe our methods for simulating the models and selecting the parameter space in section 2. A total of 190 alpha-enhanced models are included in our main sample. In section 3 we summarize our findings. We consider the enrichment produced over our parameter space in section 3.1. From our suite of models, we determine the parameter space where enriching binaries tend to lie, informing how common and significant the impact binary ejecta has on forming enriched populations. Abundance trends of the binary ejecta as a suite are also presented.

We use the yields from our binaries alongside observed period, mass, and mass ratio distributions to examine the typical contribution of a binary population within a cluster in section 3.2. In particular, we look at the total mass, timescales, and abundance spreads are consistent with MP formation. The differences in yields due to initial composition are considered through a sample of 181 solar-scaled models in section 3.3.

We consider the implications of our yields in more detail in sections 4.1 and 4.2.1, through comparison to observed MP properties. We also discuss the limitations of our study and present avenues for future work in sections 4.3 and 4.4. We offer an initial assessment of whether binaries, in general, contribute to the formation of MPs and the extent to which they do.

Chapter 2

Methods

2.1 General overview

Binaries were simulated with Modules for Experiments in Stellar Astrophysics (MESA) r15140 (Paxton et al., 2011, 2013, 2015, 2018, 2019; Jermyn et al., 2023). This version was released near the end of 2020 between the publications by Paxton et al. (2019) and Jermyn et al. (2023). All MESA models were run on the Alliance Canada supercomputer/cluster Graham. MESA is an open-source 1d stellar evolution code which includes binary evolution. Due to the extreme computational demands of multidimensional models, 1d stellar evolution is the current standard for the field (Rizzuti et al., 2023). Various capabilities are implemented in modules, for flexibility in simulating a range of astrophysical processes.

Paxton et al. (2011) is the introductory paper for MESA and describes its general operation which we summarize here. For each star, stellar structure and composition are coupled and evolved simultaneously. These are evolved according to differential relations that describe the properties of the star such as pressure, density, temperature, and chemical composition. Models are constructed to be spherically symmetric and one-dimensional by

dividing the entire star into cells, adaptively. Atmospheres are evolved separately from the stellar interiors with atmosphere properties providing boundary conditions for the interior. MESA implements multiple solvers for equations as part of the `num` module, each with different suitable use cases. We do not alter the preference for solvers from the default settings. Angular momentum, linear momentum, and energy are conserved as the star is evolved, accounting for mass loss. Algorithms in the code are parallelized to run sections concurrently using different threads on a processor through OpenMP.

By default, MESA models use hydrostatic forms of the structure and composition differential equations as much smaller time steps are required to evolve the models hydrodynamically. Furthermore, individual radial cell velocities are not evolved or calculated by default. This means fluid motions like turbulence and shocks are not modelled directly. In the default MESA settings hydrodynamics is switched on for systems that begin core-collapse. This is not relevant to our models as we end our simulations before core-collapse would be initiated. Hydrodynamical processes are instead handled through independent modelling of convection, overshoot, and mixing processes which we discuss in our selection of physical parameters.

Opacities and nuclear reaction rates are based on pre-calculated tables. Opacity coefficients describe the effective absorption of photons of a given wavelength due to a material (Rybicki & Lightman, 1979). Radiative transfer is one of the key components in stellar evolution modelling and depends on reliable values for opacities (Harris, 1996). For example, opacity affects the structure of its envelope by impacting radiative flux, alongside impacting its spectra and atmosphere (Baraffe et al., 1998; Paxton et al., 2013). The high-temperature opacities use the OPAL tables from Iglesias & Rogers (1993, 1996). OPAL tables are standard in stellar evolution codes with examples such as PARSEC (Bressan et al., 2012,

which is an update of Padova), the Dartmouth Stellar Evolution Program (DSEP, Dotter et al., 2008), and models by Ekström et al. (2012) and their subsequent stellar model grids. We use the Type 2 tables that account for variations in C and O independently of changes due to scaling solar fractions based on Z . Opacity from Compton scattering, which is the scattering of high energy photons off of charged particles, becomes important at higher temperatures $T \gtrsim 10^8$ K.

Reaction rates in MESA use several references though the majority come from JINA’s ReaLib (Cyburt et al., 2010) or NACRE (Nuclear Astrophysics Compilation of REaction rates; Angulo, 1999). ReaLib rates apply only for $T > 10^7$ K and assume complete ionization. MESA allows for customization of rates, but we use the default settings. An extensive network of nuclear reactions and isotopes (> 30 isotopes) along with the associated composition and energy evolution is the largest demand of the simulations in terms of computational resources (Jermyn et al., 2023). We do not use operator-splitting to calculate nuclear burning, following the defaults of MESA instead.

Binaries in MESA were introduced in the paper by Paxton et al. (2015), and we provide an overview of the details here. Modelling binaries in MESA is accomplished through a module, `binary`, and can be used to evolve a stellar model with a point mass, or in our usage: coevolve two stellar models. The modelling includes the effects of being in a binary on each of the stars such as tidal forces and mass transfer. Stars are assumed to rotate about axes perpendicular to their plane of orbit. At each time step, each star is evolved and the orbital properties are evolved. Although they evolve using the same timestep, they evolve independently for “flexibility and simplicity”.

Under rotation, spherical symmetry no longer holds. Details on how this is handled are presented by Paxton et al. (2013), with updates in Paxton et al. (2019), with highlighted

details following. To approximate the 3d effects of rotation in 1d, MESA adopts the shellular approximation referencing Meynet & Maeder (1997). Shells that are surfaces of equal pressure (isobars) are considered to be rigidly rotating and the effects of rotation are averaged over each shell. Rotation modifies the effective potential of the star, through distortion of the isobaric surfaces and a change in the effective gravity from centrifugal effects. In this shellular approach, MESA can still model the effects of differential rotation while using 1d stellar structure equations. The rotation-distorted shells are used instead of the spherical shells, and the influence of rotation is added to the standard structure equations.

2.2 Physical prescriptions

2.2.1 Overview of prescriptions

Through files called `inlists`, MESA users can specify input physics, mesh controls, and time step controls. We use `inlists` from the 15+16 M_{\odot} binary with self-consistent mass transfer modelled by Paxton et al. (2015) and shown in their Fig. 8 as a starting point.

The MESA Isochrones and Stellar Tracks (MIST) project provides single-star models calculated in MESA over a wide range of ages, masses, and metallicities (Choi et al., 2016; Dotter, 2016). MIST models have been extensively used in estimating stellar and globular cluster properties over a wide range of metallicities and ages, and continue to be a popular choice today (e.g. da Silva & Smiljanic, 2023; Adamo et al., 2023; Tacchella et al., 2023; Agüeros et al., 2018). They have also been used to infer galaxy formation history (e.g. Nogueras-Lara et al., 2020; Bonaca et al., 2020; Leja et al., 2020). Treating the MIST models as standard, we adopt some of the input physics from Choi et al. (2016) as modifications to the Paxton et al. (2015) binary `inlists`. For reference, table 1 of the

paper by Choi et al. (2016) show their references for their adopted parameters and physics. Note that the MIST models use an earlier version of MESA and there have since been updates to energy conservation, reaction rates, and how rotation is handled (see Paxton et al., 2019). We summarize the details of our chosen physical parameters in the remainder of this section. The base inlists, `run_star_extras.f90`, and `run_binary_extras.f90` are provided in appendix A.

2.2.2 Construction of simulations

Stars within a binary were simultaneously evolved from zero-age main sequence (ZAMS) models until core-C depletion of the primary star. We define this as when the central ^{12}C mass fraction drops to 5×10^{-3} . Our ZAMS models cover masses from $1 - 100M_{\odot}$ in steps of 0.1 in log space. ZAMS refers to the point where the core of the star ignites hydrogen burning, starting its main sequence. In MESA, this is defined as the point where the luminosity at the surface is exceeded by the nuclear-burning luminosity. ZAMS models are built from evolving pre-main sequence models in MESA. These start with a uniform composition and are uniformly contracted to be fully convective without core burning.

We also run single-star models using the same input physics as the binary models. We used these to determine the periods to sample for our binaries and comparison of yields.

2.2.3 Initial composition of models

We simulated two grids of binaries with different compositions of metals. For one grid, metal mass fractions are scaled to the Asplund et al. (2009) solar abundances. The other grid has an alpha-enhanced composition, relative to the solar-scaled abundances. All stars have initial $[\text{Fe}/\text{H}] = -1.44$. This corresponds to a solar-scaled metal mass fraction of

$Z = 5 \times 10^{-4}$ and an alpha-enhanced metal mass fraction of $Z = 1.2 \times 10^{-3}$. These metallicities are similar to that of the binary simulated by de Mink et al. (2009), which had an alpha-enhanced initial composition and $Z = 5 \times 10^{-4}$. Solar-scaled binaries were the first set we began to simulate and we opted to have them at the same Z as the de Mink et al. (2009) system for comparison. Our chosen metallicity of $[\text{Fe}/\text{H}] = -1.44$ is intermediate of values observed in globular clusters, both Galactic and extra-galactic (Carretta & Gratton, 1997; Larsen et al., 2022; Harris, 1996, 2010 version).

The relative abundances of ^1H , ^2H , ^3He , and ^4He are consistent between the models at setup. Alpha-enhancement follows values from Reddy et al. (2006), where $[\text{Fe}/\text{H}] = -1.44$ puts us in the metal-poor plateau. This is the same alpha-enhancement reference used in the NuGrid stellar models by Ritter et al. (2018). The NuGrid simulations from this paper are also performed with MESA, albeit r3709 (with earlier models from r3372). However, for $[\text{O}/\text{Fe}]$ enhancement we do not follow Reddy et al. (2006), as the O measurements do not have non-LTE (local thermodynamic equilibrium) corrections. Non-LTE corrections have been shown to significantly reduce measured oxygen abundances (Asplund et al., 2004). Instead, we follow the same fitting procedure as Ritter et al. (2018) on the updated $[\text{O}/\text{Fe}]$ data from Ramírez et al. (2013). As a summary of the procedure:

1. We apply the selection cuts from Ramírez et al. (2013) to exclude very cool dwarfs, giants, and disk outliers.
2. For $-1 < [\text{Fe}/\text{H}] \leq 0$, we perform a least-squares linear fit to $[\text{O}/\text{Fe}]$ vs. $[\text{Fe}/\text{H}]$ for all remaining halo and disc stars; i.e. $[\text{O}/\text{Fe}] = A \cdot [\text{Fe}/\text{H}] + B$ for fit parameters A, B .
3. For $[\text{Fe}/\text{H}] \leq -1$, stars are considered to be part of a plateau where $[\text{Fe}/\text{H}] = -A + B$.

Element	[X/Fe]
C ¹²	0.562
O ¹⁶	0.440*
Ne ²⁰	0.500
Mg ²⁴	0.411
Si ²⁸	0.307
S ³²	0.435
Ar ³⁶	0.300
Ca ⁴⁰	0.222
Ti ⁴⁸	0.251

Table 2.1: Relative initial abundance of metals in alpha-enhanced models which are in the metal-poor plateau region of alpha enhancement. Except for * which is based on Ramírez et al. (2013), all values come from Reddy et al. (2006). $[X/Fe] = \log_{10} \left(\frac{N_X/N_{X,\odot}}{N_{Fe}/N_{Fe,\odot}} \right)$ is the logarithmic enhancement of element X relative to Fe, compared to scaled-solar.

This results in an adopted value of $[O/Fe]= 0.440$ for our alpha-enhanced models. Table 2.1 shows the relative abundances used for the alpha-enhanced models. All other metals not included in the table were left unaltered, to keep $[Fe/H]$ fixed. Both Reddy et al. (2006) and Ramírez et al. (2013) report abundance measurements of stars in the Galactic thin-disc, thick-disc, and halo. Ramírez et al. (2013) measured the abundance of F-, G-, and K-dwarfs. Reddy et al. (2006) measure only F- and G- dwarfs but discuss some of their results in comparison to surveys containing F-, G-, and K-dwarfs; finding similar behaviour in enhancement with differing $[Fe/H]$.

Metal-poor globular clusters and stars, typically have enhanced alpha element abundances, though some clusters show less or no alpha enhancement (e.g. Larsen et al., 2022). Having two grids, we can measure how differences in initial composition may influence the enrichment provided by binaries.

Following the scaling

$$Y = Y_p + \left(\frac{Y_{\odot, \text{protosolar}} - Y_p}{Z_{\odot, \text{protosolar}}} \right) Z, \quad Y_p = 0.249 \quad (2.2.1)$$

this metallicity corresponds to an initial helium mass fraction of $Y = 0.24975$ for solar-scaled initial composition and $Y \sim 0.25092$ for alpha-enhanced (Choi et al., 2016; Asplund et al., 2009). Our choice to keep $[\text{Fe}/\text{H}]$, the observational tracer for overall metallicity, constant leads to a change in the mass fractions of H, He, and metals X, Y, Z . We ensure that the referenced opacity tables, built into MESA, are based on the Asplund et al. (2009) solar abundances.

2.2.4 1d mixing prescriptions

Mixing within a star plays a key role in determining its structure and evolution (e.g. Ekström et al., 2012; Paxton et al., 2011). For example, the location of the giant branch in luminosity-temperature plots varies with the He structure of the star (Tayar & Joyce, 2022). The processes involved in mixing are not entirely well-constrained; their implementation in 1d evolution codes relies on several free parameters. We summarize our choices and their impact below.

Mixing-length theory (MLT), which was first applied to stellar astrophysics by Böhm-Vitense (1958), is implemented in MESA to capture effects of convection (Joyce & Tayar, 2023; Paxton et al., 2011). It is also implemented in other stellar evolution models such as PARSEC (Bressan et al., 2012), Y^2 (Yonsei-Yale; Demarque et al., 2004), and BaSTI (a Bag of Stellar Tracks and Isochrones; Hidalgo et al., 2018). Modelling convection in stars is one of the largest sources of uncertainty in stellar evolution with the details in observed stars

hidden from direct measurement (Joyce & Tayar, 2023; Choi et al., 2016). Joyce & Tayar (2023) provide a comprehensive review of the impact of MLT on 1d stellar modelling.

Convection is the circulation of material due to changes in density associated with temperature changes. Hotter blobs of fluid become less dense compared to colder surroundings and rise and expand (Joyce & Tayar, 2023). In a fully-hydrodynamic model, this would generate eddies in the material that carry around energy, momentum, and chemistry (Rizzuti et al., 2023). In MLT, the effects of the net, large-scale motions are considered through several prescriptions. We summarize the scheme implemented in MESA, presented in Paxton et al. (2011). Our models use the default Cox method based on chapter 14 of Cox & Giuli (1968) which assumes optical thick media without radiative losses. We choose to use the Ledoux criterion for convective boundaries,

$$\nabla_{\text{rad}} < \nabla_L \quad (2.2.2)$$

$$\nabla_L = \nabla_{\text{ad}} - \frac{\chi_\mu}{\chi_T} \nabla_\mu \quad (2.2.3)$$

$$\chi_\mu \equiv \left[\frac{\partial \ln(P)}{\partial \ln(\mu)} \right]_{\rho, T} \quad (2.2.4)$$

$$\chi_T \equiv \left[\frac{\partial \ln(P)}{\partial \ln(T)} \right]_{\rho, \mu} \quad (2.2.5)$$

which balances the local (radiative) temperature gradient ∇_{rad} , against the summed adiabatic gradient ∇_{ad} and the effects from a composition gradient ∇_μ (see Choi et al., 2016). P refers to the pressure and ρ to density. This is in contrast to the simpler Schwarzschild criterion

$$\nabla_{\text{rad}} < \nabla_{\text{ad}} \quad (2.2.6)$$

which does not consider compositional differences.

If the radiative temperature gradient is larger, $\nabla_{\text{rad}} > \nabla_L$, then the zone is unstable to convection and becomes a convective zone (Joyce & Tayar, 2023). Boundaries between convective and non-convective regions are then where the radiative temperature gradient is equal to the compositional and adiabatic gradients. The behaviour of convective zones is dependent on a free parameter of order unity α_{MLT} , which sets the mixing length l_{MLT} in terms of α_{MLT} times the pressure scale height. As convective mixing is treated as a diffusive process in this framework, time dependence is implemented through diffusive coefficients calculated by the MESA `mlt` module. The efficiency of convective mixing is primarily set by the choice of α_{MLT} . We use the same value of $\alpha_{\text{MLT}} = 1.82$ as Choi et al. (2016). They determined this value by matching helioseismologic data.

Choi et al. (2016) opted to use the MLT option `henyey` (Henyey et al., 1965) which considers opacity, extending the framework to optically thin regimes, relevant for atmospheres. However, Choi et al. (2016) note that radiative envelopes of massive stars are still uncertain with either choice of MLT scheme.

For more accurate modelling of convective mixing, MLT is used in combination with semi-convection, overshoot, and thermohaline mixing.

Semi-convection refers to regions in the star where composition stabilizes against convective mixing (Paxton et al., 2013). These regions are stable to the Ledoux criterion but are Schwarzschild unstable. Our models adopt a semi-convection mixing-length parameter of $\alpha_{\text{sc}} = 1$ from the Paxton et al. (2015) binary. The value of $\alpha_{\text{sc}} = 0.1$ from Choi et al. (2016) leads to relatively small changes to models of single 10 and 30 M_{\odot} stars in preliminary testing. We opt for the choice of $\alpha_{\text{sc}} = 1$ for simplicity. The value of α_{sc} is expected to more greatly affect the accretor in a binary than a single star as compositional gradients can easily arise from accretion (Paxton et al., 2015). Values in literature span from $0.001 \lesssim \alpha_{\text{sc}} \lesssim 1.0$

so our models use rather efficient semi-convection (Paxton et al., 2013). Semi-convection modelling has been shown to impact core helium-burning stars and their yields (see §3.6.3 Choi et al., 2016).

At boundaries between convective and non-convective (often radiative) zones, convective mixing in MLT is treated as the movement of large-scale blobs of gas. This is implemented through a scheme called overshoot and can be considered as extended convective mixing (Herwig, 2000). Overshoot accommodates for the motion that convective eddies would have that could carry them into regions satisfying stability criterion against convection (Paxton et al., 2011). Our models use the exponential scheme, where mixing past the border is smoothed with an exponential decay of the diffusion coefficient without overshoot, as a function of distance. We use the same overshoot efficiencies and coefficients as used for the MIST models,

$$f_{\text{OV,core}} = 0.016 \tag{2.2.7}$$

$$f_{\text{OV,env}} = 0.0174 \tag{2.2.8}$$

$$f_{0,\text{OV}} = 0.5 f_{\text{OV}} \tag{2.2.9}$$

which are calibrated empirically to the shape of the MS turn-off in OC M67 (Choi et al., 2016). The coefficients are consistent with suggestions from Herwig (2000) for an exponential overshoot. Larger values of f_{OV} lead to more substantial overshoot. As mentioned by Paxton et al. (2013) in §B.7.2, suitable choices are expected to depend on the star, possibly through mass, metallicity, and/or evolutionary stage.

Our models implement convective premixing while on the main sequence, from ZAMS until the central mass fraction of hydrogen dips below 1×10^{-4} . Convective premixing

(CPM) was introduced in §5 of Paxton et al. (2019) to address how convective boundaries were determined. We repeat the relevant details here. As MESA models are divided into cells, numerical convective boundaries may not necessarily align with “physical” ones as regions must extend to cell boundaries. In earlier versions of MESA, the boundaries were then found as a sign change of the discriminant, which for the Ledoux criterion is

$$y_L = \nabla_{\text{rad}} - \nabla_L \tag{2.2.10}$$

where ∇_L is a combination of the adiabatic gradient (∇_{ad}) and the compositional gradient. This causes issues when there are discontinuities in the composition and goes against the expectation that the convective side of the boundary in MLT should have $\nabla_{\text{rad}} = \nabla_{\text{ad}}$. To remedy this, the CPM scheme adjusts cells where $y > 0$ (convective) on one face and $y < 0$ (radiative) on the other face. Mixing at the start of each time step at boundaries between radiative and convective zones is done iteratively to redefine the convective boundaries if the change from mixing is consistent with the new region being convective. Convective zones may also be adjusted through retreating a cell or splitting a cell under a similar assessment. The algorithm ends as the single radiative face of the boundary is fully consistent with the newly mixed and extended convection zone. As the diffusive timescale near convective boundaries is small compared to typical nuclear timescales, MESA treats CPM as instantaneous. CPM improves the modelling of the convective and semi-convective regions of stars but is not recommended for late core-He-burning models, due to uncertainty in the expected behaviour of core pulses in this phase.

In regions stable against convection according to the Ledoux criterion, a process called thermohaline mixing can occur Paxton et al. (2013). If the mean molecular weight is higher at larger radii, the denser material falls in, with relatively slow compositional diffusion

leading to “fingering” mixing (Brown et al., 2013). We use a thermohaline coefficient of $\alpha_{\text{th}} = 1$, following the binary in (Paxton et al., 2015). The thermohaline diffusion coefficient calculations follow the default option in MESA, described by Kippenhahn et al. (1980). Tests in single star models using a thermohaline coefficient of 666, as used by Choi et al. (2016), lead to negligible differences in evolution. Adopted values for the thermohaline coefficient can range over several orders of magnitude, $1 \lesssim \alpha_{\text{th}} \lesssim 667$ (Paxton et al., 2013). Multidimensional hydrodynamical simulations may support using smaller values of α_{th} rather than larger ones.

Rotation is particularly effective at bringing internal material to the surface through mixing and increased mass loss (Ekström et al., 2012; Meynet & Maeder, 2000). Tidal forces and accretion within binaries can increase and support the rotation rates of the stars, placing importance on the effects of rotational mixing (Paxton et al., 2015; Smith, 2014). Rotational mixing affects the evolution of the star significantly. For example, it increases the amount of fuel available in the core during the main sequence (MS), increasing the MS lifetime and surface temperatures (Eldridge & Stanway, 2009; Meynet & Maeder, 2000).

Paxton et al. (2013) explain how rotation is modelled in MESA, which we summarize here. Rotation generates instabilities that drive turbulence along isobaric surfaces. MESA allows the specification of coefficients for chemical diffusion, angular momentum, and energy transport. These are handled as a diffusive approximation with separate coefficients for each process described in MESA. There are multiple rotational instability models implemented in MESA, each with coefficients that can be modified. We use all of the non-magnetic processes, as done by Choi et al. (2016). MESA code for these is based on the publications by Heger et al. (2000) and Heger et al. (2005) who also describe each of the instabilities in detail.

The total rotational mixing of material is controlled by `am_D_mix_factor` for which we use the recommended value ($\sim 1/30$) from Charbonneau (1992) used by Heger et al. (2000), and both MESA and MIST. For all of the rotational mixing processes, we use the same coefficients as Choi et al. (2016) which provided better stability and convergence of models in preliminary testing than parameters from the binary in Paxton et al. (2015).

The critical rotation rate defined in MESA is where the equatorial centrifugal force is equal to the force of gravity (Paxton et al., 2019). Stars are allowed to rotate up to a maximum fraction of 0.9 the critical rate, according to recommendations from Paxton et al. (2019) for numerical stability.

We do not include the effect of generated magnetic fields on mixing, as is the case in both the reference binary from Paxton et al. (2015) and the models from Choi et al. (2016). Magnetic rotational mixing is not compatible with the other rotational mixing prescriptions and the efficiency of this mixing is controversial (see discussion in Paxton et al., 2019; Choi et al., 2016).

Through similar mechanisms, a lack of semi-convection, larger overshoot, and more efficient rotation-induced mixing can extend the lifetime of stars with convective H or He-burning cores (stellar mass $\gtrsim 1.5 M_{\odot}$) by increasing their size (Paxton et al., 2013). This has an impact on the subsequent yields of the star (e.g. Herwig, 2000).

2.3 Binary prescriptions

Binary controls in our models generally follow the controls used for figure 8 in Paxton et al. (2015).

2.3.1 Orbits, tides

Our models follow the same self-consistent mass transfer scheme laid out by Paxton et al. (2015). Tides refer to the differential gravitational forces that the stars in a binary exert on each other, altering their shape and rotation. Binaries start tidally synced on a circular orbit. As the binaries we are most interested in are short-period binaries, these are likely to be circularized so we opt for this simplifying assumption (Moe & Di Stefano, 2017). This means that the rotation of the stars is synchronized with the orbit and is sometimes called tidal locking. True tidal synchronization is only possible for circular orbits and is expected for short-period binaries (Lurie et al., 2017). Interactions between the binary stars and the evolution of the individual stars, leading to mass loss for example, can remove the synchronization (Paxton et al., 2015). Tides are evolved according to prescriptions from (Hurley et al., 2002) for radiative envelopes. Each layer of each star is independently synced according to the calculated synchronization time scale.

There are a few differences in the treatment of angular momentum in this scheme compared to default settings in MESA. We do not perform magnetic braking. Magnetic braking refers to the coupling between stellar winds and the magnetic field leading to a slowdown in stellar spins which can efficiently reduce the orbital angular momentum if tidally synced (Paxton et al., 2015). This process in MESA is only appropriate for stars with low mass stars with convective envelopes and radiative cores. Magnetic braking for radiative envelopes (massive stars) is not predictable. Angular momentum loss from the orbit is computed based on mass loss unaccounted for by the stellar angular momentum loss (`do_jdot_missing_wind`). We also allow angular momentum transfer through accretion (`do_j_accretion`). Both `do_jdot_missing_wind` and `do_j_accretion` are necessary for following the non-conservative mass transfer taking place in these binaries.

Changes in the orbital angular momentum do include effects from the coupling between the stellar spins and orbit (spin-orbit or L-S coupling), radiation of gravitational waves, and mass loss. Magnetic braking is not compatible with L-S coupling in MESA.

2.3.2 Mass transfer

We use the “Ritter” scheme for computing mass transfer as is default (Ritter, 1988). This is the same description used for mass transfer in the binary code de Mink et al. (2009) used. In this model, stars can lose mass before reaching the boundary of their Roche Lobe. Accounting for their extended atmospheres, the mass loss can be estimated as an exponential decay on a scale length following the pressure scale height at the atmosphere with a mass ratio q -dependent factor ($q = M_2/M_1 \leq 1$). The mass loss rates are computed implicitly at each time step for a maximum of 100 tries by finding upper and lower limits for a new rate based on the current one and determining the next try based on the limits. Implicit methods reduce the jumps in mass loss rates that arise from calculating mass loss rates explicitly at each time step. The value is taken once a new solution is within the tolerance of the old one or if the maximum number of tries is reached. To prevent sharp composition jumps that may occur with accretion, the outer layer of the secondary is smoothed as done by Paxton et al. (2015). The outer $0.05 M_{\odot}$ are smoothed in windows of $0.03 M_{\odot}$. This improves the behaviour of thermohaline mixing (Paxton et al., 2015).

2.3.3 Other details

We use a custom reaction network containing 65 species for more complete coverage of H, He, and C/O burning as well as some coverage of alpha processes. At each time step we compute and output the mass loss rate for various isotopes through a routine added to

`run_binary_extras.f90` based on code from MESA r10000. We track the ejection of 50 total species, covering all isotopes of H, He, Li, Be, B, C, N, O, F, Na, Mg, Al, Si, Ca, Ti, Ni, Cr, and Fe included in our reaction network.

Stellar winds are modelled using the `dutch` option in MESA which is the default and mainly references Glebbeek et al. (2009). For high temperatures results from Vink et al. (2001) and Nugis & Lamers (2000) are used. At low temperatures, we use the scheme based on de Jager et al. (1988). We use wind parameters matching the rotating binary from Paxton et al. (2015).

2.4 Parameter space for models

Between binaries we vary the initial masses M_1, M_2 and the initial period P . Based on test runs of single stars, we found convergence of the models was largely affected by the `inlist` parameters related to `varcontrol`. These set the target relative change between subsequent models. For single stars `varcontrol_target` is increased for higher masses, similar to what is done by Choi et al. (2016), however, we increase it in steps rather than linearly with M . We choose to use `varcontrol_target` = 1×10^{-4} for single stars with $M < 30 M_\odot$, 4×10^{-4} for $30 \leq M < 40 M_\odot$, 5×10^{-4} for $M = 40 M_\odot$ for non-rotating models, and 6×10^{-4} for $M = 40 M_\odot$ for rotating models.

For binary stars, there are multiple `varcontrol` settings for different evolutionary phases of the individual stars, and for whether mass transfer is taking place. We use the same settings as used for figure 8 of Paxton et al. (2015) for the initial run of all models. For runs we identify as having convergence issues, based on visual inspection of plots of the models' evolution, we rerun the simulation with new parameters and select the run with the most stable results or longest evolution as part of our sample.

We use three different stopping conditions for our binaries:

1. spike in system mass loss rate,
2. binaries come into contact,
3. or primary core C depletion.

We check for these stopping conditions in the order they are listed. For a binary to be included in our completed sample, it must eject at least 0.1 solar masses of material and have the primary reach RLOF during simulation time. This imposes that the binaries we examine undergo non-conservative mass transfer, the mechanism we are interested in for acting as an enrichment source.

The specific criteria are as follows. Large fluctuations in the system mass loss rate indicate physical and/or numerical instability of the model. These are detected through checking for numerical divergences in the mass loss rate of the system as a function of the ejected mass, such that the numerical gradient that is calculated using `numpy.gradient` (Harris et al., 2020) is larger than $10^8 \log M_{\odot} \text{ yr}^{-1} / M_{\odot}$ in magnitude. We also impose that the fractional mass loss rate of the system is larger than 10^{-3} yr^{-1} . These conditions were tested on a preliminary set of binaries to select for runs that visually had poor convergence and had the highest sensitivity out of other gradients and thresholds which we tested. We note that the instabilities we aim to exclude occur during periods of small time steps ($10^{-10} \sim 10^{-12} \text{ yr}$), so variations in cut-off points do not significantly impact results.

Binaries are considered to be in contact when both stars are simultaneously overflowing their Roche lobes. MESA outputs the relative RLOF:

$$\text{relative RLOF} = \frac{R_{\star} - R_{\text{RL},\star}}{R_{\text{RL},\star}}. \quad (2.4.1)$$

When both stars’ relative overflows are above -0.01 , we consider the stars to be approaching contact and treat this as the stopping point. A threshold of -0.01 rather than 0 , was used as some runs stall with small time steps as the primary approaches RLOF and this threshold catches these near-contact binaries. As our current MESA settings do not allow for the reliable evolution of contact binaries, we cannot simulate these further than their termination.

Primary core C depletion is when the primary star reaches a mass fraction of carbon below 0.005 :

$$X_{C^{12},\text{center}} = 0.005 \quad \text{center_c12}=0.005. \quad (2.4.2)$$

To ensure this is core-C depletion and is not triggered by low C on the main sequence, we also require a low He mass fraction ($< 1 \times 10^{-4}$). We choose to terminate runs at this point as we are interested primarily in the ejection of hot H-burning products. Past this stage, the stars are expected to become supernovae, shedding a significant portion of an iron-enhanced envelope in an energetic explosion (Paxton et al., 2018). On its own, MESA cannot model the entire core collapse and explosive phase of the supernova (Paxton et al., 2018).

2.5 Simulations

2.5.1 Parameter space selection

We choose to explore the dependence of enrichment on M_1 , the mass ratio $q = M_2/M_1$, and P . The masses of primary stars are roughly evenly log-spaced, ranging from $10 - 40 M_\odot$. Although higher mass binaries have been observed (e.g. Shenar et al., 2022), they are increasingly uncommon due to the shape of the IMF favouring less massive stars (e.g. Kroupa, 2001). Furthermore, above $40 M_\odot$, the stellar evolution, particularly the mass loss

rates, are uncertain (Smith, 2014). This largely applies to the post-MS phase of evolution, which is where we select our binaries to initiate mass transfer (Smith, 2014).

Periods were sampled so that based on models of single star evolution, mass transfer would occur around core-H exhaustion up until core-He ignition of the primary with 5 points in log space. These events correspond to peaks in the radius evolution of the star. We expected this evolutionary range to cover the range where binaries were most likely to contribute enrichment, with maximal products from H-burning and minimal products from advanced burning based on what has been produced in the core and may be stripped from the envelope of the primary. Another period above the upper limit expected with core-He ignition was sampled to test the veracity of this assumption. Details on this process are covered in the next section, §2.5.2.

The evolutionary endpoints correspond to periods ranging from approximately 2-700 days. Extended, we simulate up to ~ 2800 days. The lower limit falls into a narrow range of around 2-3 days for the mass range we cover. The upper period limit varies sharply with mass in comparison to the lower limit. With a narrower range of periods for the high-mass primaries expected to act as enrichment sources, and with the relative rarity of high-mass primaries, the high-mass binaries in our sample are not expected to contribute significant enrichment overall, within a cluster.

Mass ratios were evenly sampled over the range of 0.15 - 0.9. This excludes twins, $q \gtrsim 0.95$, which if close enough to initiate mass transfer in our simulations, would become contact binaries which we cannot simulate.

Since lower mass stars were expected to contribute less enrichment, we progressively restrict the range of q sampled for $M_1 \leq 15 M_\odot$. Lower mass ratios also lead to smaller tidal forces on the donor star, potentially reducing the rotational mixing in the primary and

reducing the enrichment near the surface. Fig. 2.1 shows the parameter space sampled by the binaries, spanning P, M_1, q . A total of 408 binaries were simulated. Binaries that meet one of the three stopping conditions highlighted above are included in our primary sample. We also consider the implications of envelope ejections in runs that do not reach primary core-C depletion, i.e. if they were to also approach core collapse in section 3.4.

2.5.2 Single star models and stellar tracks

To compare the yields of single stars to the yields of binaries as well as set up the binary period limits, we simulate grids of stellar models, as mentioned earlier. To cover the range of primary and secondary masses in our binary grid we simulate single stars with masses from $3 \leq M \leq 40 M_{\odot}$, with roughly equal log spacing. For each initial composition (solar-scaled and alpha-enhanced), we simulate the stars with and without rotation. We initialize the rotating models with a rotation rate relative to the critical rotation rate of $\omega = 0.2\omega_{\text{crit}}$. This corresponds to the maximum rotation we saw in initially tidally synced binary models, where period limits were only described by non-rotating stellar models. We present the stellar tracks for our single star models in figures 2.2 for the solar-scaled models and 2.3 for the alpha-enhanced models. In figure 2.2 we compare our non-rotating models to similar models in MIST. Note that alpha-enhanced models for MIST have not yet been released. The difference in location and shape of the loop between our models and MIST's towards higher T_{eff} , known as the 'blue loop', can be attributed to the different Y of the models. Our resolution of the higher mass stellar tracks appears better than MIST's and is likely due to choices to follow Paxton et al. (2015) in constraining the maximum change in location for the stellar tracks.

High-mass singles $M \geq 10 M_{\odot}$ ignite core-C, so we impose the same stopping condition

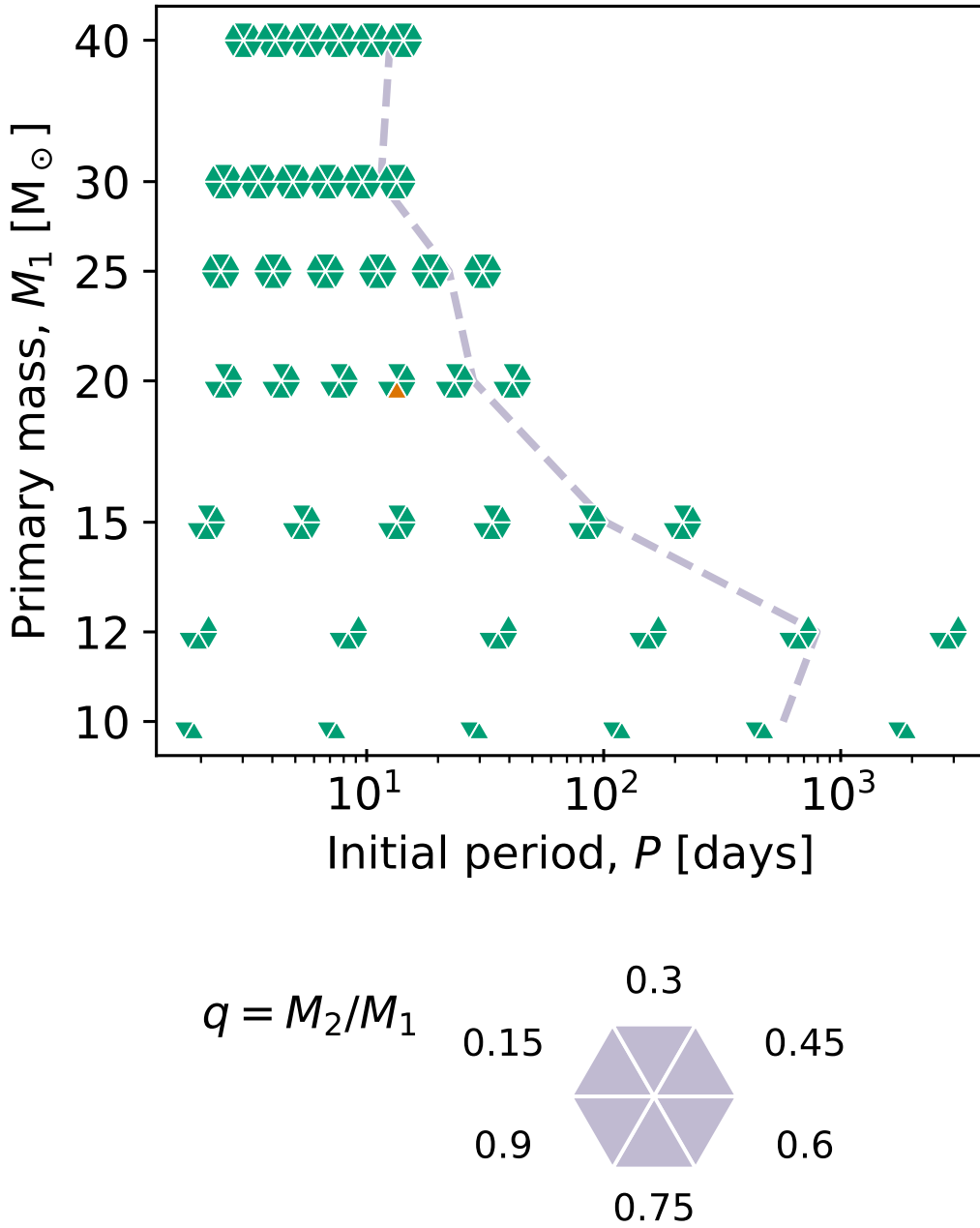


Figure 2.1: Periods, primary masses, and mass ratios of the binaries simulated in this work. Binaries of the same initial primary mass and initial orbital period are triangular segments of a hexagon centred on the primary mass and period. The relative position of the segment represents the mass ratio, q , shown in the legend. The grey dashed line represents the expected upper limit on the period for binaries of interest based on single-star models at the sampled primary masses.

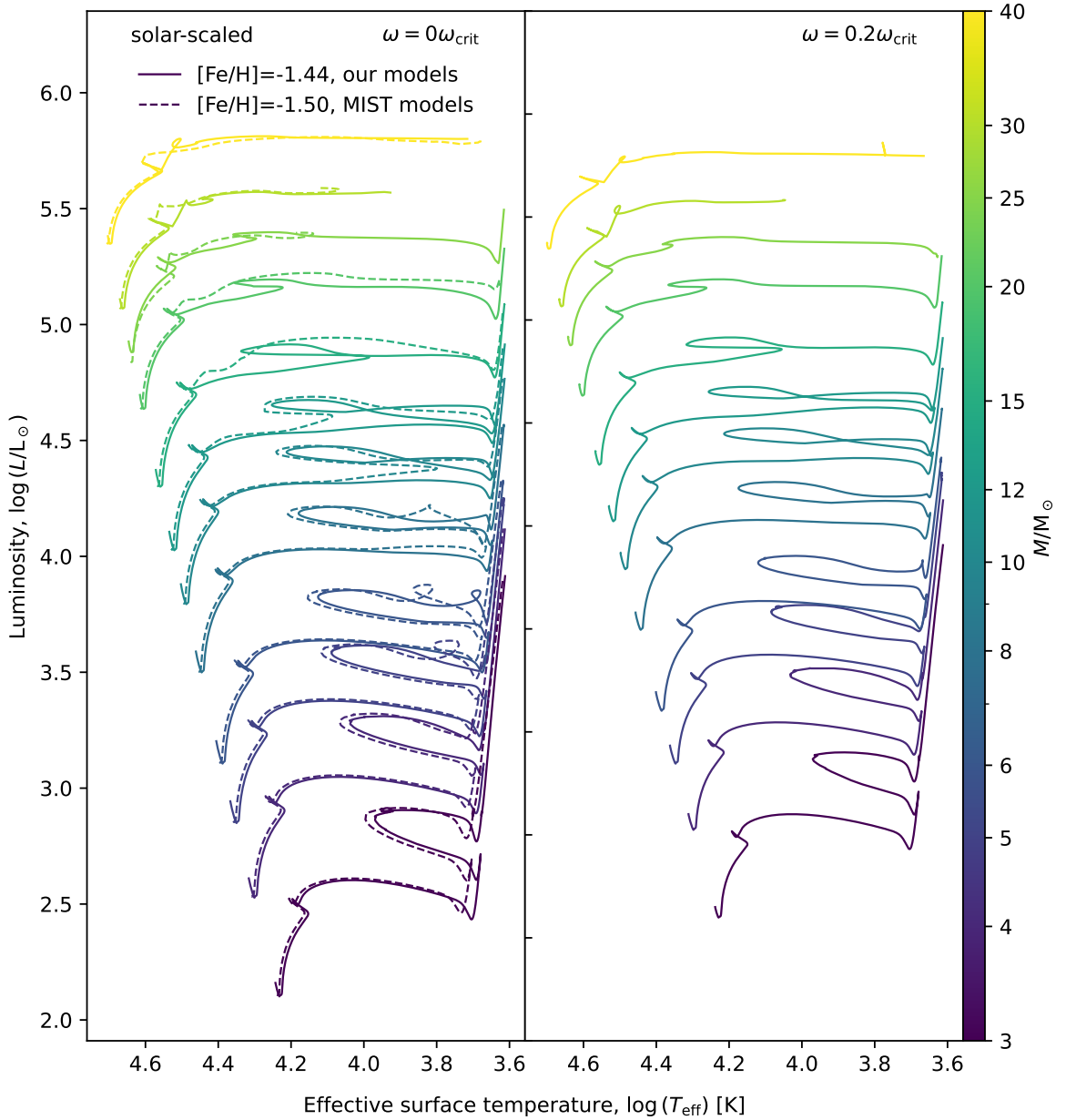


Figure 2.2: Single star evolutionary tracks for solar-scaled models. The left panel shows the non-rotating models, whereas the right panel shows the rotating models. Solid lines correspond to our set of models and dashed lines are for the MIST (v.1.2) models (Choi et al., 2016). These are at slightly different metallicities ($[\text{Fe}/\text{H}]$), and our $25M_{\odot}$ model (3rd track from the top) does not have a direct MIST counterpart. Instead, we show the $M = 24 M_{\odot}$ MIST model for comparison.

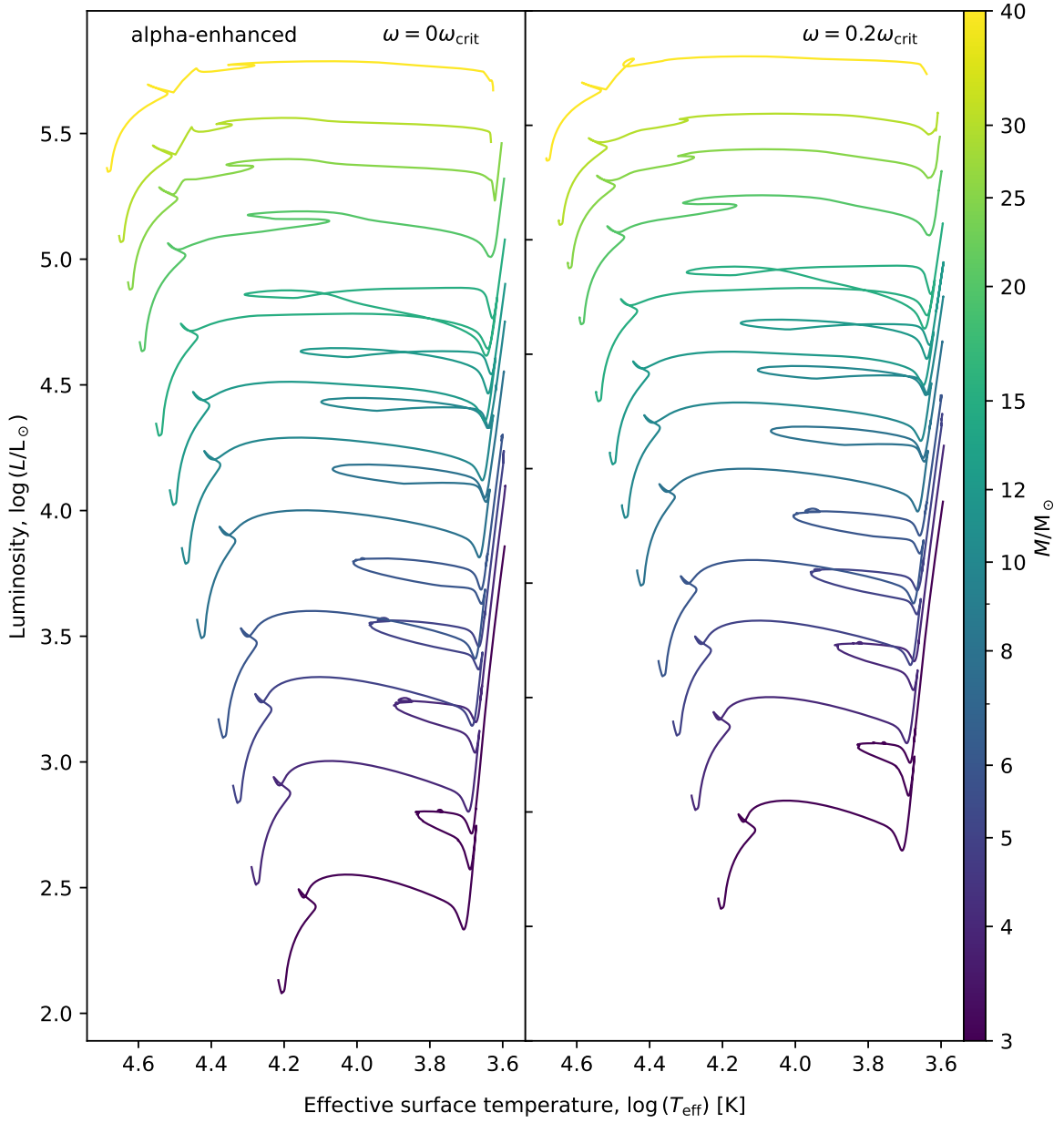


Figure 2.3: Our single star evolutionary tracks for alpha-enhanced models. Similar format to figure 2.2, however, we do not compare to MIST tracks in this since they do not have alpha-enhanced models available.

of core-C mass fraction dropping below 5×10^{-3} for these stars. Our lower mass singles will become white dwarfs after leaving the MS, so we impose `center_degeneracy` reaching above 10 as the end point for these stars. The `center_degeneracy` is the electron chemical potential μ_e in units of kT . For single star models that do not reach any of these stopping conditions, we increased `varcontrol_target` by 1×10^{-4} . If this still did not lead to convergence we increased it again by the same step. The only model that does not reach a stopping condition is the alpha-enhanced, rotating, $M = 25 M_\odot$ model, but it does ignite core-C reaching a central abundance of $\sim 16\%$. Based on the mass lost from other massive singles, this causes a negligible difference in the yields ($< 1\%$).

Due to a change in the nuclear burning rates, and subsequently the luminosity and radiation pressure, different evolutionary phases correspond to changes in radii. Events like ignition and depletion of elements in the core can correspond to peaks in the radius evolution of the star. Peaks in radii were detected using `find_peaks` from `scipy.signal` (Virtanen et al., 2020). We look for peaks in the log radius with widths of the log time step, with prominences of 7×10^{-3} , which was chosen through trial-and-error to detect both peaks for all primary masses. We note that for the higher mass stars $M \gtrsim 20M_\odot$, the peaks in radius can be less extreme or have multiple peaks near core-He ignition, in part owing to influences from shell burning and complex mixing regions.

From Eggleton (1983), the effective Roche lobe radius of the primary in a binary is approximated as

$$r_L = \frac{0.49q^{-2/3}}{0.6q^{-2/3} + \ln(1 + q^{-1/3})} a \quad (2.5.1)$$

where a is the binary separation. We solve for a when the Roche lobe exactly fills at each of the peaks in radius. By Kepler's laws, the semi-major axis is related to the period via the

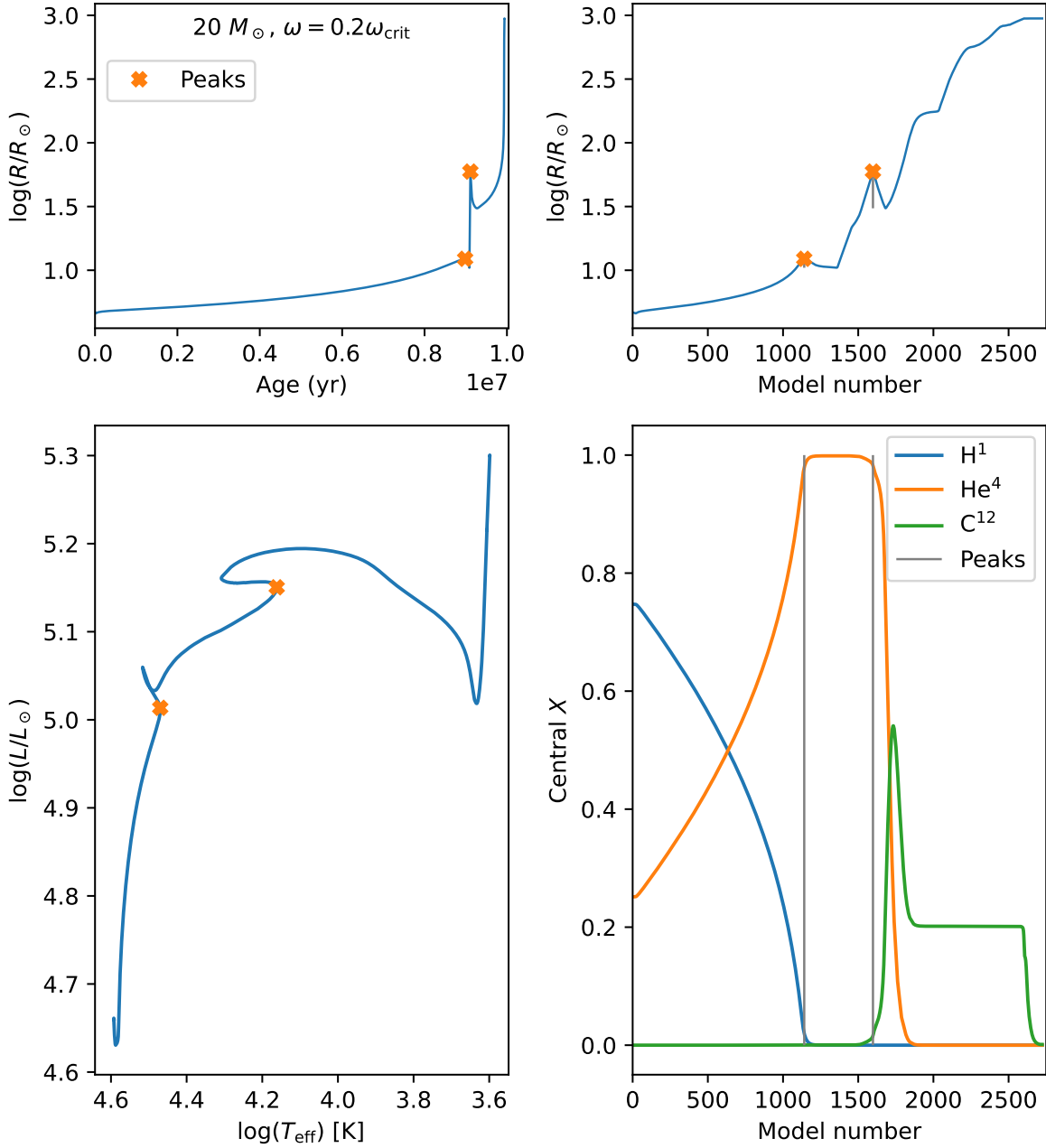


Figure 2.4: Evolution of an example single model, showing the radius evolution in the upper panels, the stellar track in the lower left, and the central abundances in the lower right. Orange crosses and grey vertical lines correspond to the identified peaks in radius. This model is alpha-enhanced, $20 M_{\odot}$, and starts with an initial rotation rate of $0.2\omega_{\text{crit}}$.

relation (e.g. Eggleton, 2011)

$$P^2 = \frac{4\pi^2}{G(M_1 + M_2)} a^3. \quad (2.5.2)$$

We verify the location of peaks by checking that the core composition and the location on the temperature-luminosity diagram at each peak are consistent with the relevant evolutionary phase. Period limits shift slightly ($\leq 1\%$) when accounting for the mass loss of the primary (via single-star winds). We show an example of the peaks and evolution for an alpha-enhanced single model in figure 2.4.

We choose to use period estimates based on solar-scaled singles. The alpha-enhanced singles tend to suggest larger period limits by typically 10% \sim 30%. As we sample the period using steps in $\log(P)$ and extend our P by an additional step above the upper period limit, the desired range of alpha-enhanced binaries is often still well covered. However, since the upper peak occurs during the Hertzsprung gap where stars move towards lower temperatures and larger radii relatively rapidly, the upper period limit varies substantially in some models. Although the period limits may vary greatly, the associated evolutionary time lag due to this is relatively small.

2.5.3 Alterations to our fiducial settings

For runs that did not reach core-C depletion or contact using our fiducial `inlist` settings, we adjusted their `varcontrol` settings and reran the simulations. We also vary `varcontrol` to check for convergence of results in a few runs.

For binaries, the `varcontrol` can change during mass transfer using `varcontrol_case_a` when the donor is on its MS and `varcontrol_case_b` when the

donor is past the MS. Outside of mass transfer, the `varcontrol` of the stars are set using `varcontrol_ms` and `varcontrol_post_ms` for the same scenarios. When issues arise during RLOF, we run with both `varcontrol_case` at 3×10^{-4} and 5×10^{-4} , compared to the default 4×10^{-4} . The `varcontrol_post_ms` are adjusted similarly. For `varcontrol_ms` however, we only increase it relative to the fiducial 1×10^{-4} . We test 2×10^{-4} for both alpha-enhanced and solar-scaled binaries but only check 4×10^{-4} for the alpha-enhanced models.

Table B.1 in the appendix lists all our alpha-enhanced models, their changes relative to our fiducial controls, stopping/exclusion conditions reached, and other notes. The list of solar-scaled binaries is in table B.2.

Chapter 3

Results

3.1 Yields of alpha-enhanced binaries

In this section we consider the yields from the alpha-enhanced binaries we simulated, exploring their properties as a set. As alpha-enhancement is typical to metal-poor stars, we emphasize these results.

3.1.1 The parameter space of enriching binaries

We plot the binaries alongside the stopping conditions or exclusion conditions in figure 3.1. Out of the 204 alpha-enhanced binaries we simulated, 190 are included in our main sample as they undergo non-conservative mass transfer. Out of the 190 binaries, 29 reach core-C depletion. In general, binaries that reach core-C depletion occupy the intermediate masses ($12 \lesssim M_1 \lesssim 25 M_\odot$). Binaries that initiate contact (34) occur at the lower period limit, as expected since closer binaries have smaller Roche lobes that are more easily filled. The 67 binaries that reach the sharp increase in the system mass loss rate, \dot{M} , are more present

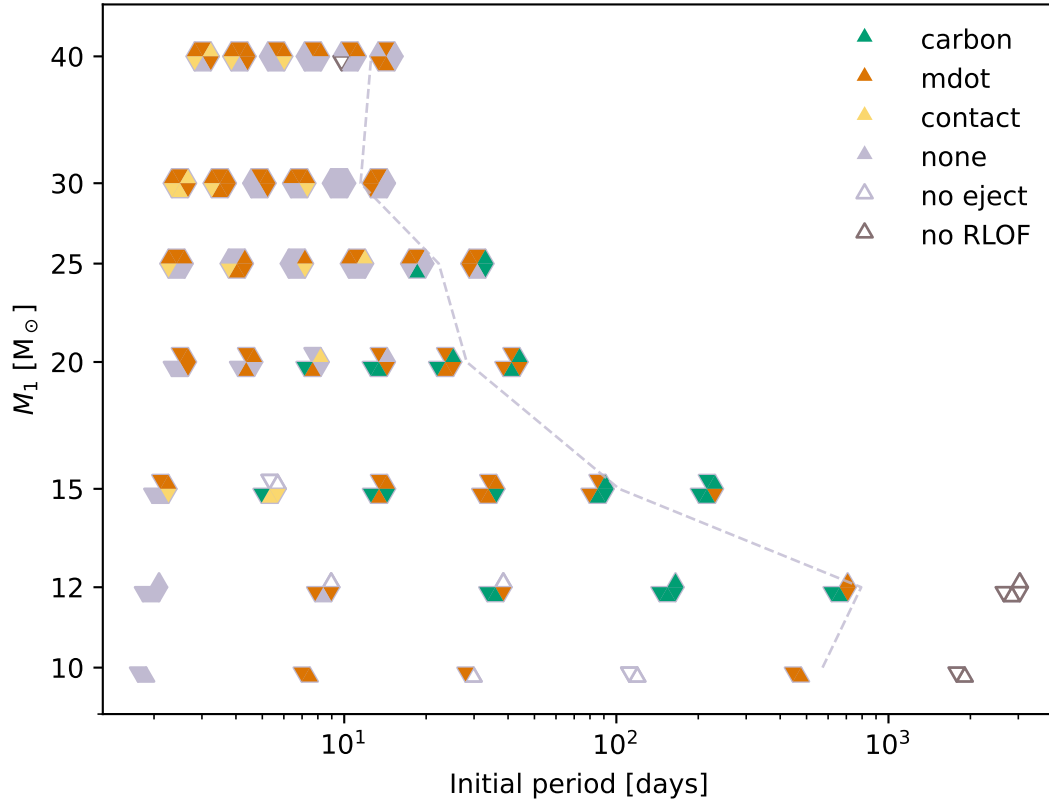


Figure 3.1: End-point conditions reached by each binary in the sample of 204 alpha-enhanced binaries. Filled-in triangles are included in our main sample and empty triangles are omitted. The layout of this figure follows figure 2.1. The colour of each point indicates the stopping condition reached by that binary. Out of the 190 binaries that we include in our main sample, 29 reach core-C exhaustion, 34 initiate contact, and 67 have sharp changes in their mass loss rates. A detailed description of these stopping conditions is in §2.4. 60 of the binaries do not reach any of these stopping conditions, however, we still include them in our sample as they undergo significant binary mass ejection. 14 out of 204 binaries are excluded for not meeting the minimum requirements.

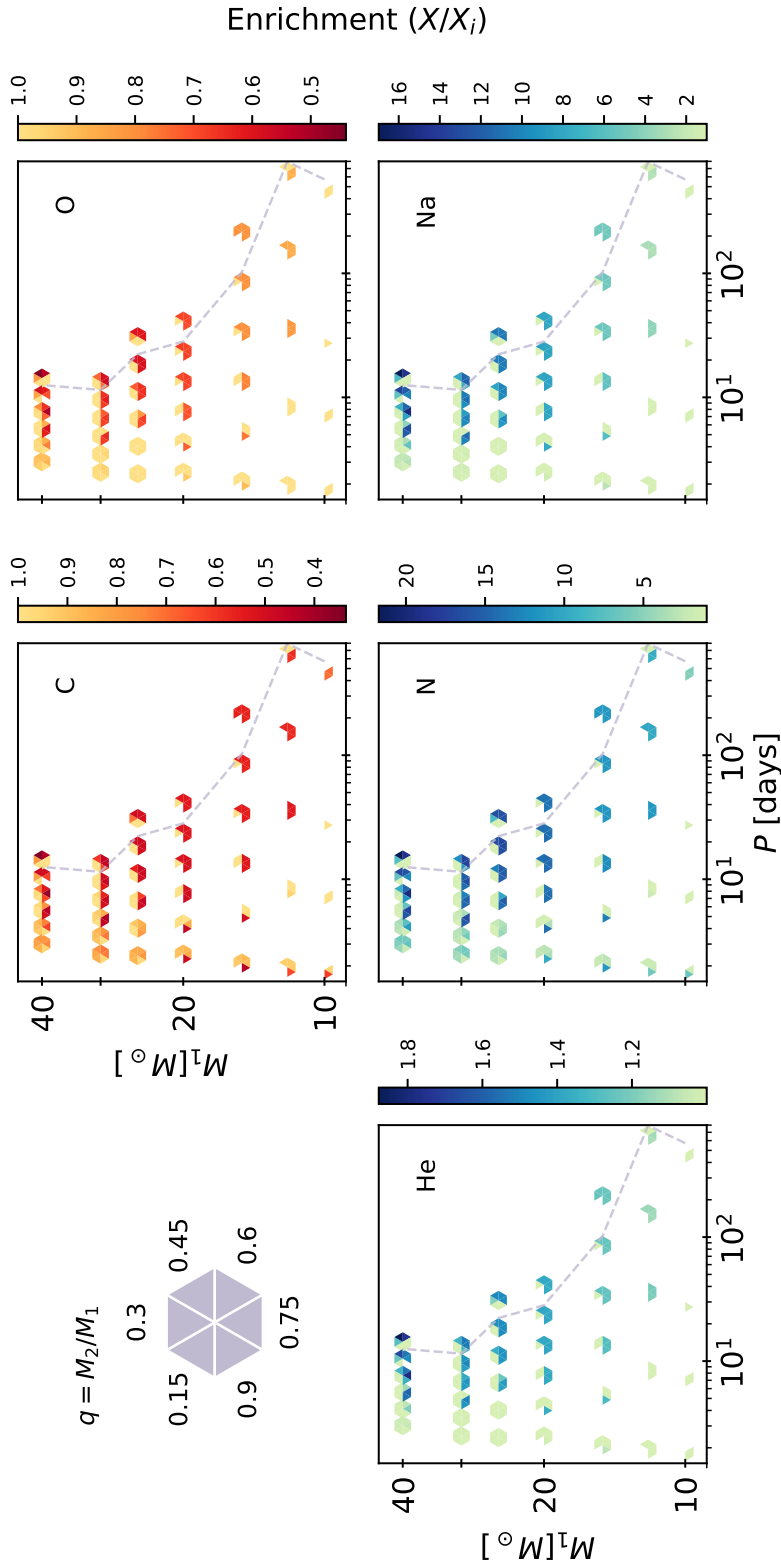


Figure 3.2: Enrichment of the total ejected material from each completed binary. The enrichment is the relative change in the mass fraction of the element compared to the initial ejected mass fraction (i.e. surface abundances), X/X_i . Values less than 1 indicate that element is depleted in the ejecta from that binary; values above 1 indicate enrichment. The colour indicates the strength of enrichment; darker values correspond to stronger depletion (top panels) or stronger enhancement (bottom panels). The strongest signals of enhancement are present at higher q , higher P , and higher M_1 . For these enriching binaries, the signals of enrichment seem qualitatively consistent with observations for all 5 elements.

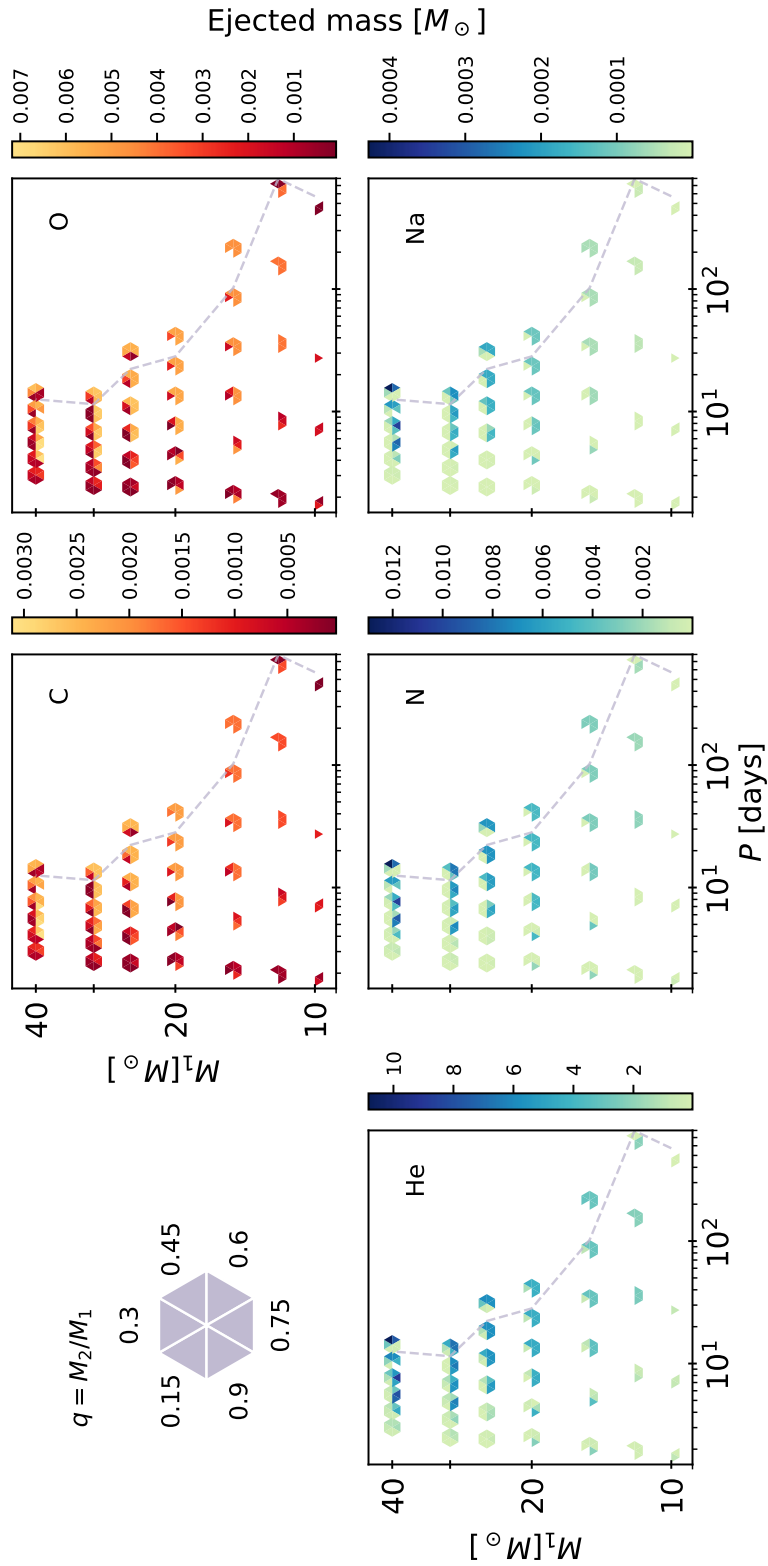


Figure 3.3: Absolute mass ejected in C, O, He, N, and Na for all massive interacting binaries in our simulations. This figure is similar to figure 3.2, however darker colours correspond to less mass ejected in the typically depleted elements (C, O) and more mass ejected in the enriched elements (He, N, Na). In contrast to the previous figure, the points that are relatively light in the upper panels (showing high ejected mass) were dark in the enrichment plot (showing strong depletion).

throughout all parameter space. These include runs that approach unstable mass transfer or are otherwise numerically unstable due to limitations of the code and input parameters to follow the evolution further.

The other 14 binaries did not meet our requirements of undergoing RLOF with an ejection of at least $0.1M_{\odot}$ and are excluded from our main sample. The 6 binaries with $M_1 = 10, 12 M_{\odot}$ outside the period limit do not initiate RLOF during their runs. This suggests that binaries at these primary masses and with the mass ratios we simulate ($q = 0.45, 0.6, 0.75, 0.9$ for $M_1 = 12 M_{\odot}$ and $q = 0.75, 0.9$ for $M_1 = 10 M_{\odot}$) will not initiate mass transfer at or above these periods. The $M_1 = 10 M_{\odot}$ primaries only fill about 75% of their Roche lobes, and the $M_1 = 12 M_{\odot}$ fill $\sim 60\%$. We fully cover the range of periods that will undergo mass transfer for $M_1 = 12, 15 M_{\odot}$ past core-H depletion.

One binary at high mass, with $M_1 = 40 M_{\odot}$, $P = 10.47$ days, $q = 0.9$, also does not initiate RLOF. We suspect that this is due to difficulty in simulating the initiation of mass transfer concurrently with core-He ignition in a high mass primary. 7 systems at intermediate periods with $10 \leq M_1 \leq 15 M_{\odot}$ initiate RLOF but do not eject greater than $0.1M_{\odot}$. These runs stalled with time steps of about $10^{-2} \sim 10^{-3}$ years, with reruns and/or resumes not showing any significant improvement.

We define the value X/X_i as the enrichment. This is similar to the definition used by de Mink et al. (2009) for their figure 1. We normalize the mass fraction of a chosen element for the entire ejecta of the binary, X , by the initial mass fraction of that element lost during the first time step for that system. So, X/X_i describes the relative change in mass fraction for an element compared to the initial surface abundances. For the elements ubiquitously observed to vary in multiple populations (C, O, He, N, Na) we show the enrichment for each system in our main sample in figure 3.2. Points that are darker in these plots have ejecta

with stronger enrichment signals (associated with more extremely enriched populations) than lighter points. From panel to panel, the enhancement of He, N, and Na generally corresponds to the depletion of C and O at similar relative levels (indicated by colour value). Systems with high initial primary masses $M_1 = 40 M_\odot$ consistently set the strongest enrichment signals. The strength of enrichment weakens with mass more strongly in He, O, and Na than in C and N. From figure 3.2, enriching binaries (darker value points) tend to have higher primary masses $M_1 \gtrsim 12$ (top of the plots), higher $q \gtrsim 0.45$ (bottoms and upper right of hexagons), and are at longer periods (right of plots, near period limit). Binaries with lower mass primaries $M_1 \lesssim 20 M_\odot$ at the lowest periods we simulate ~ 2 days, and at the highest mass ratio $q = 0.9$ also exhibit relatively strong signs of enrichment. These binaries have larger C depletion and N enhancement, but relatively small changes in He, Na, and O indicating the ejection of less-processed material. For higher mass primaries with the same mass ratio and similar periods, enrichment is not observed. These systems are stopped by reaching contact phases.

In figure 3.3 we present the absolute mass ejected in HeNaCNO, rather than the relative enrichment shown in figure 3.2. Many of the trends are similar to the enrichment trends when considering the enhanced elements. However, the systems that eject strongly depleted C and O in terms of X/X_i are shown to eject high masses of C and O. This suggests that the strength of enrichment correlates with the total amount of mass ejected from the binary.

In our parameter space, there are systems that show little-to-no signs of processing with $X/X_i \sim 1$ in HeNaCNO. This suggests that non-conservative mass transfer can not only provide enriched gas but can also provide pristine gas for dilution.

To further illustrate some of the trends seen in the hexagonal plots we make scatter plots of the enrichment in HeNaCNO as a function of the fraction of the initial system mass that

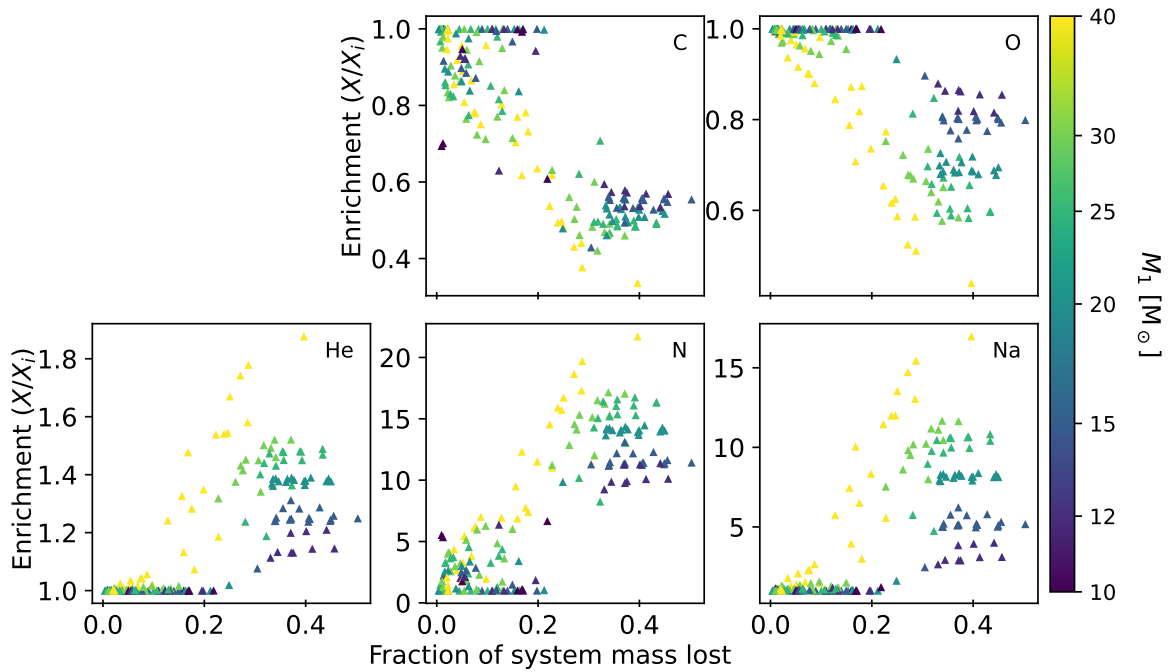


Figure 3.4: Scatter plots of the enrichment, X/X_i , in different elements (C, O, He, N, Na) as a function of the initial system mass lost. The fraction of system mass lost is the (total mass ejected)/($M_1 + M_2$). Each point corresponds to the yields of a simulated binary in our main, alpha-enhanced sample. The colour of the points corresponds to the initial primary star mass of the binary.

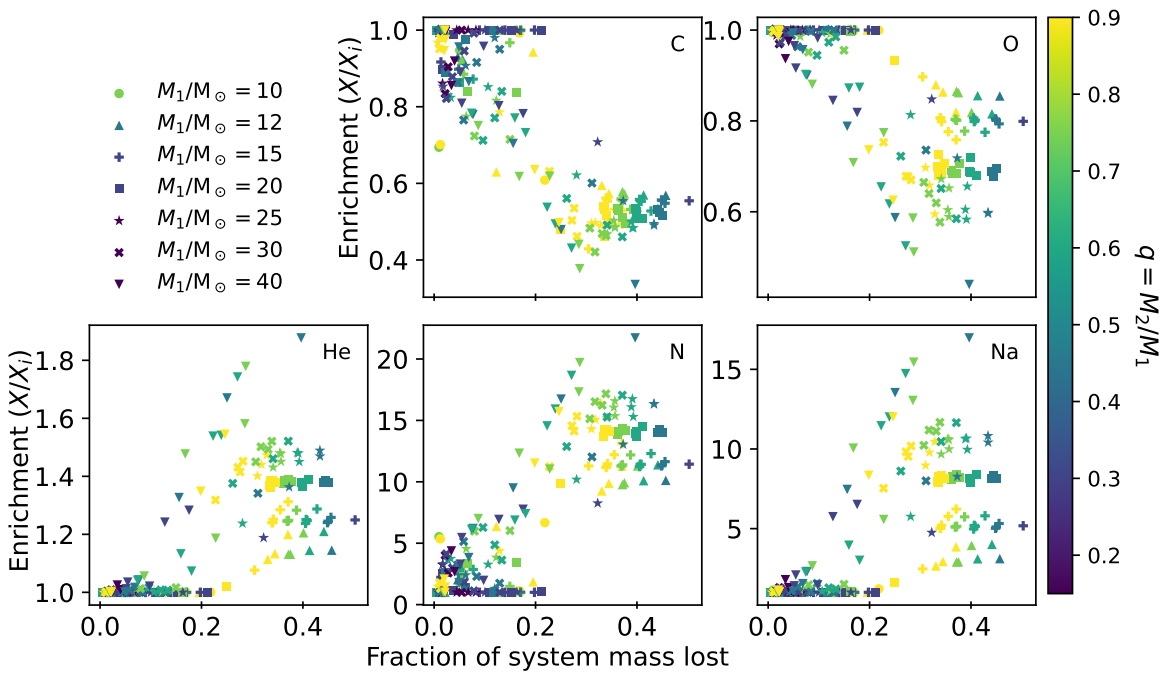


Figure 3.5: Scatter plots of enrichment against the fraction of system mass lost, similar to figure 3.4, though the colour now corresponds to the mass ratio $q = M_2/M_1$. The shape of the points now indicates the initial primary mass of the binary.

has been ejected. We calculate the fraction of system mass loss as the total mass ejected at the end of the simulation (up until a stopping condition) divided by the initial system mass ($M_1 + M_2$). In figure 3.4 we show these scatter plots with the colour corresponding to the initial primary mass. Figure 3.5 shows the same points with the colour map showing the initial mass ratio q instead. The enriching binaries are lower for the upper panels showing depleted elements and higher for the enhanced elements shown in the bottom row.

In general, less enriching binaries with $X/X_i \sim 1$ eject a smaller fraction of mass. A transition appears when around 20% of the system mass has been ejected. We also see that the maximum fraction of system mass lost is around 50% of the initial system. However, there is a larger spread in C and N at the low ejected mass fraction end (~ 0), compared to the spreads seen in He, Na, and O.

From figure 3.4 focusing on each colour, higher enrichment is reached with increasing mass at the same relative fraction of system mass lost. Although these systems are ejecting similar fractions of their primary envelopes, this fraction is generally more enriched in binaries with higher mass primaries. A couple of binaries with $M_1 = 10 M_\odot$ exhibit large changes in C ($X/X_i \sim 0.5$) and N ($X/X_i \sim 5$) at low fractions of system mass lost (~ 0), with practically no change in the other three elements. This suggests that binaries with low masses that do not eject a significant portion of their envelopes do not expose the hot-H burned material consistent with enrichment in multiple populations.

Focusing on the He, O, or Na panel and on the $20 M_\odot$ primaries transition from having $X/X_1 \sim 1$ at low fractions of system mass ejected to having their extreme X/X_i in a plateau. This behaviour is observed in the other primary masses. However, for the $40 M_\odot$ primary mass binaries, this does not appear to hold.

Visually the binaries with $M_1 \leq 20 M_\odot$ have two plateau-like regions in enrichment,

which at higher masses transition to a more linear-like trend with the fraction of system mass loss. This indicates a more efficient mixing of hot-H-burned material towards the surface of the stars, with higher primary masses. It also implies that for lower-mass systems, binary mass transfer must eject a larger proportion of their mass to provide enrichment.

Comparing the enriching binaries shown in figure 3.4 to their mass ratio in figure 3.5 we see that lower mass ratios can provide the same level of enrichment as higher mass ratio systems while ejecting a larger fraction of the system mass. To determine the cause of this pattern, we checked the evolution of the binaries in their evolutionary tracks; central H, He, and C abundances; relative Roche lobe overflow; masses; radii; mass loss rates; orbital period; and rotation rate, $\omega/\omega_{\text{crit}}$. Comparison of the mass evolution of the stars in 3 binaries with $M_1 = 12 M_{\odot}$ and $P = 154.16$ days, where they all terminated by reaching core-C depletion, reveals that the primary loses a similar amount of mass in each system. The offset in the fraction of system mass lost for these binaries is due to the mass of the secondary increasing the initial system mass lost. A comparison of two $M_1 = 25 M_{\odot}$ and $P = 30.84$ days binaries which also reached core-C depletion behaved similarly. There may also be additional effects from the amount of mass accreted by the secondary and the impact of tidal forces on rotation rates and rotational mixing. However, rotation rates and the mass change of the secondary are relatively similar in these runs. We note that in general, the secondary in our binaries do not change mass substantially (increases $< 1 M_{\odot}$).

This trend holds for $12 \leq M_1 \leq 30 M_{\odot}$ but does not appear to be true for $M_1 = 40 M_{\odot}$. Our main sample only has 7 completed binaries with $M_1 = 10 M_{\odot}$ so it is not apparent whether they follow the same trend. None of the $M_1 = 10$ or $40 M_{\odot}$ reach core-C depletion (see figure 3.1). It may be that if all simulations could be run to late evolutionary stages, this trend would appear at all masses. This would be consistent with a fairly constant fraction

of the primary envelope being ejected at a given mass, for the q and P we simulate.

3.1.2 Abundance enrichment and depletion in binary ejecta

We consider the ability of binaries to match the various abundance trends associated with MPs by first considering the entire sample. In table 3.1 we present the extremes and the median enrichment in each element that we track the ejection of. If the median $X/X_i > 1$, the binaries in our sample typically enhance that element; if it is less than one we consider it to be depleted. We set a tolerance of 0.01 and anything within this of 1 is considered to not typically change.

Based on this selection we find Mg, Fe, H, Si, Ca, Ti, Ni, and Cr do not change. Of these, Cr is unusual as we set up our initial composition to have no Cr for consistency with how solar-scaled ZAMS models are set by MESA. However, the enhanced Cr is at a level of $N_{\text{Cr}} \sim 10^{-94} N_{\text{H}}$ at most which is insignificant (i.e. the “enhancement” is numerical). Elements from atomic numbers $21 \leq Z \leq 32$ are considered part of the iron-peak elements. These elements generally vary together and are produced with extreme, often explosive burning, $T \gtrsim 5 \times 10^9$ K (Ernandes et al., 2018). This includes Ti, Cr, Fe, and Ni. Mg, Si, and Ca are lighter alpha elements. In some systems, H is considerably depleted ($X/X_i < 1$), and this is expected with the ejection of H-burned, He-enhanced material. Since the mass fraction of H is a few factors larger than He (the second largest mass fraction), the factor that H decreases by is relatively small.

C, O, Li, Be, B, and F are all depleted. Enhancement is observed in He, N, Na, and Al. Li, Be, and B are fragile elements that can easily be destroyed at high temperatures (Randich & Magrini, 2021). C and O depletion alongside enhancement in He, N, and Na is ubiquitous in MPs (Milone & Marino, 2022).

Element	Min. X/X_i	Min. X/X_i binary	Max. X/X_i	Max. X/X_i binary	Median X/X_i	General change
C	0.336	40m1_18.0m2_14.29d	1.0001	15m1_4.5m2_85.33d	0.7728	depleted
O	0.4399	40m1_18.0m2_14.29d	1.0	40m1_6.0m2_14.29d	0.9562	depleted
Mg	0.963	40m1_18.0m2_14.29d	1.0	12m1_5.4m2_1.95d	0.9988	no change
He	1.0	40m1_6.0m2_14.29d	1.8772	40m1_18.0m2_14.29d	1.0167	enhanced
N	1.0	25m1_3.75m2_30.84d	21.7173	40m1_18.0m2_14.29d	5.7567	enhanced
Na	1.0	40m1_6.0m2_14.29d	16.973	40m1_18.0m2_14.29d	1.4892	enhanced
Al	1.0	12m1_7.2m2_8.37d	2.2095	40m1_18.0m2_14.29d	1.0369	enhanced
Li	0.0018	15m1_13.5m2_2.11d	0.6839	40m1_18.0m2_10.47d	0.0194	depleted
Fe	1.0	40m1_30.0m2_7.67d	1.0	40m1_36.0m2_14.29d	1.0	no change
H	0.7057	40m1_18.0m2_14.29d	1.0	40m1_6.0m2_14.29d	0.9944	no change
Be	0.0211	20m1_18.0m2_2.49d	0.9977	20m1_6.0m2_7.65d	0.145	depleted
B	0.0231	20m1_18.0m2_2.49d	0.9979	20m1_6.0m2_7.65d	0.1398	depleted
F	0.3519	40m1_18.0m2_14.29d	1.0005	12m1_10.8m2_8.37d	0.9499	depleted
Si	1.0	10m1_7.5m2_7.47d	1.0007	40m1_18.0m2_14.29d	1.0	no change
Ca	1.0	40m1_30.0m2_7.67d	1.0	40m1_36.0m2_14.29d	1.0	no change
Ti	1.0	40m1_30.0m2_7.67d	1.0	40m1_36.0m2_14.29d	1.0	no change
Ni	1.0	40m1_30.0m2_7.67d	1.0	40m1_36.0m2_14.29d	1.0	no change
Cr	0.9999	10m1_9.0m2_29.86d	3588166.238	40m1_30.0m2_10.47d	1.0	no change

Table 3.1: Maximum, minimum, and median enrichment, X/X_i , observed in each element of the ejecta of the alpha-enhanced binaries. Based on the median of the X/X_i for all binaries, we label whether the element is depleted ($(X/X_i)_{\text{med.}} < 1$) or enhanced (> 1). Elements where $(X/X_i)_{\text{med.}} \sim 1$ (within 1%) are listed as having no change. Cr is included in our network and tracked in the ejecta, but is not initially included for congruence with the solar-scaled compositions set by MESA. For all elements, the binary where the extreme was produced is mentioned.

The extremes correspond to the maximum possible spread in that abundance for an enriched population forming out of the ejecta from the binaries we simulated. Of the canonical elements associated with MPs (HeNaCNO), the largest spread is observed in N with up to a factor of $\sim 22\times$ enhancement corresponding to a spread of about 1.3 dex. For the majority of altered (generally enhanced/depleted) elements, the binaries with the most extreme depletion/enhancement are binaries with $M_1 = 40 M_\odot$, except for Li, Be, and B which occurred in binaries with $M_1 = 15, 20 M_\odot$.

3.1.3 Main abundance correlations observed in multiple populations

Considering the entire set of binaries, we check if massive binary ejecta reproduces the observed abundance trends in MPs in GCs. Mixing of the ejecta of binaries will only result in abundances within the extremes. As several binaries in our sample eject mass that is consistent with the initial composition, dilution will have a similar effect. To assess the significance of the correlation we use a two-sided Spearman rank test, reporting both the Spearman coefficient r_s and the probability of the data corresponding to an uncorrelated data set, p . We calculate the statistic using `scipy.stats.spearmanr` and use `scipy.stats.permutation_test` with the default number of resamples (9999) with permutations done as ‘pairings’ to calculate the p -value. An $|r_s| = 1$ indicates a perfectly monotonic correlation between the two variables. Lower r_s values correspond to weaker correlations. The sign of r_s indicates if the correlation is a positive correlation or an anti-correlation. We round the r_s and p calculated to three decimal places.

For comparison to observations, we calculate the abundances of metals as

$$[X/Fe] = \log(N_X/N_{Fe}) - \log(N_{X,\odot}/N_{Fe,\odot}), \quad (3.1.1)$$

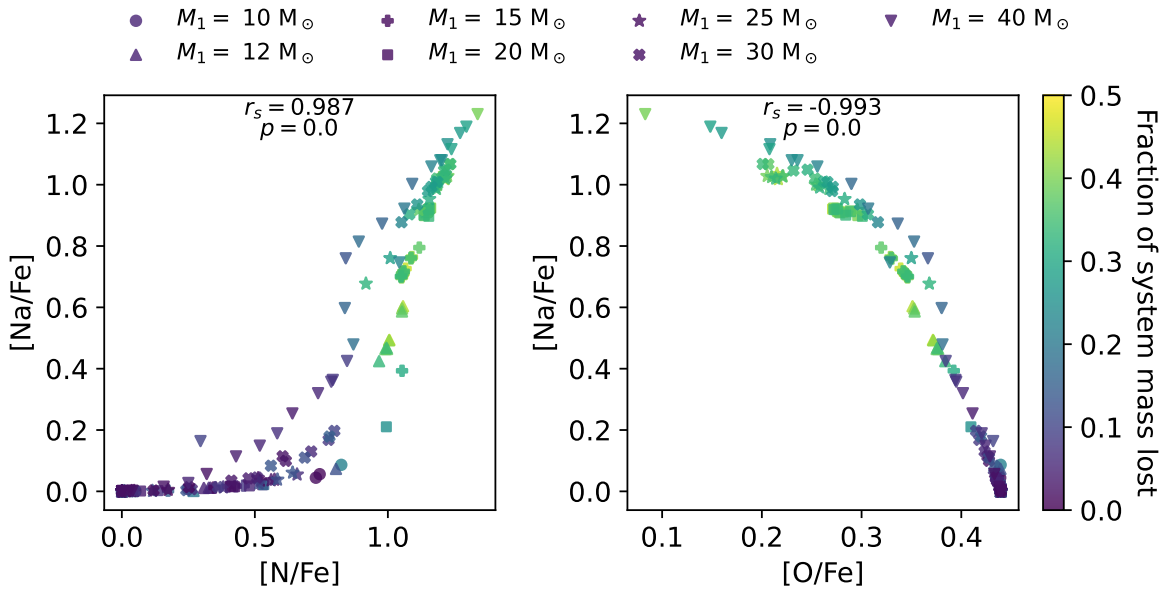


Figure 3.6: Na-N correlation and Na-O anti-correlation of the ejected mass from each binary in our main alpha-enhanced models. The elemental abundances are presented as $[X/Fe]$. The fraction of initial system mass lost from the binary is shown in the colour map. Different symbols correspond to different initial primary masses. More enriching binaries will have their ejecta in the upper right of the Na-N plots (high Na and high N) and the upper left of the Na-O plots (low O). At the top of each panel are the Spearman rank coefficients and the associated p -value (rounded to 3 decimal places) for the data arising from an uncorrelated data set.

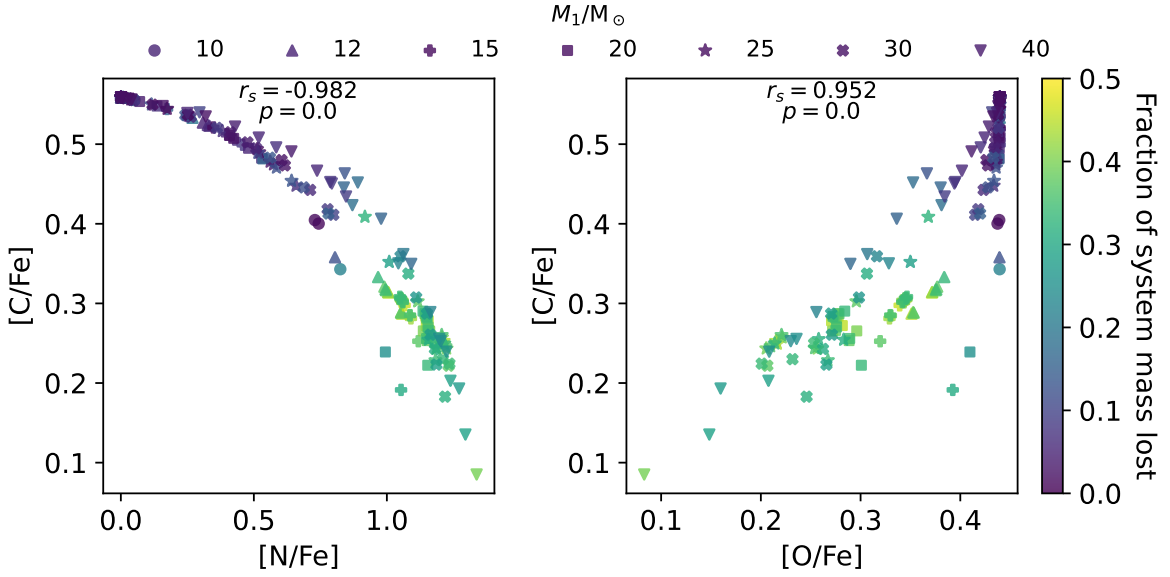


Figure 3.7: C-N anti-correlation and C-O correlation in the ejecta of alpha-enhanced binary models. Similar presentation to figure 3.6.

getting N_X by dividing the total mass in element X by the most common isotope.

Figure 3.6 shows the Na-N and Na-O relationships for our binary ejecta. We see that the ejecta has the Na-N correlation and Na-O anti-correlation as expected for an enrichment source. The Na-O anti-correlation is stronger than the Na-N correlation ($r_s = -0.993$ compared to $r_s = 0.987$). Comparing the scatter in the figures, it is apparent that for the same [N/Fe], binaries with higher mass primaries have higher levels of [Na/Fe] ejected compared to binaries with lower mass primaries. Equivalently, for the same [Na/Fe], ejecta from higher mass primaries has less [N/Fe]. However, they have similar [O/Fe] at the same [Na/Fe] even with different masses. The different behaviour seen in the enrichment of N in figure 3.4 affects the correlation relation between Na-N. This suggests higher mass binary ejecta can introduce scatter into the abundance correlations, compared to lower mass primary systems.

We note that the spread in [N/Fe] is large even for small changes in [Na/Fe] abundance.

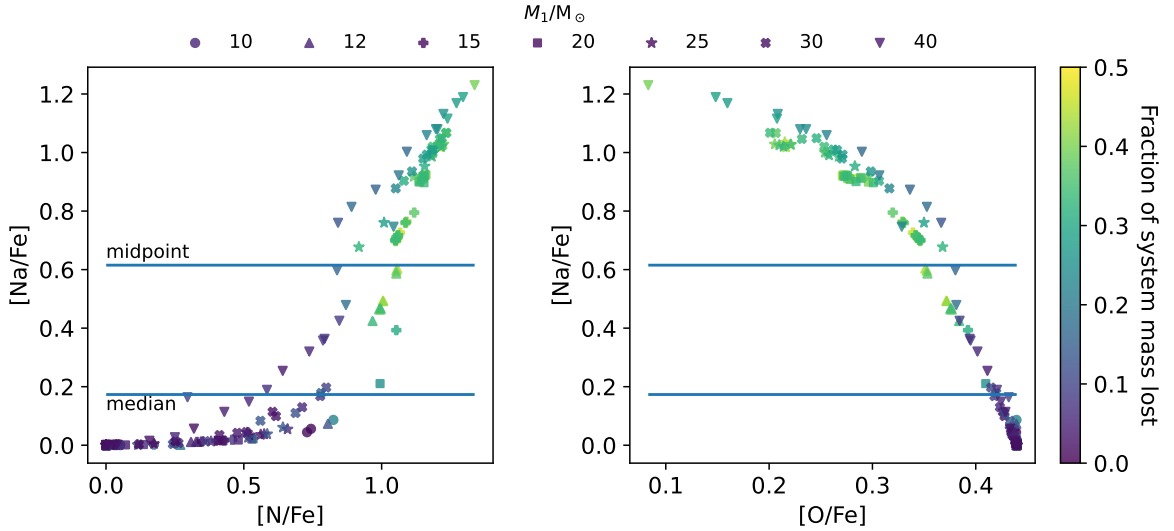


Figure 3.8: The [Na/Fe] thresholds (horizontal lines) we use for ejecta from simulated alpha-enhanced binaries. The underlying plot is the same as figure 3.6. The midpoint lies at 0.615 and the median at 0.173 dex.

Figure 3.7 explores the C-N anti-correlation and C-O correlation for our binary ejecta. Both correlations are present in the ejected material from the massive binaries, consistent with the expectation for an enrichment source. The C-N anti-correlation is similar to the Na-N correlation where the difference in N enrichment affects the scatter. The C-O correlation is the weakest of the ones we plotted so far ($r_s = 0.952$). The variation in [C/Fe] at higher [O/Fe] appears in systems with primary masses $10 \leq M_1 \leq 20 M_\odot$. Comparing the enrichment X/X_i in C and O from figure 3.4 we see that the enriching binaries (fraction of system mass lost ≥ 0.2) fill a relatively narrow range in C but a much wider range in O. Examining figure 3.7, in terms of the symbols which indicate mass, suggests the [C/O] ratio ejected is impacted by the primary mass of the binaries.

3.1.4 Predictors of strength of enrichment

To explore how binary mass transfer can effectively provide enrichment, we divide the binaries into two categories based on their ejecta: enriching and non-enriching (or weakly enriching). We use two different thresholds to divide the binaries, basing both of them on the [Na/Fe] abundance of their yields: the median and the midpoint. We illustrate this cut in figure 3.8. The midpoint lays well above the median by ~ 0.44 dex, indicating that the [Na/Fe] produced by most of our binaries would cause a small spread in [Na/Fe] with a small proportion producing more extreme spreads.

The goal of this analysis is not to provide a quantitative description of how enriching binaries can be based on their parameters or evolution (ex. through an analytic fit). Instead, we test the statistical strength of the trends seen in earlier figures. We use the Anderson-Darling test (implemented in `scipy.stats.anderson_ksamp`, Scholz & Stephens, 1987) to compare the distributions of binaries divided by these cuts, in M_1 , q , P , and the fraction of mass lost.

In figure 3.9 we show the M_1 distributions for both cuts. The p -value for the midpoint threshold is 0.029, suggesting the distributions are distinct at a confidence of $\sim 98\%$ and the p -value for the median cut is 0.172 indicating low confidence $\sim 83\%$. The $M_1 = 10 M_\odot$ binaries are not above either threshold. More $M_1 = 15$ and $20 M_\odot$ binaries are more enriching than those that are not. A large fraction of the $M_1 = 40 M_\odot$ binaries lies between the midpoint and median cut, compared to other primary masses.

The same comparisons but for q , P , and fraction of mass lost distributions are shown in figures 3.10, 3.11, and 3.12, respectively. For both cuts and for all of these quantities, the distributions are different from one another between enriching and non-enriching binaries at high confidence (Anderson-Darling $p < 0.001$). As such, the trends we saw visually

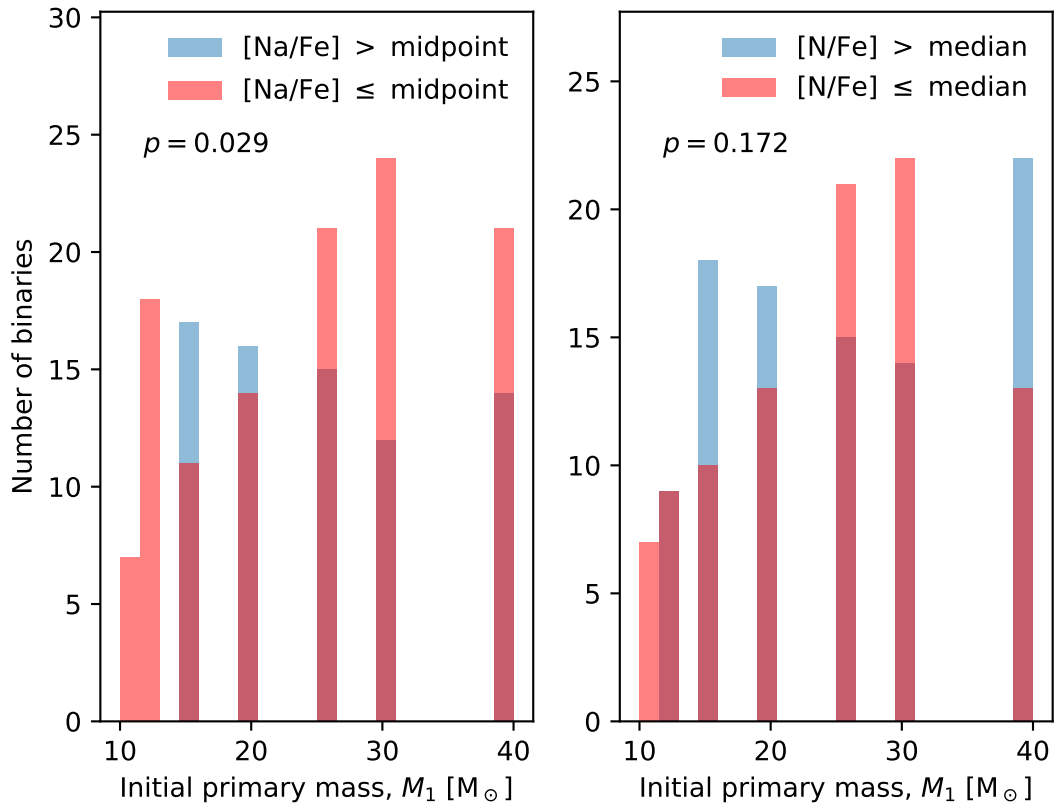


Figure 3.9: Distributions of the initial primary mass for binaries separated by the $[Na/Fe]$ they eject. Each panel shows the result for a different threshold (midpoint or median), which is shown in figure 3.8. The p -value annotated from the plot is the probability that the two distributions share the same underlying distribution, calculated from the Anderson-Darling test.

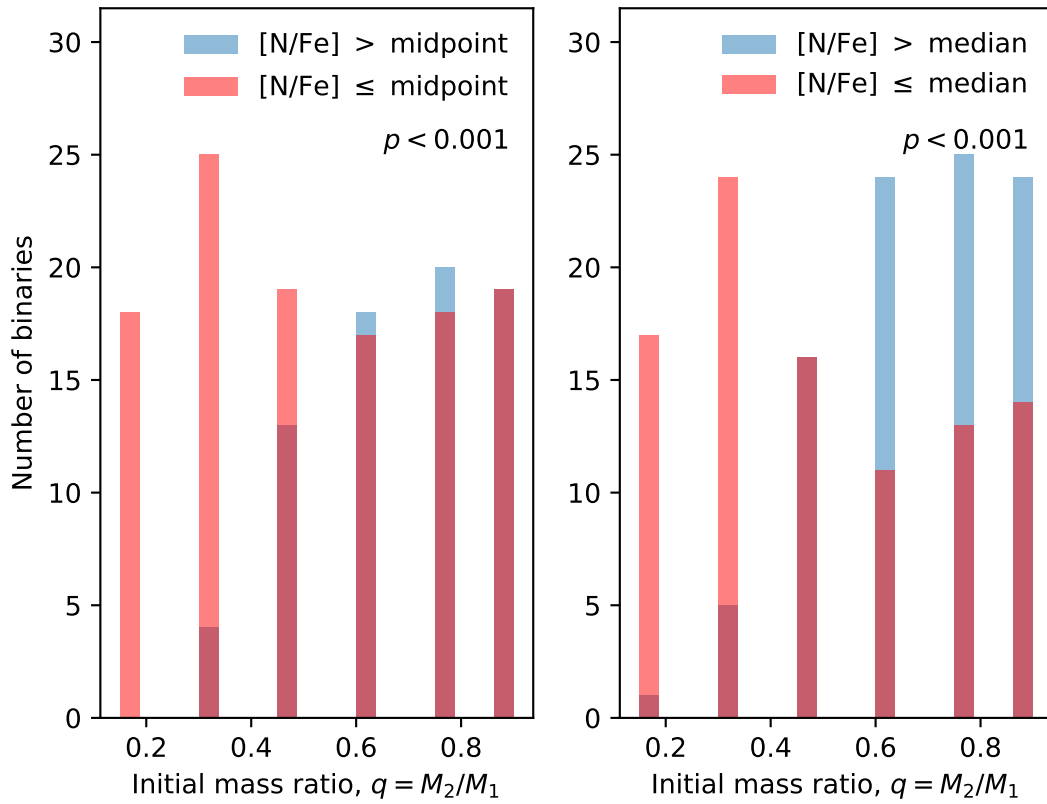


Figure 3.10: Mass ratio (q) distributions of binaries based on the $[Na/Fe]$ of their ejecta, similar to figure 3.9.

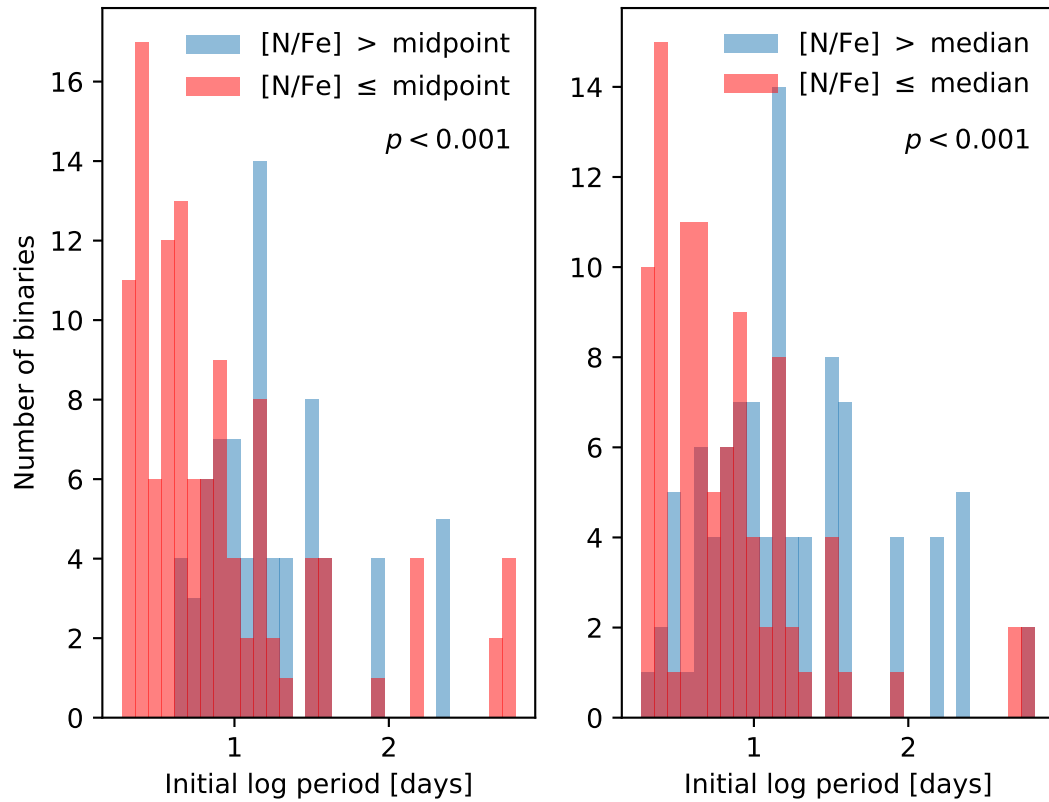


Figure 3.11: Initial period (P) distributions of binaries based on the $[Na/Fe]$ of their ejecta, similar to figure 3.9.

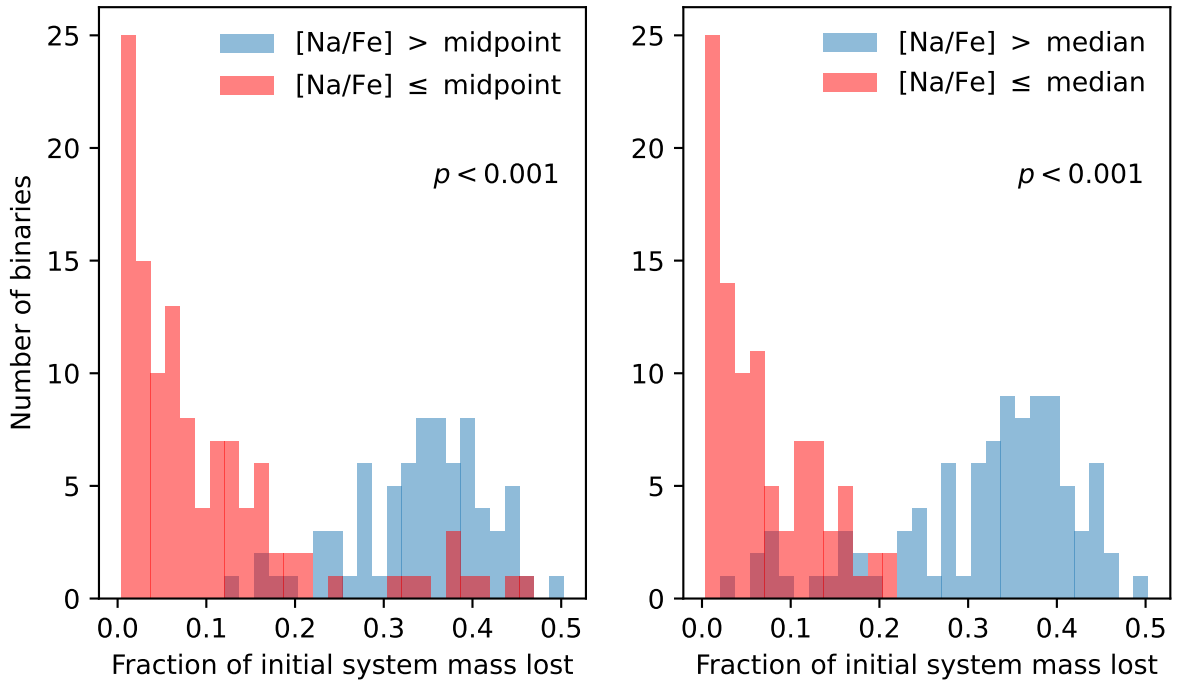


Figure 3.12: Distributions of the fraction of initial system mass lost by each binary, where binaries have been split based on their $[\text{Na}/\text{Fe}]$ ejected, similar to figure 3.9.

in earlier sections (e.g. figure 3.2) are statistically significant. We reiterate that enriching binaries tend to have higher mass ratios and longer orbital periods and lose a larger fraction of their initial mass compared to non-enriching binaries. Note that the ranges of P and q that we simulate depend on M_1 , and the fraction of mass lost is dependent on q , so none of these distributions are independent of the others.

3.1.5 Timescales for non-conservative mass transfer in massive interacting binaries

The timescale on which these systems eject mass is an important factor in their ability to act as an enrichment source. Mass transfer and the associated mass ejection in all of the binaries we simulate happens on an extremely short timescale ($\lesssim 0.5$ Myr) compared to the evolution of the system leading up to that point. For systems that undergo multiple phases of mass transfer, the second phase ejects less mass than the first. In figure 3.13 we show an example system with initial parameters of $M_1 = 25 M_\odot$, $M_2 = 11.25 M_\odot$, $P = 30.84$ days. The primary overflows its Roche lobe for $\lesssim 3\%$ of its total lifetime and loses most of the mass it ejects over $\lesssim 0.3\%$ of its age. As such, we choose to associate a single time of mass ejection for all of the binaries in our samples. For all of our systems in our main sample, the onset of RLOF as defined by the age of the stars (t) when the primary’s effective radius is first equal to the effective Roche lobe radius:

$$\min [t(R_1 \geq R_{1,\text{RLO}})] \quad \text{Onset of RLOF} \quad (3.1.2)$$

For reference, 3.14 shows the timescale of mass transfer for the binaries against their initial properties M_1 and P . This highlights how the initial mass sets the range where RLOF

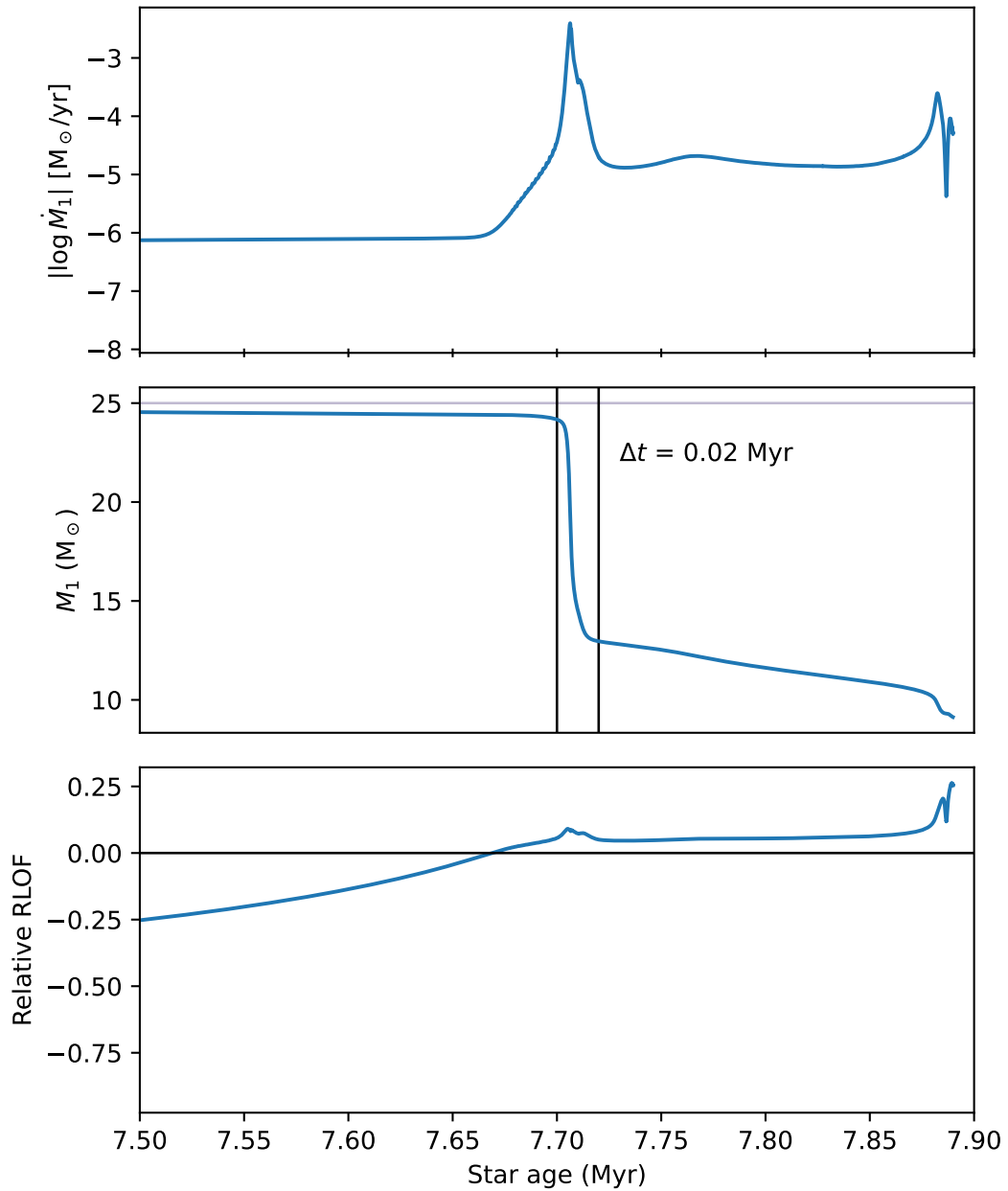


Figure 3.13: Absolute mass loss rate (top panel), mass (middle), and relative RLOF (bottom panel) of the primary in the $M_1 = 25 M_\odot$, $M_2 = 11.25 M_\odot$, $P = 30.84$ days, alpha-enhanced binary, over time. The relative RLOF of the primary is $(R_1 - R_{\text{RL},1})/R_{\text{RL},1}$. RLOF happens as the relative RLOF crosses the horizontal line at zero. This primary is overflowing its Roche lobe for ~ 0.2 Myr but loses $\sim 12 M_\odot$ shortly after initiating RLOF over just ~ 0.02 Myr. Another $\sim 3 M_\odot$ is lost during the remainder of the simulation.

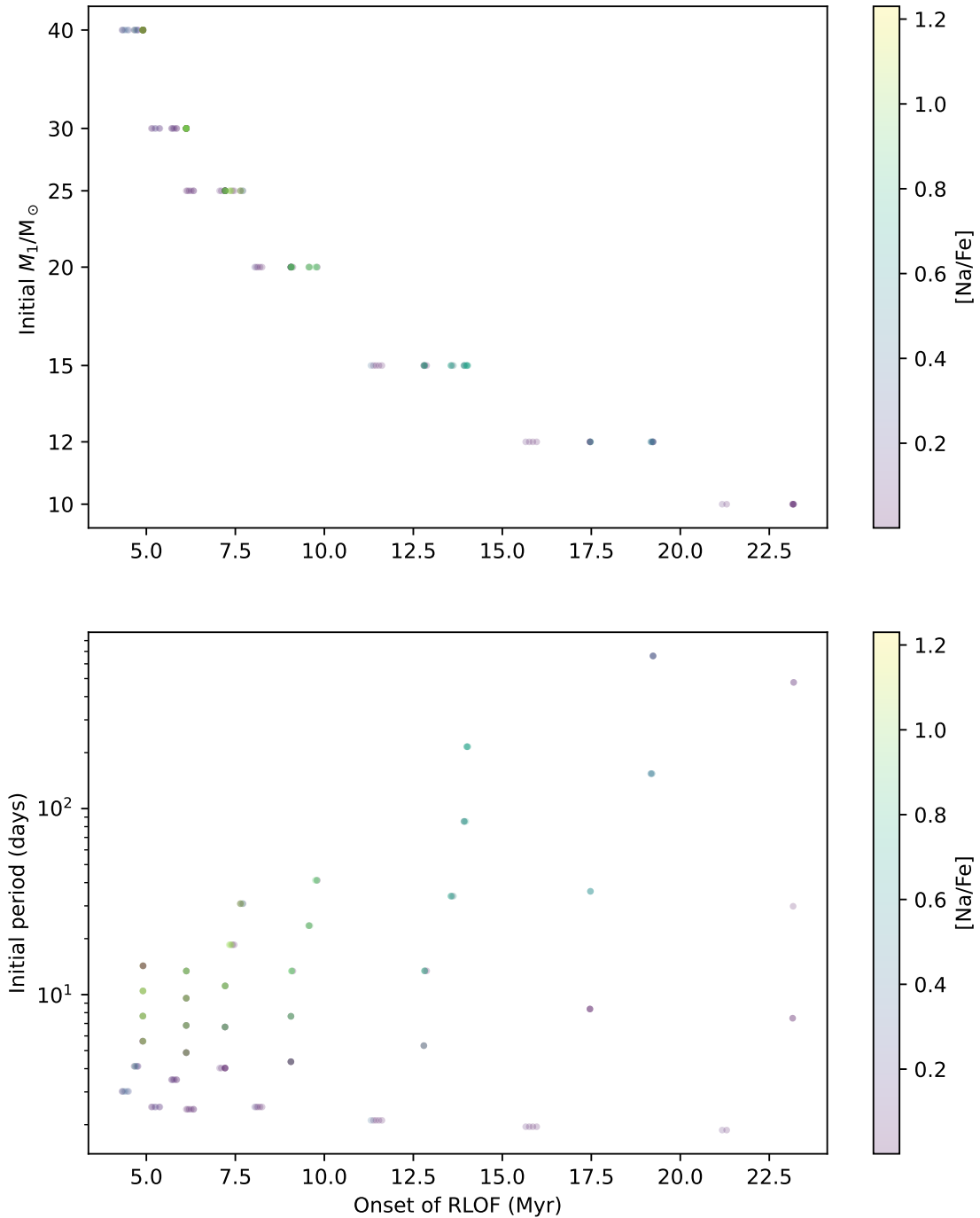


Figure 3.14: The onset of RLOF for the initial binary parameters: primary mass (top) and orbital period (bottom). Each point corresponds to one of the 190 binaries in our sample. Points are translucent to show the overlap. [Na/Fe] is shown through the colour map as a measurement of how enriching the binary ejecta is.

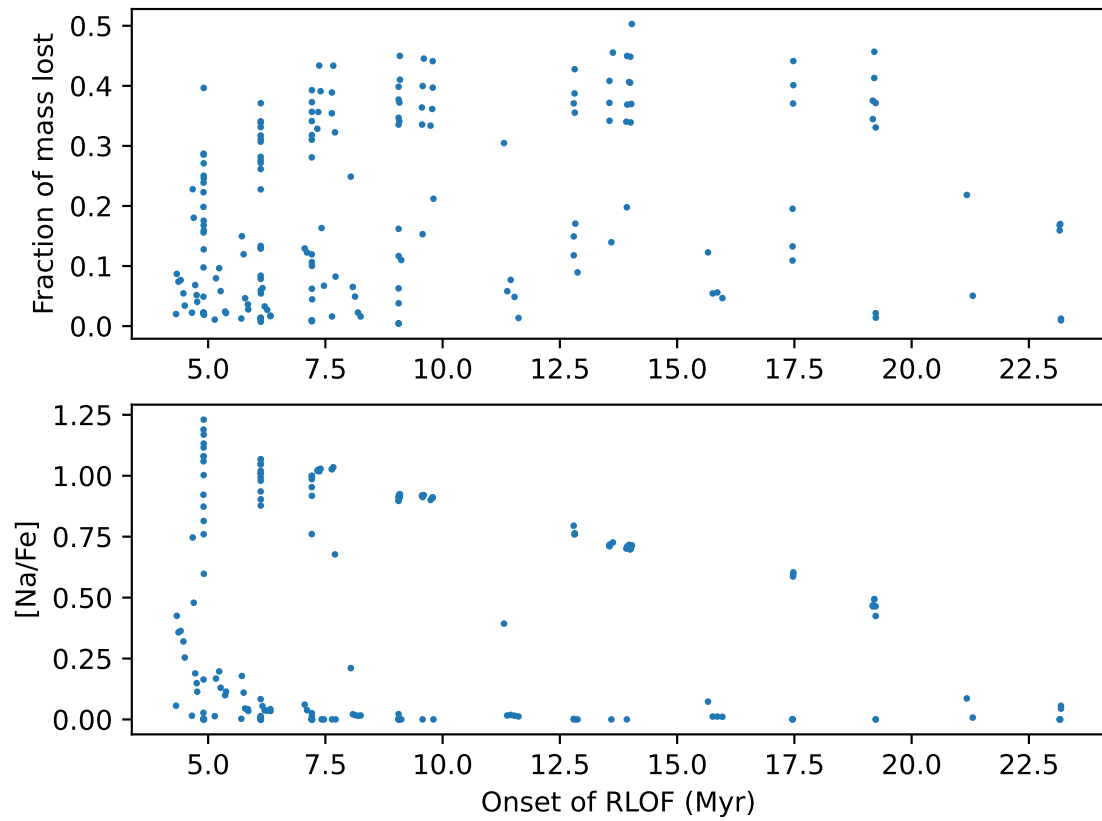


Figure 3.15: Scatter plots of the fraction of mass lost (top) and $[\text{Na}/\text{Fe}]$ (bottom) with respect to the onset of Roche lobe overflow (RLOF). This shows the timescales on which our simulated binaries eject material, relative to their formation (ZAMS).

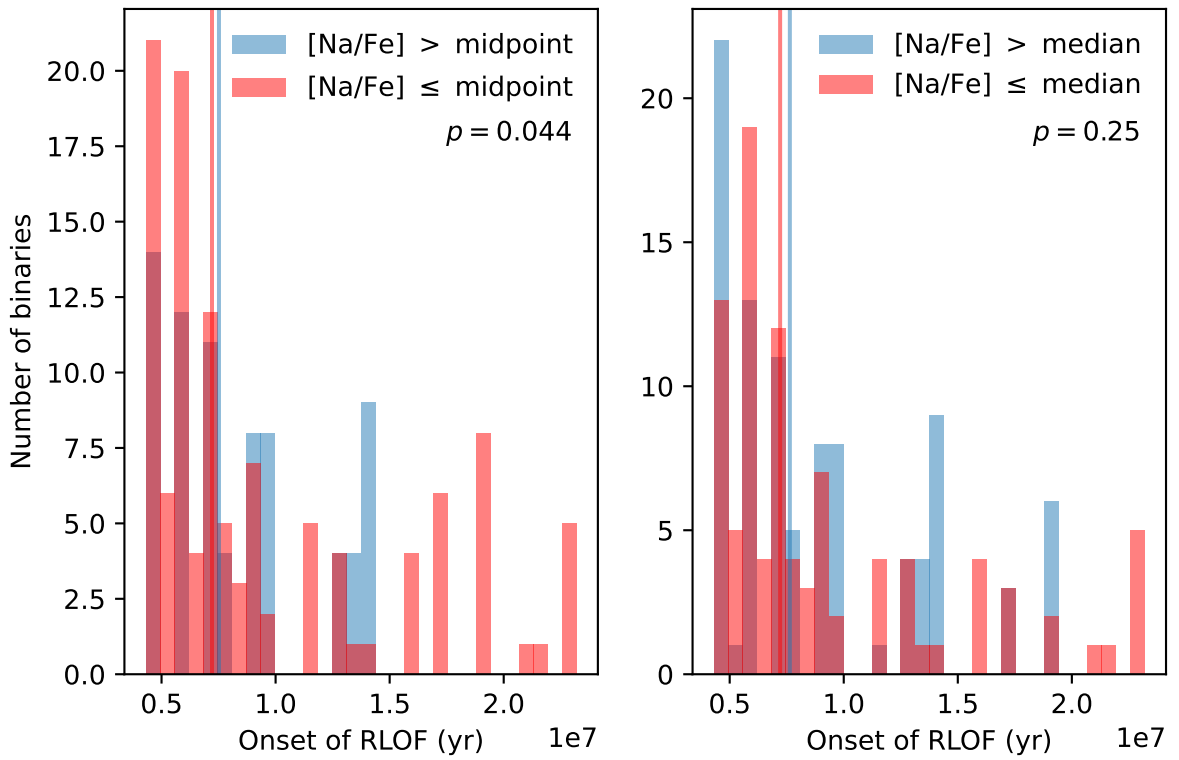


Figure 3.16: Distributions of the RLOF timescales for the binaries with cuts based on the $[\text{Na}/\text{Fe}]$ of their ejecta (midpoint or median), in the same manner as for figures in section 3.1.4. The medians of each sample are plotted as vertical lines.

occurs by setting the radius evolution of the primary. The lowest mass primaries eject on timescales $\gtrsim 23$ Myr, and the highest mass primaries we simulate can eject as shortly as ~ 4.3 Myr.

In figure 3.15 we show the timescales of the binary and their associated ejected fraction of system mass and the [Na/Fe] of their ejecta. There are no readily apparent trends of timescale with enrichment provided by the binary.

In figure 3.16 we compare the timescale distributions of the enriching and non-enriching binaries and find only weak differences between the samples ($p = 0.044$ for the midpoint cut, and $p = 0.25$ for the median cut). The medians of each sample are close to one another, suggesting that interacting binaries allow for the ejection of enriching and unenriched material on similar timescales. The enriching and non-enriching material of binaries fit into the dilution model of MP formation, as both are ejected on similar timescales and can mix prior to star formation. If stars form from relatively unmixed material, a scenario where the enriched and unenriched populations are coeval is also supported by their similar timescales or ejection.

3.1.6 Other abundance features of binary ejecta

We analyze the yields from our binaries for comparison to other constraints from observations of MPs.

An enhancement of He is often seen in enriched populations, although difficult to measure. We define ΔY as the difference between the ejected mass fraction of He and the initial mass fraction,

$$\Delta Y = Y_{\text{ejecta}} - Y_{\text{initial}} \quad (3.1.3)$$

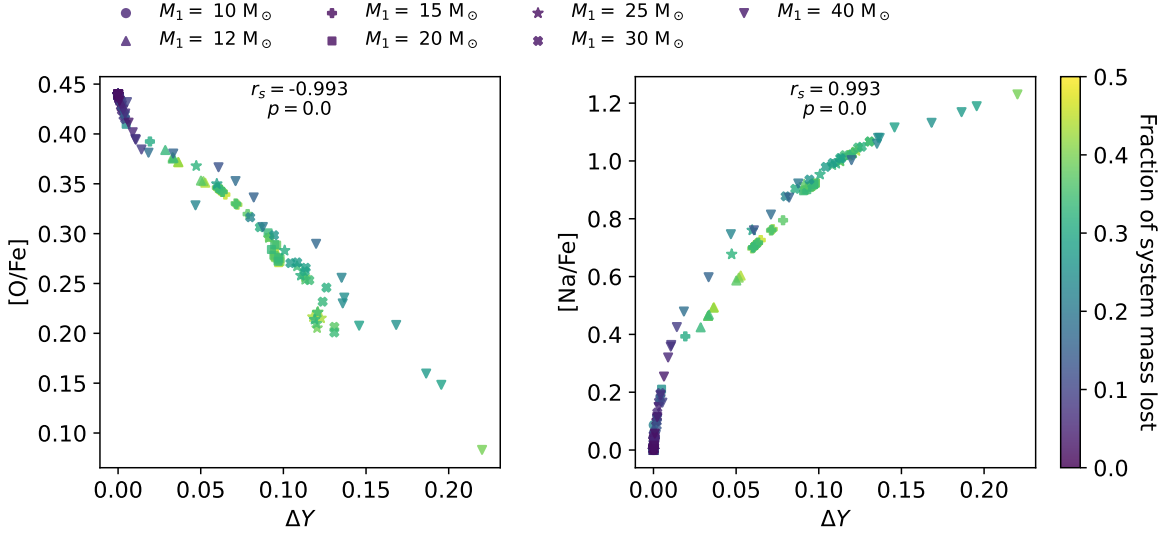


Figure 3.17: Relation between the He enhancement in mass fraction ΔY and the $[O/Fe]$ and $[Na/Fe]$ abundances. The colour map shows the fraction of the initial system mass lost by the end of the simulation. Spearman rank correlation coefficients and p -values are annotated on each panel.

In figure 3.17 we plot the He changes for the ejecta of each binary. O is strongly anti-correlated with He and Na shows a strong positive correlation with He. He enhancement is significantly associated with other enrichment signals in our binary ejecta, as expected from hot-H burning. An enhancement of Y by 0.1 corresponds to a ~ 1 dex enhancement of $[Na/Fe]$ and a ~ 0.2 dex depletion of $[O/Fe]$.

We consider if an iron spread is apparent in the ejecta and if it is associated with enrichment. In figure 3.18 we show the $[Fe/H]$ as a function of the helium spread ΔY . There is a strong monotonic correlation between the two. We also plot a least-squares linear fit performed with `numpy.polyfit` to show how $[Fe/H]$ varies with ΔY . An increase of Y by 0.2 corresponds to ~ 0.2 decrease in the H mass fraction, X . This is a change of ~ 0.135 dex in H which explains practically all the variation in $[Fe/H]$ over $\Delta Y = 0.2$. Our binary ejecta predict a small spread in $[Fe/H]$ due to the burning of H which decreases X . In the lower

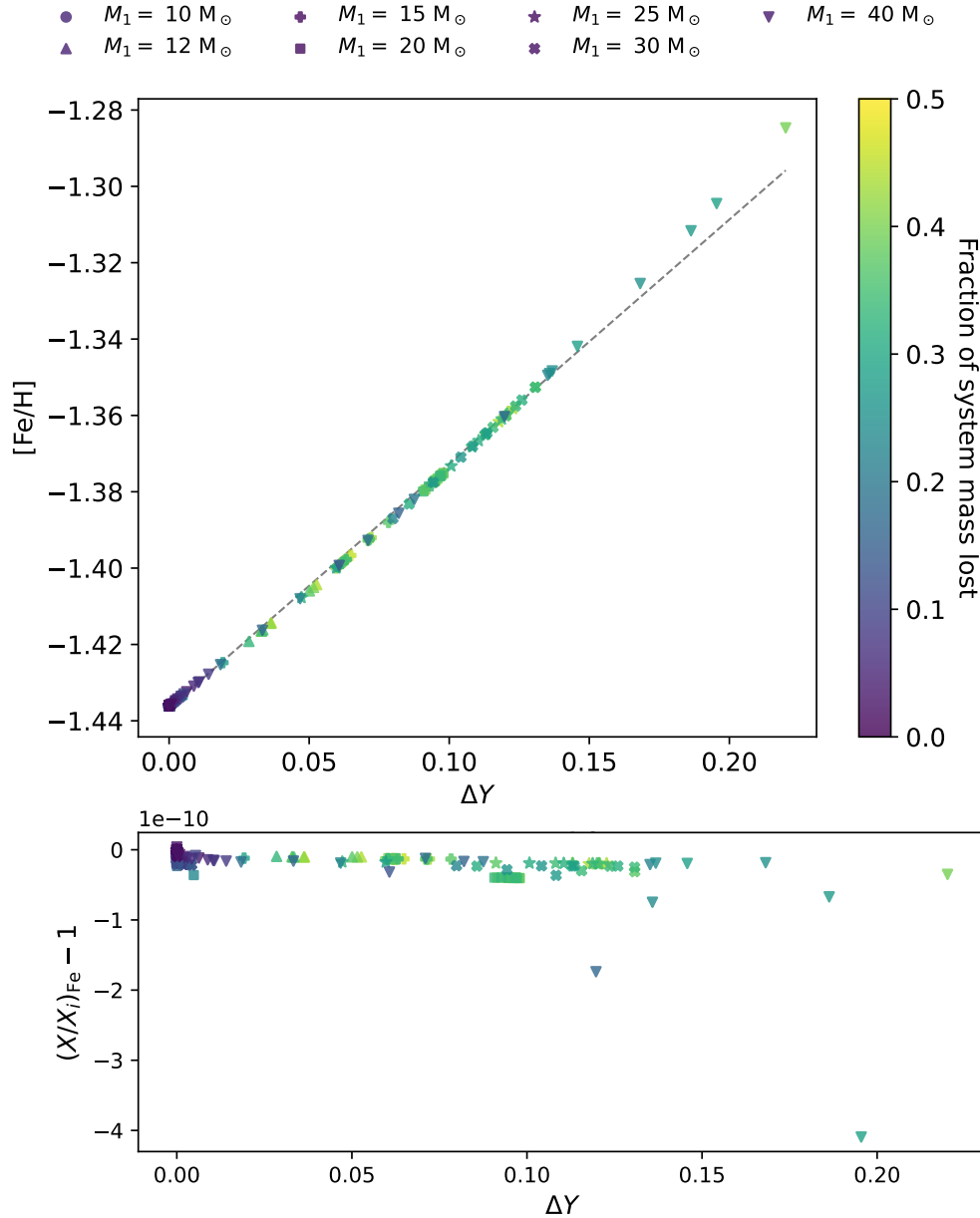


Figure 3.18: Scatter plot of the $[\text{Fe}/\text{H}]$ and ΔY of the ejected material from alpha-enhanced binary models. The Spearman rank coefficient and p – value are shown at the top of the plot. A linear least-squares fit is shown as a dashed line with the fitted relationship annotated on the panel. $[\text{Fe}/\text{H}]$ and ΔY are tightly correlated. The lower plot shows the enrichment difference of Fe in the ejecta instead of $[\text{Fe}/\text{H}]$, $(X/X_i)_{\text{Fe}} - 1$.

panel of the figure, we illustrate this by showing the enrichment X/X_i for Fe as a function of ΔY . Relative to the initial mass fraction, the Fe mass fraction only varies as much as $\sim 4 \times 10^{-10}$. As seen in table 3.3, the iron abundance does not vary at any significant level. We note that when abundances are measured relative to H, they will be impacted by variation in He.

For clusters with measured C, N, and O abundances the sum of C+N+O is constant (within uncertainties) for all measured stars in the cluster (Bastian & Lardo, 2018). We show the abundance of C+N+O as

$$A(\text{C} + \text{N} + \text{O}) = \log_{10} (N_{\text{C}} + N_{\text{N}} + N_{\text{O}}) - \log_{10} (N_{\text{H}}) + 12 \quad (3.1.4)$$

as a function of the helium enhancement $\Delta Y = Y_{\text{ejecta}} - Y_{\text{initial}}$ in figure 3.19. These are highly correlated ($r_s = 0.996$). We see that the maximum spread is ~ 0.15 dex. For reference, we perform a least-squares fit of a line using `numpy.polyfit` and show the resulting fit on the plot. Note that this slope is the same as seen in figure 3.18 and we find the same result that C+N+O is constant and H varies. As $r_s < 1$, there is a small amount of variation in C+N+O on top of this. In the bottom panel, we compare the absolute number of C+N+O atoms, rather than the $A(\text{C+N+O})$ which is relative to the H abundance. The variation is only about 0.02% at most, which is negligible. These results are consistent with the expectation that an enrichment source ejects hot-H burning products, but not more advanced burning products.

Some clusters exhibit Li abundance variations between their enriched and unenriched populations. We present the Li abundances in our binary yields to see if there is a Li variation associated with enrichment. In figure 3.20 we compare the $[\text{Na/Fe}]$ to the $[\text{Li/Fe}]$ seeing a weak correlation, indicating that highly enriched material from binary ejecta tends to be more Li-poor. All ejecta has $[\text{Li/Fe}] < 0$, indicating all our binaries deplete Li. Performing

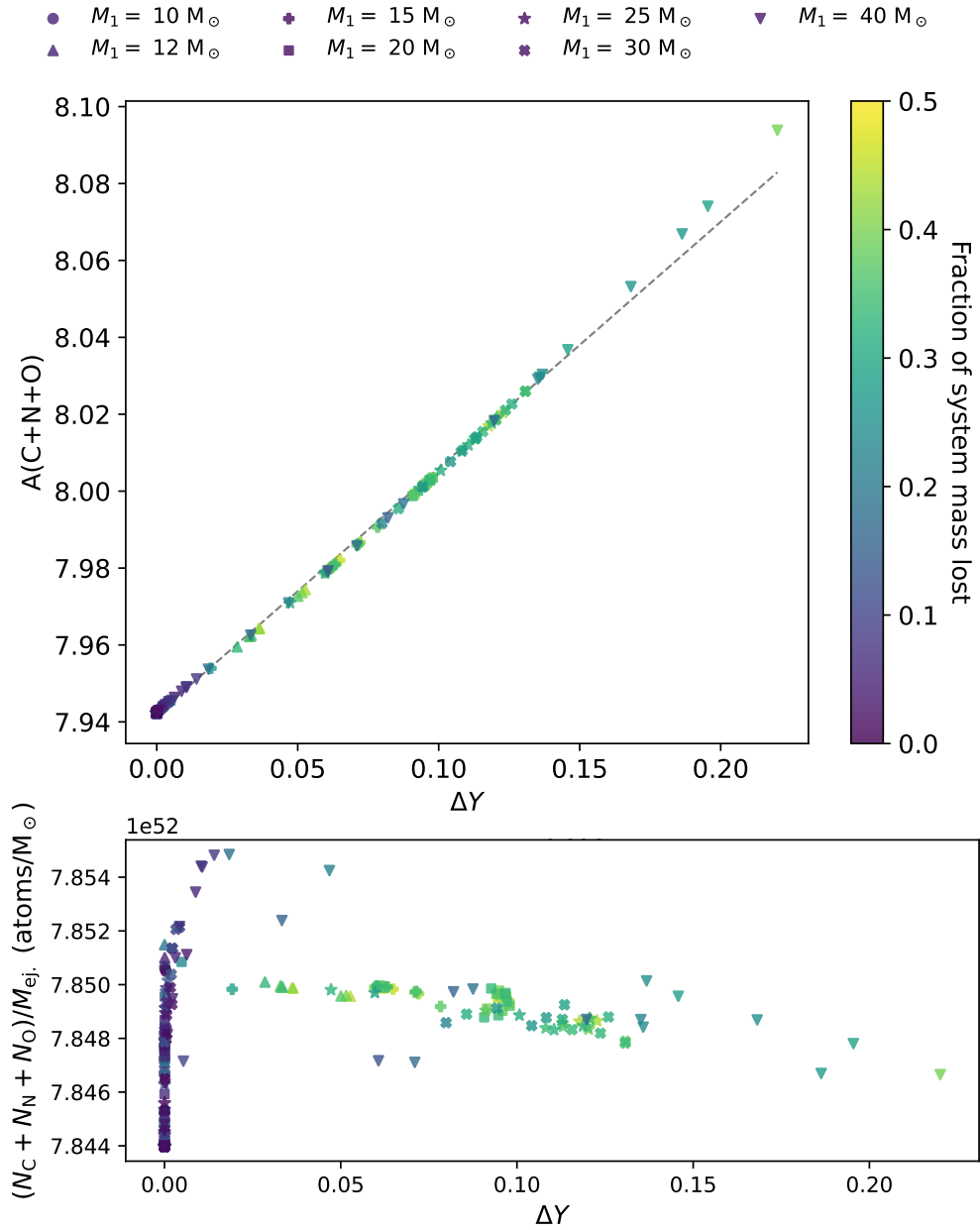


Figure 3.19: Relationship between $A(\text{C+N+O})$ and ΔY similar to figure 3.18 in the upper panel. In the bottom panel, the number of C, N, and O atoms per ejected solar mass. The variation in the number of C+N+O atoms is at a fractional level of $\sim 2 \times 10^{-4}$ compared to the total number of atoms.

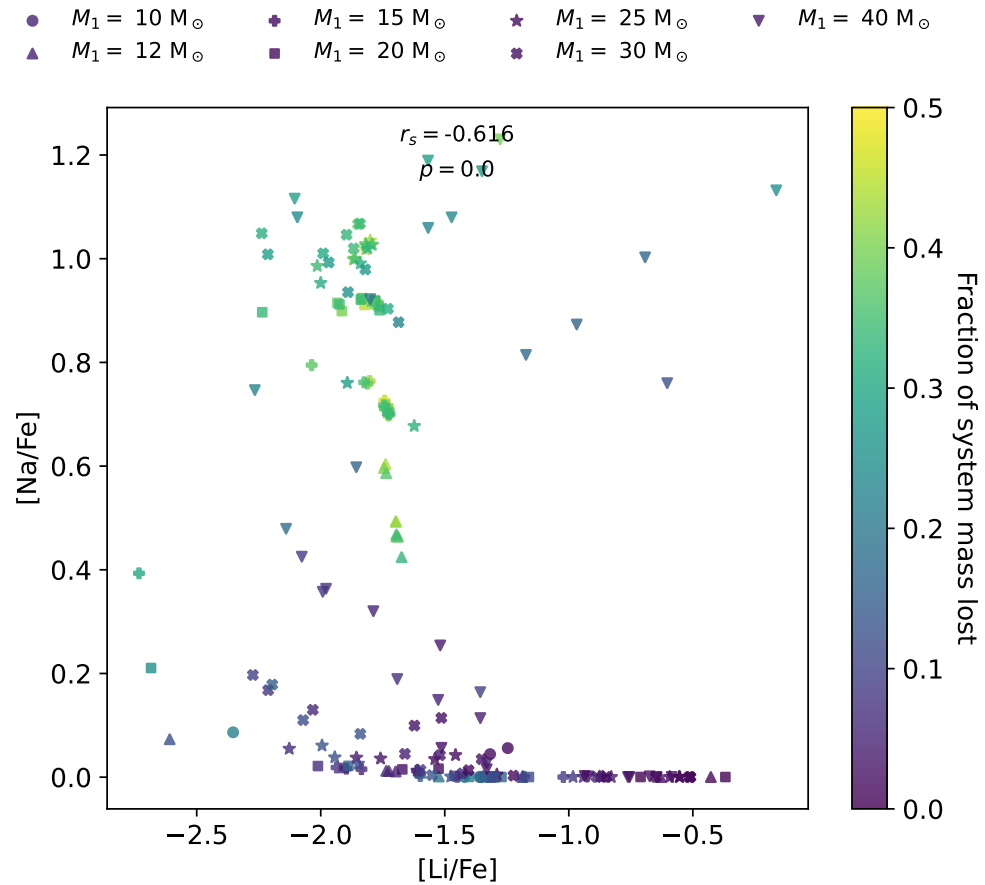


Figure 3.20: Scatter plot of the [Na/Fe] and [Li/Fe] of the ejecta of alpha-enhanced binary models. The Spearman rank correlation coefficient and p -value are annotated at the top of the plot. A weak anti-correlation is seen.

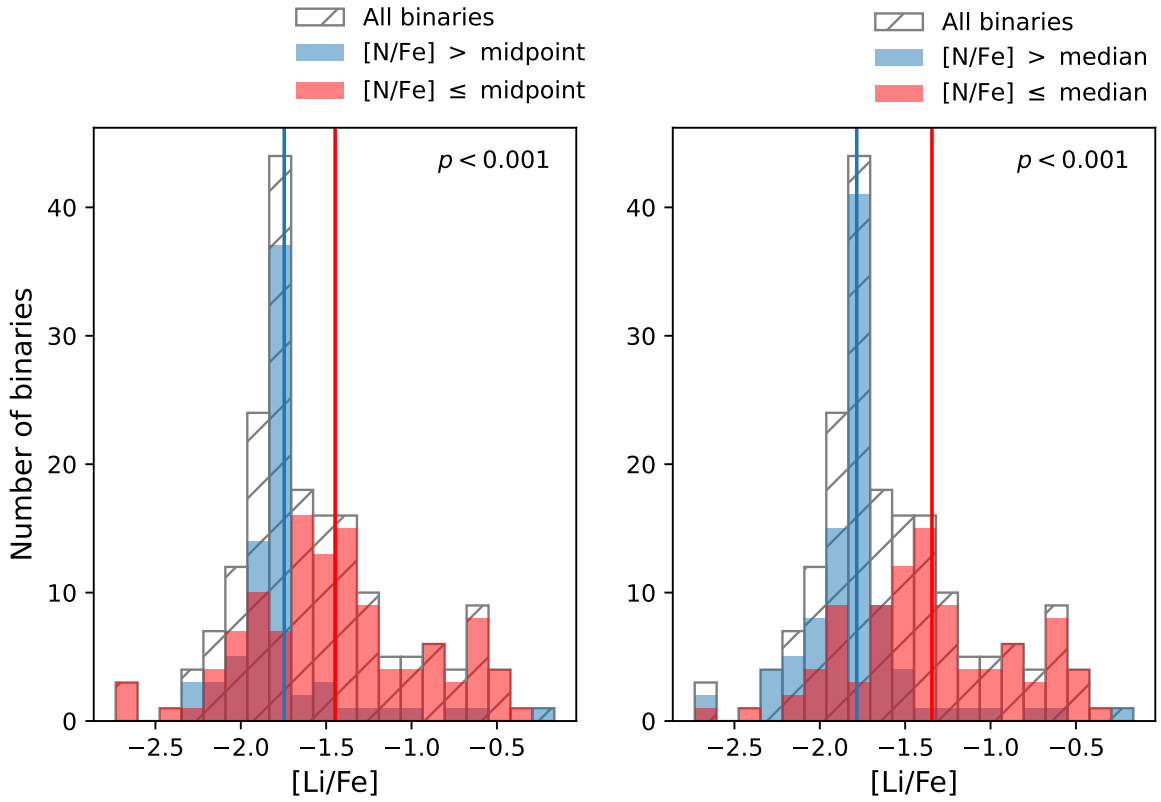


Figure 3.21: Histograms of the $[Li/Fe]$ of modelled alpha-enhanced binary ejecta. The binaries have been split based on their $[Na/Fe]$ as a proxy for how enriching the binary is. The Anderson-Darling p -value is annotated on the graph. Medians of the distributions are shown as vertical lines.

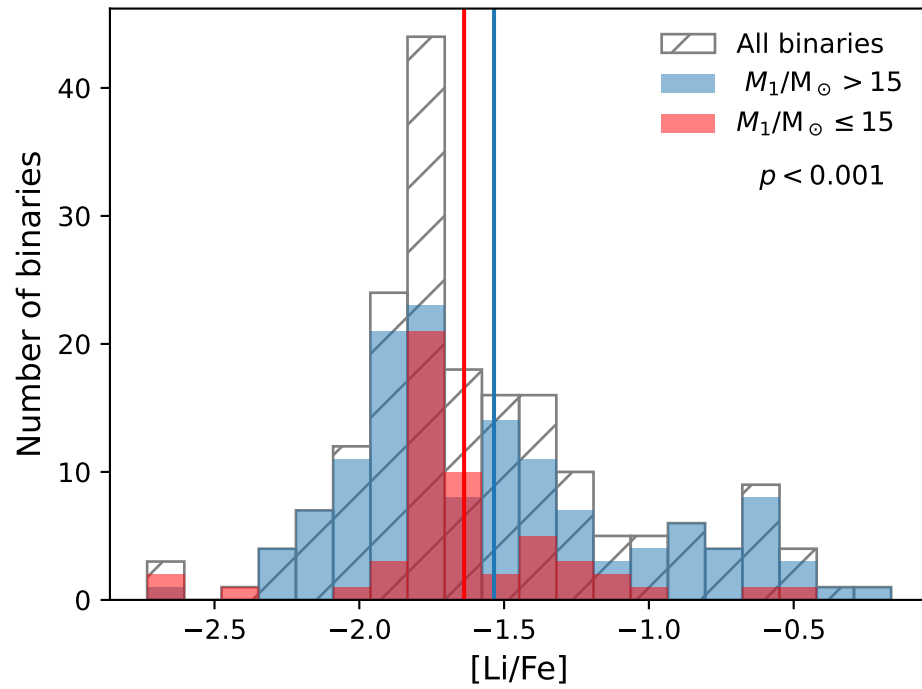


Figure 3.22: Histogram of the [Li/Fe] of modelled alpha-enhanced binary ejecta, similar to figure 3.21. The binaries have been split based on their initial primary mass.

the median and midpoint splits in $[\text{Na}/\text{Fe}]$ and comparing their Li distributions in figure 3.21, we see that the distributions of $[\text{Li}/\text{Fe}]$ are statistically distinct. The peak and median $[\text{Li}/\text{Fe}]$ of the binaries we simulate are lower for enriching binaries than for non-enriching binaries. The non-enriching binaries are less peaked in $[\text{Li}/\text{Fe}]$. Both non-enriching and enriching binaries eject a similar maximum and minimum $[\text{Li}/\text{Fe}]$.

Massive stars easily destroy lithium in contrast to AGB stars, which are expected to be able to produce some Li. We compare the $[\text{Li}/\text{Fe}]$ distributions of binaries with $M_1 > 15 M_\odot$ and with $M_1 \leq 15 M_\odot$ in figure 3.22. The distributions are distinct, with more massive stars showing more spread in their typical $[\text{Li}/\text{Fe}]$ ejected. The median $[\text{Li}/\text{Fe}]$ is higher for more massive stars, converse to expectations that more massive stars would show stronger Li depletion. This indicates Li depletion is sensitive to other factors such as the evolutionary phase of the binary during mass ejection. In combination with the result that $[\text{Na}/\text{Fe}]$ and $[\text{Li}/\text{Fe}]$ show a weak correlation, this indicates that binary ejecta can complicate $[\text{Li}/\text{Fe}]$ in an enriched population.

We show the relationship between Al abundance and N and Mg in figure 3.23. These exhibit the Al-N correlation and Al-Mg correlation. However, it is clear that the $[\text{Mg}/\text{Fe}]$ variation is extremely small (maximum of ~ 0.02 dex) consistent with the results that no change was observed in Mg abundance in table 3.1. The Al-N scatter plot exhibits the same features as Na-N and C-N where the shape of the relationship varies with primary mass. We note that we enhanced the initial composition to have $[\text{Mg}^{24}/\text{Fe}] = 0.411$ which is above the $[\text{Mg}/\text{Fe}]$ measured in the ejecta of any of the binaries. This is because there are significant fractions of Mg^{25} and Mg^{26} at solar abundances ($\sim 10\%$ each).

The isotopic ratios of Mg may indicate the source of enrichment for MPs, with AGB stars expected to produce different ratios than massive stars, for example (Denissenkov &

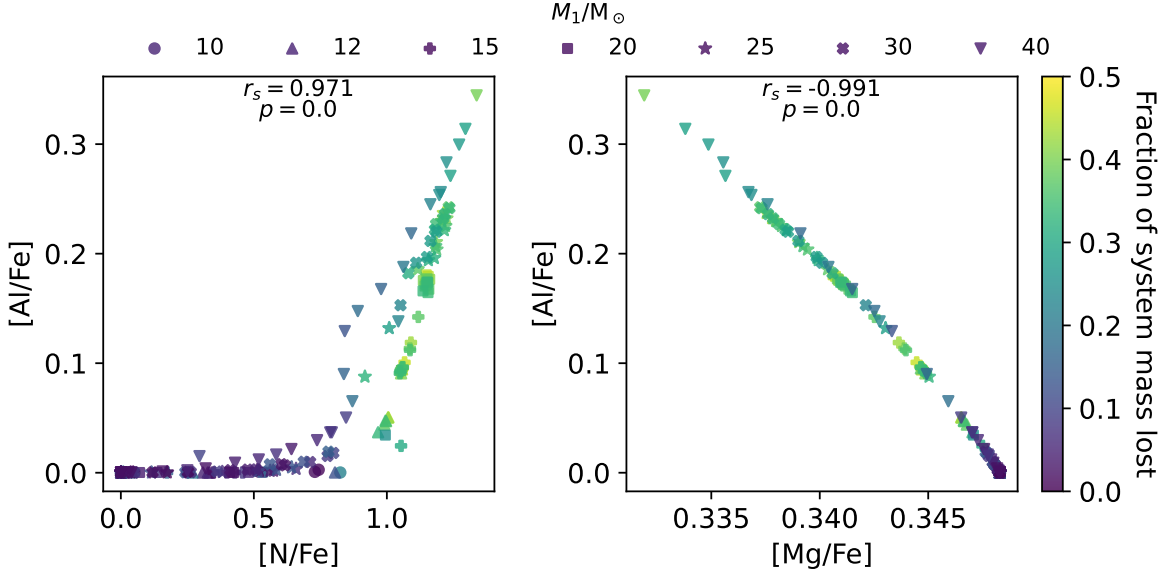


Figure 3.23: Al-N and Al-Mg relations for the ejecta of our alpha-enhanced binaries. Spearman rank correlation coefficient and p -value of the data corresponding to an uncorrelated set are shown.

Herwig, 2003; Thygesen et al., 2016). We calculate the relative changes in the main Mg isotopes: Mg^{24} , Mg^{25} and Mg^{26} and list these in table 3.2. We also include Mg^{22} and Mg^{23} in our network but do not include them in our initial composition and find no significant production of either element. In general, Mg^{25} shows depletion and the other isotopes have no median change. Mg^{26} is enhanced in the ejecta of some binaries and is significantly depleted in others.

Isotope	Min. X/X_i	Max. X/X_i	Median X/X_i	General change
Mg^{24}	1.0	1.0043	1.0	no change
Mg^{25}	0.4887	1.0	0.9585	depleted
Mg^{26}	0.6723	1.0538	1.0	no change

Table 3.2: Enrichment of Mg isotopes in binary ejecta from alpha-enhanced binary models. The minimum, maximum, and median relative changes are listed. Based on the median value we describe if the isotope is generally depleted, enhanced, or shows no change.

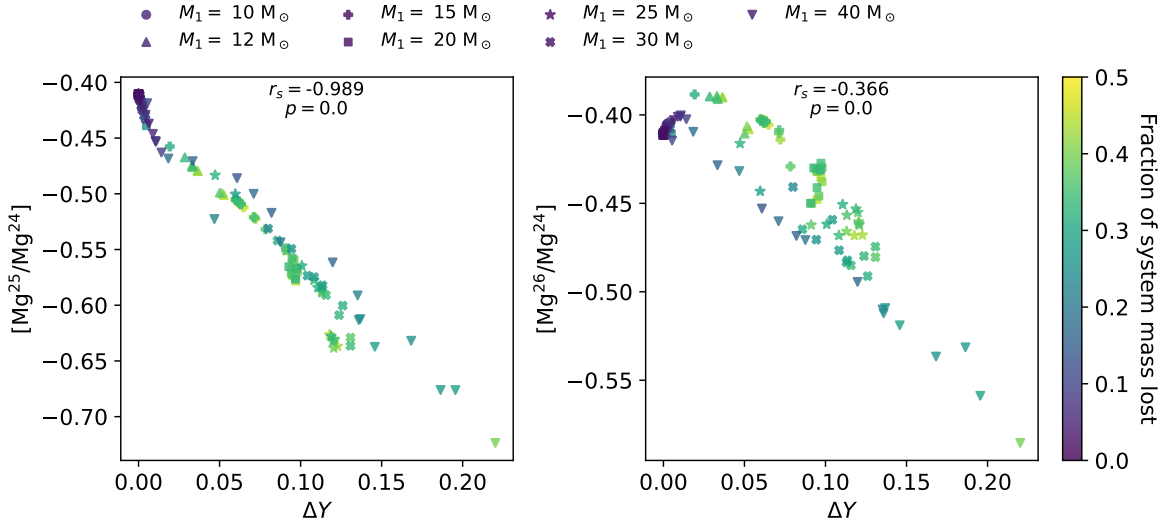


Figure 3.24: Isotopic ratios of Mg as a function of helium mass fraction increase seen in alpha-enhanced binary ejecta. Spearman rank coefficients and p -values are annotated on the top.

3.2 Expected yields from a binary population

To determine the expectation values from a population of binaries, we consider the observed frequencies of the binaries. On a grid covering $1.87 < P < 661.65$ days, $10 < M_1 < 40 M_\odot$, and $0.15 < q < 0.9$ in steps of $\Delta(\log P) = 0.01$ [days], $\Delta M_1 = 0.1 M_\odot$, and $\Delta q = 0.01$, we interpolate the results from our grid of binary simulations. We interpolate our results linearly using `scipy.interpolate.griddata`. We do not extrapolate any results beyond the boundaries of our simulations.

To consider a realistic binary population, we need to weigh the results by their probabilities. We base our methods on work by Cournoyer-Cloutier et al. (2021), where they simulated star cluster formation and evolution including binaries. We use the same distributions as they do for their binary generation algorithm. For the primary mass distributions,

we reference a Kroupa initial-mass function (IMF) (Kroupa, 2001):

$$f(M_1) \propto \begin{cases} M_1^{-1.3} & 0.08 \leq M_1 \leq 0.5 \\ M_1^{-2.3} & 0.5 < M_1 \leq 150 \\ 0 & \text{otherwise} \end{cases} \quad (3.2.1)$$

where a constant factor is set to normalize the probability density function $f(M_1)$ for our chosen minimum and maximum mass $0.08 \leq M_1 \leq 150 M_\odot$. Our lowest primary mass is $10 M_\odot$ and our smallest secondary is $3.75 M_\odot$. These limits affect the absolute probabilities of our binaries occurring, but not their relative probabilities, since the limits determine the normalization factor.

We use the binary parameter distribution functions for period and mass ratio from Moe & Di Stefano (2017). In particular, we reference the parameters and statistics provided in their Table 13. We do not account for the uncertainties in these parameters in our analysis. All of our periods sampled fall into the “close” description of Moe & Di Stefano (2017) as $\log(P/\text{days}) < 3.7$. We also use the multiple fraction $\mathcal{F}_{n>0}$ from Moe & Di Stefano (2017) to scale the probabilities. The multiple fraction refers to the number of primaries that are not singles, i.e. it is

$$\mathcal{F}_{n>0} = \frac{\text{number of singles} + \text{number of binaries} + \text{number of triples} + \dots}{\text{number of binaries} + \text{number of triples} + \dots} \quad (3.2.2)$$

For the binaries we simulate, $\mathcal{F} = 0.84$, $M_1 < 16 M_\odot$ and $\mathcal{F} = 0.94$, $M_1 \geq 16 M_\odot$, dropping the $n > 0$ subscript. Although the multiplicity fraction includes higher order multiples, we treat these as occurrence rates for binaries as many multiples are hierarchical with an inner binary and outer tertiary/quarternary/etc. (?). We assume that we are modelling the inner

binary of such systems.

Moe & Di Stefano (2017) provide the companion frequency per decade of period in ranges of $\log_{10} P$ in $(0.5 - 1.5)$, $(2.5 - 3.5)$. We linearly interpolate between the period ranges (e.g. for $\log_{10}(P)$ in $[1.5 - 2.5]$). We also extend the close period range $\log P$ in $(0.5 - 1.5)$ down to $\log_{10}(P) \geq 0.2$ which is the lower limit of the period, with the same companion frequency per dex. Their distributions of the companion frequency at small $\log P \leq 1$ are flat, so this is a reasonable approximation. In each bin of log period, we consider the probability distribution to be uniform in $\log P$.

The mass ratio distribution power law $f(q) \propto q^\gamma$ has γ listed for $\log_{10} P = 1, 3, 5, 7$ [days]. We use the power-law slopes listed for $\log P = 1$ over the range $[0.2, 2)$ and use the slopes at $\log P = 3$ for the range $[2, 4)$.

We do not consider the eccentricity distribution function of the binaries as we only simulate initially circular binaries.

The probability distribution function for binaries of M_1, q, P is the product of the individual distribution functions, scaled by the probability of a primary being in a multiple:

$$f(M_1, q, \log P) = f(M_1)f(q)f(\log P)\mathcal{F}. \quad (3.2.3)$$

To determine expectation values on our grid with spacing of $\Delta(M_1), \Delta(q), \Delta(\log P)$, we perform the sum over the entire grid

$$\text{expected } X = \sum_i X_i w_i \cdot f(M_1, q, \log P) \Delta(M_1) \Delta(q) \Delta(\log P) \quad (3.2.4)$$

where w_i are additional weights for the given interpolated binary on grid cell i and X is the quantity we measure. X_i is the linearly interpolated quantity X for the cell i . For most of

our values, we calculate the unweighted sum, $w_i = 1$. For mass-weighted values, we use the mass ejected M_{ej} , such that

$$w_i = \frac{M_{\text{ej},i}}{\sum_j M_{\text{ej},j} \cdot f(M_1, q, \log P) \Delta(M_1) \Delta(q) \Delta(\log P)} \quad (\text{mass-weighting}) \quad (3.2.5)$$

Additionally, we calculate weighted statistics including standard deviation, medians, and other quantiles using `statsmodels.stats.DescrStatsW` (Perktold et al., 2023).

For reference, a visualization of our interpolated parameter space and the probabilities associated with each cell is in appendix B.

3.2.1 Overall expected values

First, we consider the values expected overall for enrichment by binaries, in terms of the mass and the timescales expected.

Of the cubic grid $1.87 < P < 661.65$ days, $10 < M_1 < 40 M_\odot$, and $0.15 < q < 0.9$, our binaries span about 60% of the total probability of binaries with these properties. Our binaries and their interpolations are $\sim 0.071\%$ of all systems (singles + binaries). Their primaries constitute $\sim 2.5\%$ of the total mass in primaries. We note the total mass in primaries includes singles and the most massive star in a binary.

A “typical” binary within our range ejects $\sim 22\%$ of its initial system mass, or $\sim 6.7 M_\odot$ on a timescale of 12 Myr. The ejected-mass-weighted expected timescale is ~ 11 Myr. This corresponds to about $0.0047 M_\odot$ per primary in an entire stellar population or $\sim 0.81\%$ of the total mass in primaries. Binaries similar to our systems are relatively rare and as such only contribute a small fraction of the stellar population mass.

In comparison, if each of our interpolated binaries were two singles instead, they would

eject about $1.1 M_{\odot}$ per pair, on an ejected-mass-weighted timescale of 14 Myr. This is about 16% of what would be ejected as a binary in our simulated range. With just the primary yields considered, the ejection would only be $\sim 12\%$ of the binary yields.

Binaries that undergo non-conservative mass transfer eject significantly more mass than they would as singles. Treating massive stars as single stars neglects considerable mass loss, and by extension enrichment, on top of neglecting the fact that the majority of massive stars reside in multiples.

For the 6 low-mass binaries that did not undergo RLOF since they were beyond the period limit, they only eject $\sim 1\%$ of their initial system mass or $\sim 2\%$ of their initial primary mass by termination. Single models of the same masses as the primary (10 and $12 M_{\odot}$) eject about 3% of their initial mass.

To illustrate the dependence on the “typical binary ejecta” properties on our grid, we show the probability per mass bin in figure 3.25. The low-mass end is missing a factor of ~ 8 of the total probability space due to the restriction of $q = 0.75, 0.9$ in our simulations. At the high-mass end, the restriction of the period to $\lesssim 15$ days from ~ 660 days at the low-mass end reduces the probability covered by about a factor of 4. We also note that since none of the $M_1 = 30, 40 M_{\odot}$ primaries reach core-C depletion as lower-mass primaries do, there is likely an underestimate of mass ejection disproportionately affecting high-mass yields. The underestimation of mass ejection in runs terminated due to contact or unstable mass loss rates is considered in section 3.4.

3.2.2 Expected enrichment and spreads

From our interpolated binary yields and the probability associated with them, we calculate the expected yields in each element and the associated spread. In figure 3.26 we show

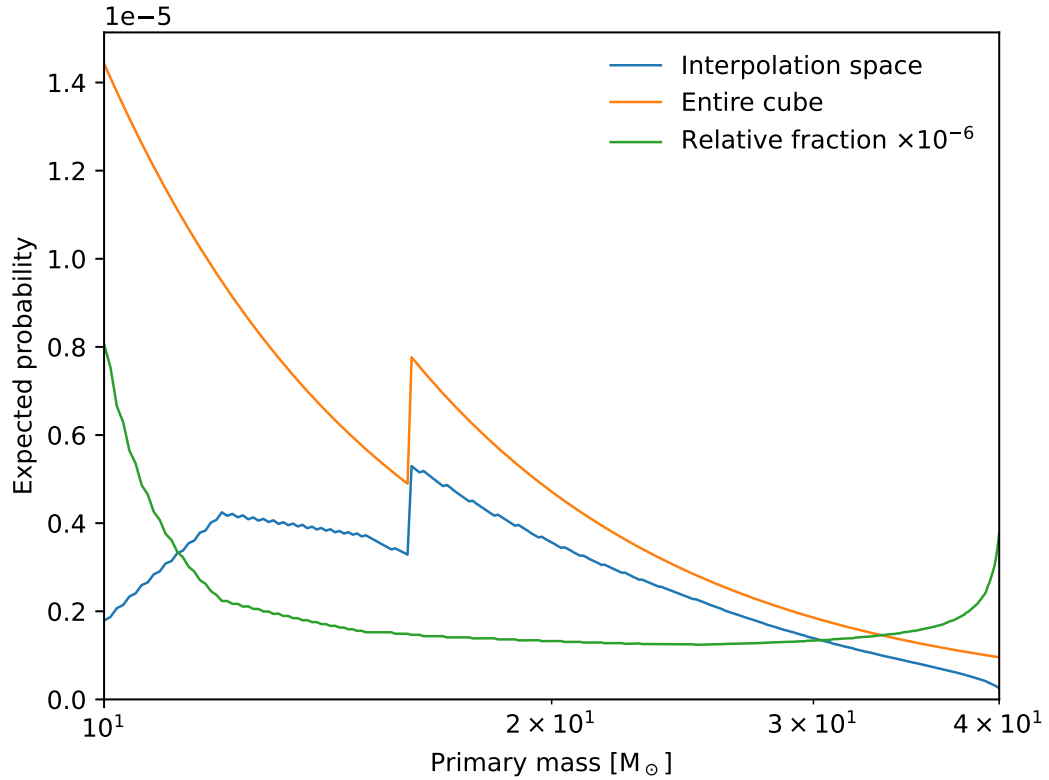


Figure 3.25: Probability of a binary occurring per mass bin of width $0.1 M_{\odot}$. For the entire cube, the probabilities are summed over $1.87 < P < 661.65$ days and $0.15 < q < 0.9$. For the interpolation space, we only sum over the ranges within the volume covered between our simulated binaries: restricting q at the low mass end and P at the high mass end in particular. The green line shows the relative probability in the total cube compared to only the interpolation space, scaled by 10^{-6} to fit on the same axis. A discontinuity in the probabilities occurs at $M_1 = 16 M_{\odot}$ as this is the boundary between B-stars and O-stars. O-star primaries are more likely than B-stars to be part of a binary or multiple.

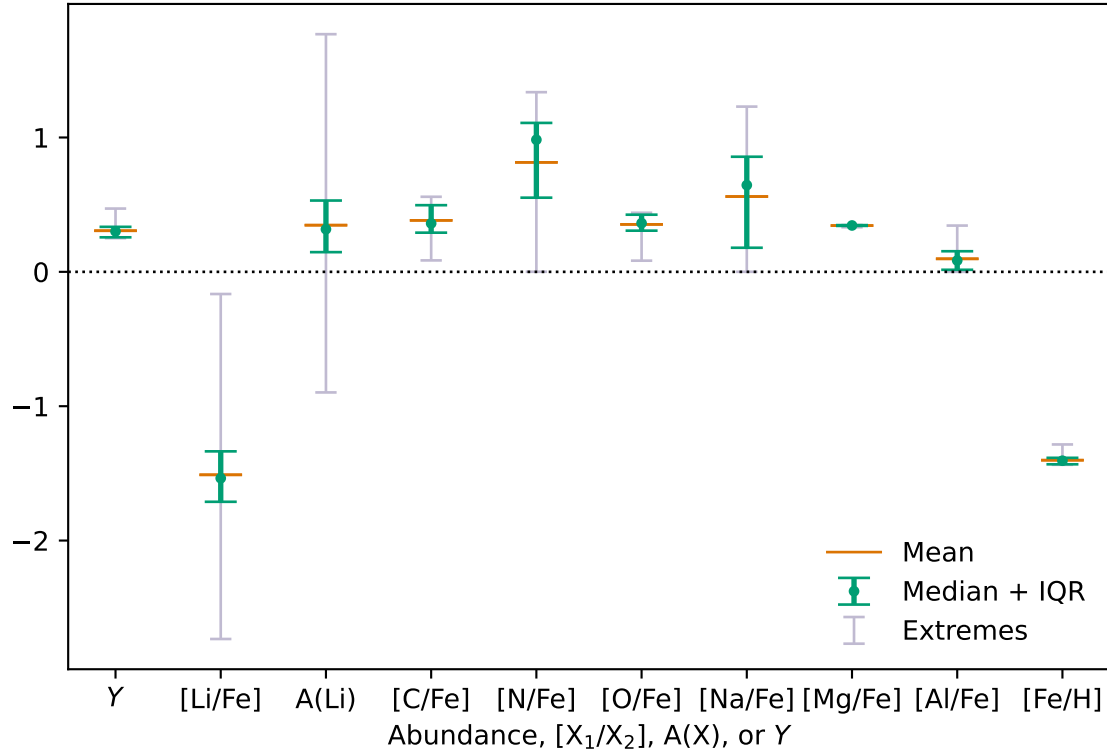


Figure 3.26: The abundances of binary ejecta, as a “typical” population of binaries within our interpolation limits. Values were calculated by interpolating yields within our simulated parameter space and weighting their yields by their expected occurrence to calculate their weighted statistics. The green point corresponds to the median, with the bold, green error bars corresponding to the interquartile range (IQR, 25-75th percentile). The orange bar indicates the mean. Light grey bars show the extremes of the range. These features overlap for [Mg/Fe] for the line widths and marker size plotted. For elements in A(X) or $[X_1/X_2]$ notation, the values are in dex. For Y, this is just the direct mass ratio of helium.

Abundance	Minimum	25th percentile	Median	75th percentile	Maximum	Mean
Y	0.251	0.257	0.301	0.335	0.471	0.306
$[\text{Li}/\text{Fe}]$	-2.733	-1.712	-1.536	-1.336	-0.165	-1.511
$A(\text{Li})$	-0.898	0.147	0.317	0.531	1.769	0.348
$[\text{C}/\text{Fe}]$	0.085	0.292	0.36	0.496	0.559	0.383
$[\text{N}/\text{Fe}]$	0.001	0.552	0.983	1.109	1.337	0.815
$[\text{O}/\text{Fe}]$	0.083	0.306	0.362	0.425	0.44	0.353
$[\text{Na}/\text{Fe}]$	0.0	0.179	0.646	0.857	1.23	0.561
$[\text{Mg}/\text{Fe}]$	0.332	0.342	0.345	0.348	0.348	0.344
$[\text{Al}/\text{Fe}]$	0.0	0.015	0.084	0.153	0.344	0.097
$[\text{Fe}/\text{H}]$	-1.436	-1.433	-1.406	-1.384	-1.285	-1.402

Table 3.3: Abundances and ranges of the weighted sum of the ejecta from the binaries we simulated. This corresponds to values plotted in figure 3.26.

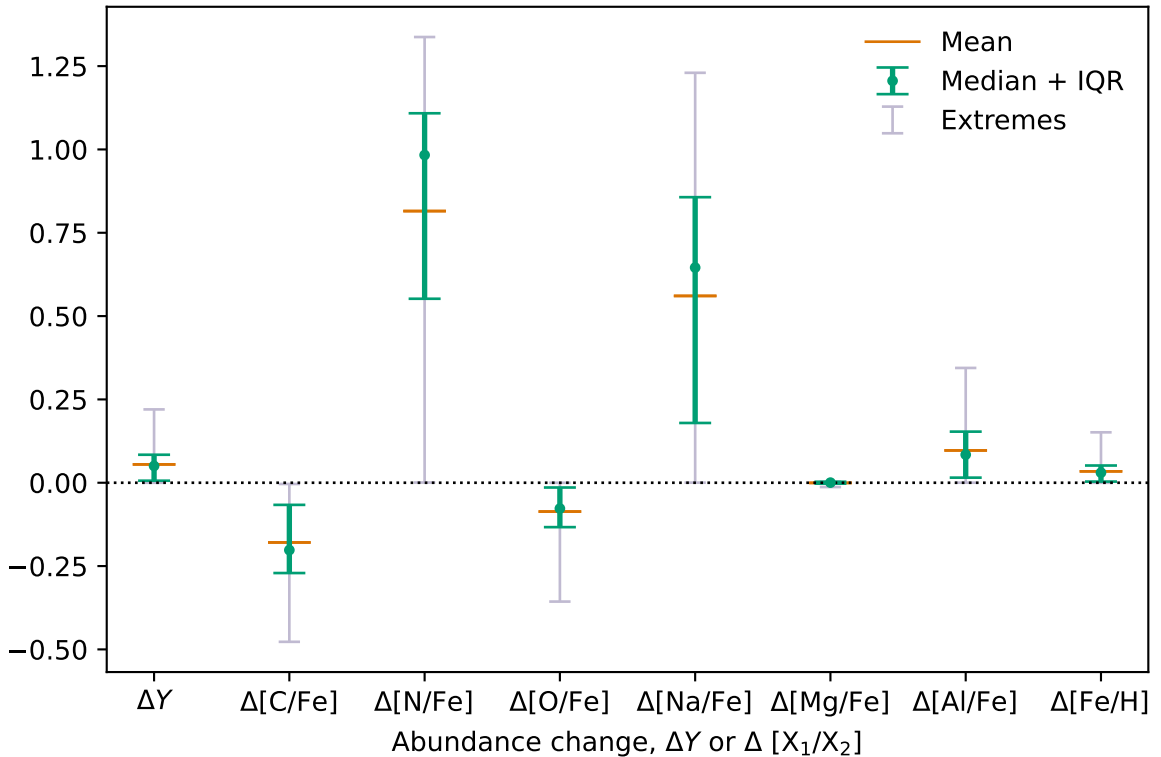


Figure 3.27: The abundance of elements from interpolated, and probability-weighted yields of our simulated binaries, relative to the initial alpha-enhanced composition. This figure follows the same general format as figure 3.26.

Abundance	Min.	25th percentile	Median	75th percentile	Max.	Mean	IQR	σ
ΔY	0.0	0.006	0.05	0.084	0.22	0.055	0.078	0.049
$\Delta[\text{C}/\text{Fe}]$	-0.477	-0.271	-0.202	-0.066	-0.004	-0.179	0.205	0.116
$\Delta[\text{N}/\text{Fe}]$	0.001	0.552	0.983	1.109	1.337	0.815	0.556	0.392
$\Delta[\text{O}/\text{Fe}]$	-0.357	-0.133	-0.077	-0.014	-0.0	-0.086	0.119	0.076
$\Delta[\text{Na}/\text{Fe}]$	0.0	0.179	0.646	0.857	1.23	0.561	0.677	0.37
$\Delta[\text{Mg}/\text{Fe}]$	-0.013	-0.003	0.0	0.003	0.004	-0.0	0.006	0.004
$\Delta[\text{Al}/\text{Fe}]$	0.0	0.015	0.084	0.153	0.344	0.097	0.138	0.084
$\Delta[\text{Fe}/\text{H}]$	-0.0	0.003	0.03	0.052	0.151	0.034	0.048	0.032
$[\text{O}/\text{Na}]$	-1.147	-0.55	-0.283	0.245	0.439	-0.207	0.795	0.442

Table 3.4: Abundances of the weighted sum of the ejecta from the binaries we simulated relative to the initial composition, as Δ . The first 8 abundances (above the dividing line) are shown in figure 3.27. We also include the $[\text{O}/\text{Na}]$ measures to show the spread of the Na-O relation.

abundances in terms of the mean, median, IQR, and extremes. We report the abundances of He, Li, C, N, O, Na, Mg, Al, and Fe. The values that we plot in figure 3.26 are shown in table 3.3. For Li, we show both $[\text{Li}/\text{Fe}]$ and $A(\text{Li})$ as $[\text{Li}/\text{Fe}]$ illustrates the relative depletion to the initial abundance of Li and $A(\text{Li})$ can be compared to measurements of Li in literature.

We present the change in He, C, N, O, Na, Mg, Al, and Fe in figure 3.27 and table 3.4. In table 3.3 we also report the IQR and standard deviation, σ , associated with the yields. As a measure of the Na-O correlation, we also calculate the ranges for $[\text{O}/\text{Na}]$ in the ejecta and list this in table 3.4.

Helium enhancement typically shows a spread of 0.034 in mass fraction with a median mass fraction of 0.05. This is consistent with the maximum spreads of He typically observed in clusters, but is larger than the expected difference between average unenriched and average enriched population abundances (Milone et al., 2018; Bastian et al., 2015). The iron spread is ~ 0.021 dex.

The typical variation of [Mg/Fe] is small (~ 0.006 dex) and is generally below observational measurement limits (e.g. Schiappacasse-Ulloa & Lucatello, 2023). The largest spreads are seen in Na, N, and C with IQRs of 0.677, 0.556, and 0.205 dex respectively. IQRs for O and Al are more modest at 0.119 and 0.138 dex.

The [O/Na] IQR in the ejecta of our binaries is 0.795 dex. This is larger than the typical values of Carretta (2019) where the median IQR is $\sim 0.6 \pm 0.1$ dex, depending on the location of the clusters (disk/bulge, inner/outer halo).

In section 3.1, we showed ejecta enrichment varies with primary mass, in terms of both strength and the shape of the correlations (ex. Na-N). Higher mass primaries tended to provide more extreme enrichment. In general, high-mass primaries are less common than lower-mass primaries due to the shape of the IMF (e.g. Kroupa, 2001). This would suggest relatively little scatter should be present in the correlations from a stellar population forming from material enriched exclusively by non-conservative massive binary mass transfer. However, as seen in figure 3.4, the enriching binaries eject similar fractions of the system mass. Assuming a fixed fraction of mass loss, then enrichment in terms of absolute mass should scale as $\sim M_1$. Predicted IMFs have steeper slopes than $\sim M^{-1}$ for massive stars (Salpeter, 1955; Kroupa, 2001; Kroupa & Weidner, 2003; Chabrier, 2003). Additionally, the restricted P range for higher mass stars relative to lower mass stars means higher mass binaries are not common enough to introduce similar scatter into a stellar population as we see when plotting our binary ejecta. Due to the relative rarity of high-mass binaries, their primary effect on typical cluster abundances is expected to appear in the extremes or spreads.

Ejecta from binaries in the parameter space we simulate show, in terms of dex, large spreads in C, N, and Na; smaller spreads in He, O, Al, and Fe; and minimal spread in Mg.

We compare these spreads to observational expectations in section 4.2.1.

3.3 Comparison with solar-scaled binary yields

Although solar-scaled metal-poor stars are rare, and metal-poor GCs are generally modelled as alpha-enhanced stellar populations, some clusters are less alpha-enhanced than the typical levels for their metallicity (Nandakumar et al., 2022). The yields from our solar-scaled systems may be considered as a lower bound to what less alpha-enhanced binary stars may contribute to enrichment. Our solar-scaled models are simulated with the same $[\text{Fe}/\text{H}]$ as the alpha-enhanced ones, decreasing the metal mass fraction Z .

As we did for the alpha-enhanced runs in figures 3.1 and 3.2, we show the completed runs and the relative enrichment in HeNaCNO for the solar-scaled binaries in figures 3.28 and 3.29.

Of the 204 solar-scaled binaries we simulate, 181 eject sufficient mass through RLOF. 38 out of 183 reach core-C depletion, 29 initiate contact, and 66 reach unstable system mass loss rates. The other 48 do not reach any of these stopping conditions.

For the 23 binaries excluded from the sample, 19 do not initiate RLOF and 4 do not eject sufficient mass ($> 0.1 M_{\odot}$) before stalling. Compared to the alpha-enhanced binaries there are fewer complete binaries with $M_1 = 40 M_{\odot}$ due to fewer `varcontrol` settings tested as detailed in section 2.5.3.

In figure 3.30 we show the Na-N correlation and the Na-O anti-correlation for the solar-scaled binary ejecta. In general, the solar-scaled binaries eject material following the same trends as seen in the alpha-enhanced binaries. This is expected since regardless of the level of alpha-enhancement, massive stars will undergo high-T H burning. However, we note that the Na-N relation is tighter for the solar-scaled yields ($r_s = 0.9920$).

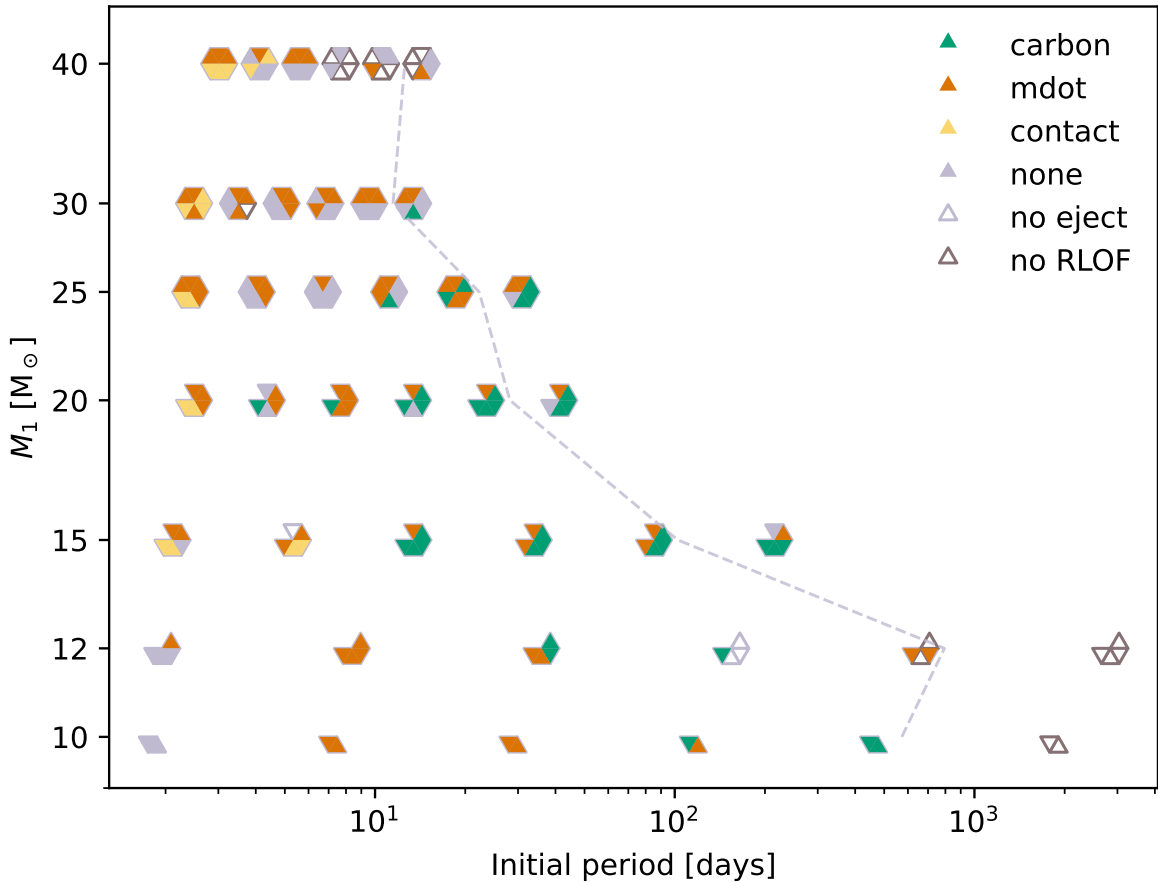


Figure 3.28: Solar-scaled binaries that we run in this work. Similar format as figure 3.1. 181 of the binaries undergo non-conservative mass transfer, with 38 reaching core-C depletion, 29 initiating contact, and 66 reaching unstable mass loss rates. The other 23 of the 204 binaries either do not initiate RLOF (19) or do not eject more than $0.1 M_\odot$ (4).

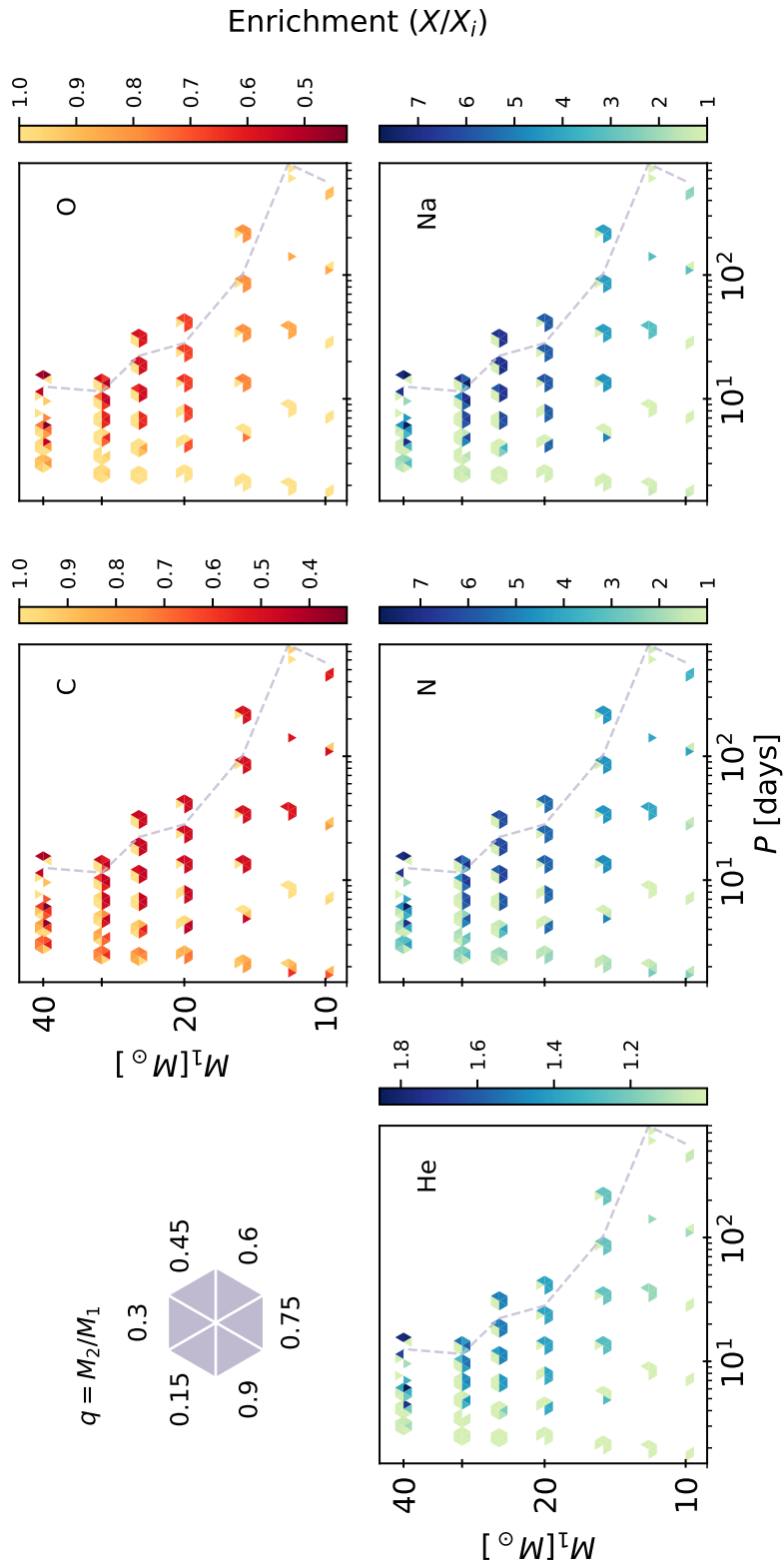


Figure 3.29: Similar to figure 3.2, but the enrichment from solar-scaled binary models is shown.

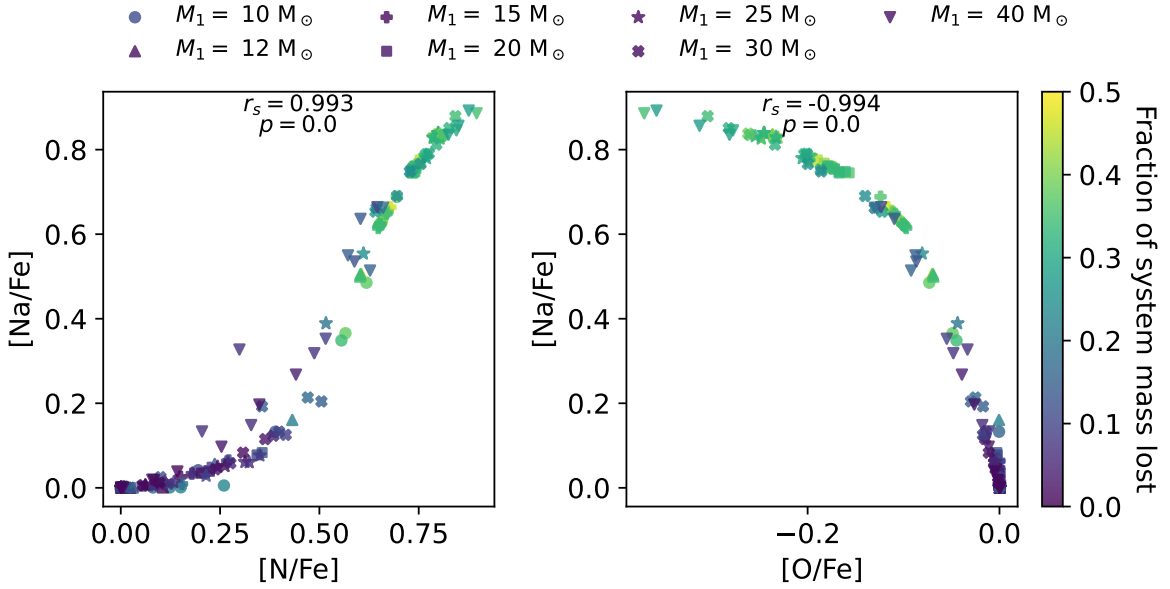


Figure 3.30: The Na-N and Na-O relations for binary ejecta from models with initially solar-scaled abundances, similar to figure 3.6 which was for alpha-enhanced models.

We calculate the expected values for the yields of a population of binaries using the solar-scaled models in the same way we do for the alpha-enhanced models in §3.2. The coverage of the solar-scaled binaries is slightly smaller than with our alpha-enhanced sample, at $\sim 57\%$ of the cubic volume rather than $\sim 60\%$. The typical mass ejected and timescales are similar between the solar-scaled and alpha-enhanced binaries, within a few percent of each other. However, the estimates of yields over the same space of single solar-scaled models are only $\sim 6.7\%$ of what they would eject as binaries, if including both the yield of the primary and secondary as single stars. If only considering the mass loss from the primary as the single star yield, it is about 4.6% of the binary mass loss. For solar-scaled binaries, the mass lost from massive binaries is even more significant relative to their mass loss as singles than for alpha-enhanced binaries.

3.4 Envelope ejection in alpha-enhanced binaries

101 out of the 190 binaries in our main sample were ended due to reaching contact or having unstable mass loss rates. As an upper limit on the ejecta that these binaries can end up producing, we calculate the yields including the ejection of the entire envelope of the primary. We compute this by taking the mass of the core of the primary from the `history` file and using the `profile` file at the nearest step to the end of the simulation to sum the mass in each isotope outside of the core. The mass of the core may not exactly match the shell boundaries in the profile if the profile is saved for a slightly earlier/later model, so we find the shell with the closest boundary to the core boundary and sum those masses. Each stellar model has thousands of shells so the difference in mass this causes is insignificant, $\lesssim 0.001 M_{\odot}$. For stars with these stopping conditions, the time steps are small such that the nearest `profile`'s model has negligible differences to the model exactly at termination.

The core of the star can be determined in a few ways: the central convective zone, the central nuclear burning zone, or from the transition of abundances. We compare the mass enclosed by all three and take the largest of the masses as the core mass.

In figure 3.31 we show the mass ejected from the system when we include the primary envelope. A few of the primaries in the runs that reach contact or unstable mass loss rates have already ejected practically their entire envelope mass, lying on the dotted line in the right panel. These are generally binaries with $M \lesssim 20 M_{\odot}$. Approximately $5 M_{\odot}$ or more remains in the primary envelope at termination for the rest of the systems. The binaries now eject as much as $\sim 60\%$ of the initial system mass compared to $\sim 50\%$ seen earlier with our main yields.

We show the Na-N correlation and Na-O anti-correlation when including envelope ejection for these binaries in figure 3.32. For comparison, the abundances of the original

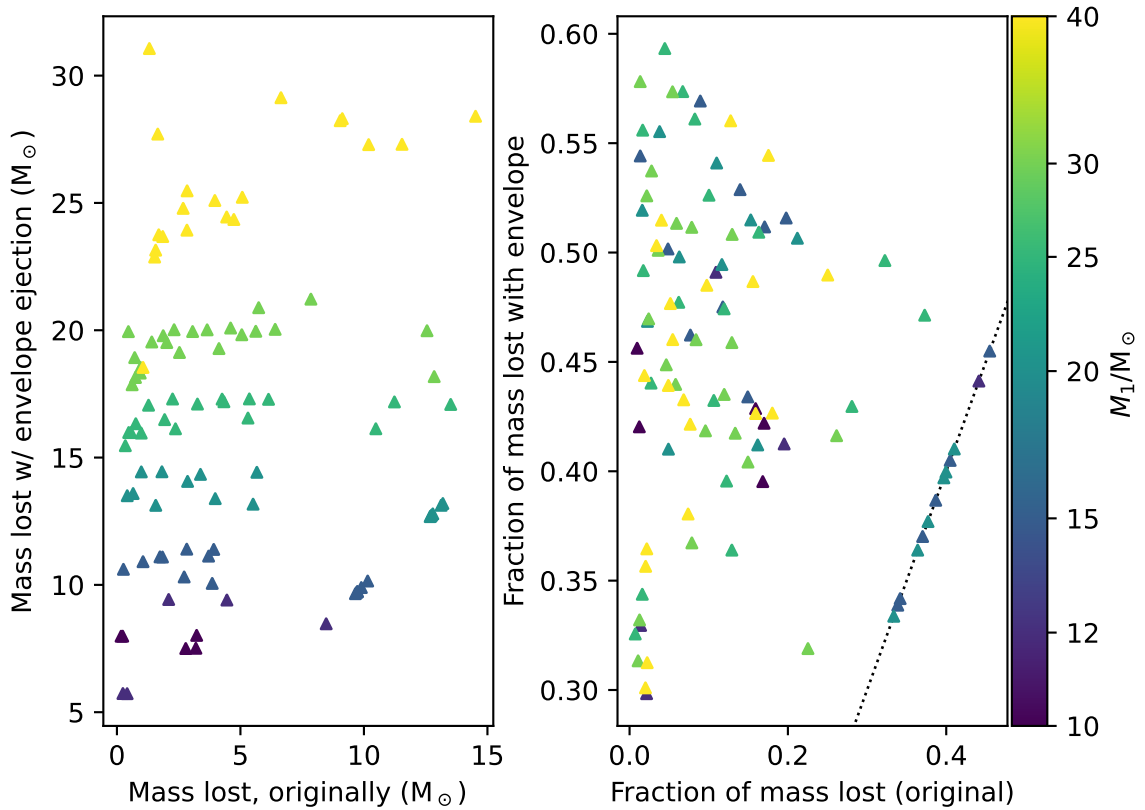


Figure 3.31: A comparison of the mass lost from systems as calculated up until reaching contact or unstable mass loss (on the x -axis) and when including the ejection of the primary (on the y -axis). The total mass ejected is shown in the left panel. The fraction of the initial system mass that was lost is shown in the right panel. In the left panel, the dotted line shows the 1:1 relationship, where no additional mass is ejected from the primary envelope. The colour map indicates the initial primary mass of the system.

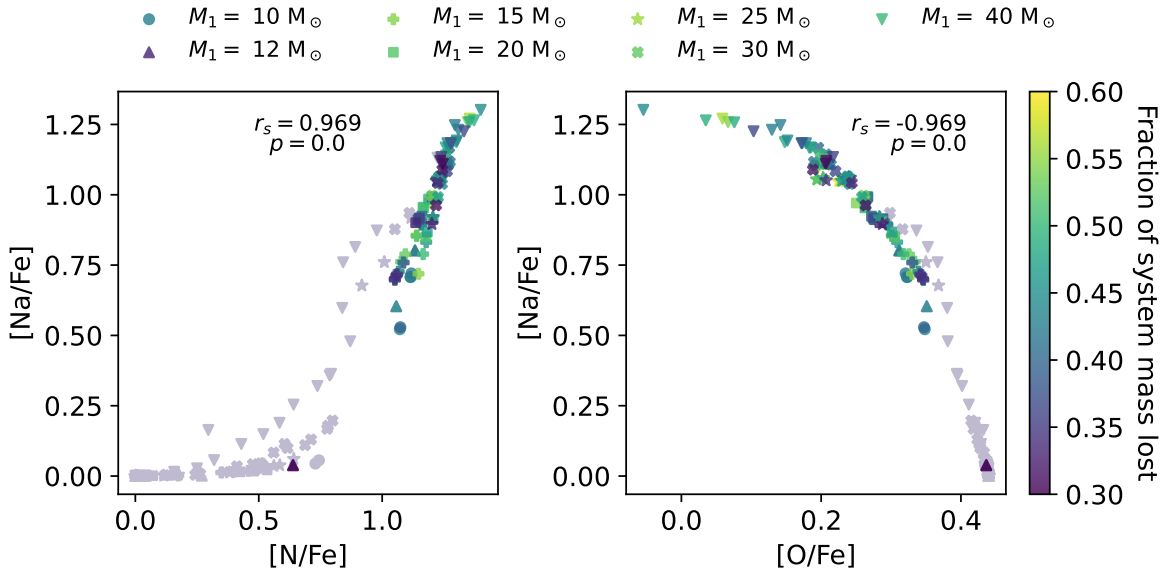


Figure 3.32: The Na-N and Na-O relations for the ejected material with primary envelope ejection for binaries reaching contact or unstable mass transfer. The coloured points each correspond to the total calculated yields of a binary. The grey points are the yields for those binaries without the additional envelope mass, which can be considered a lower limit for the yields of these binaries. At the top of each panel are the Spearman rank correlation coefficients and the associated p -value.

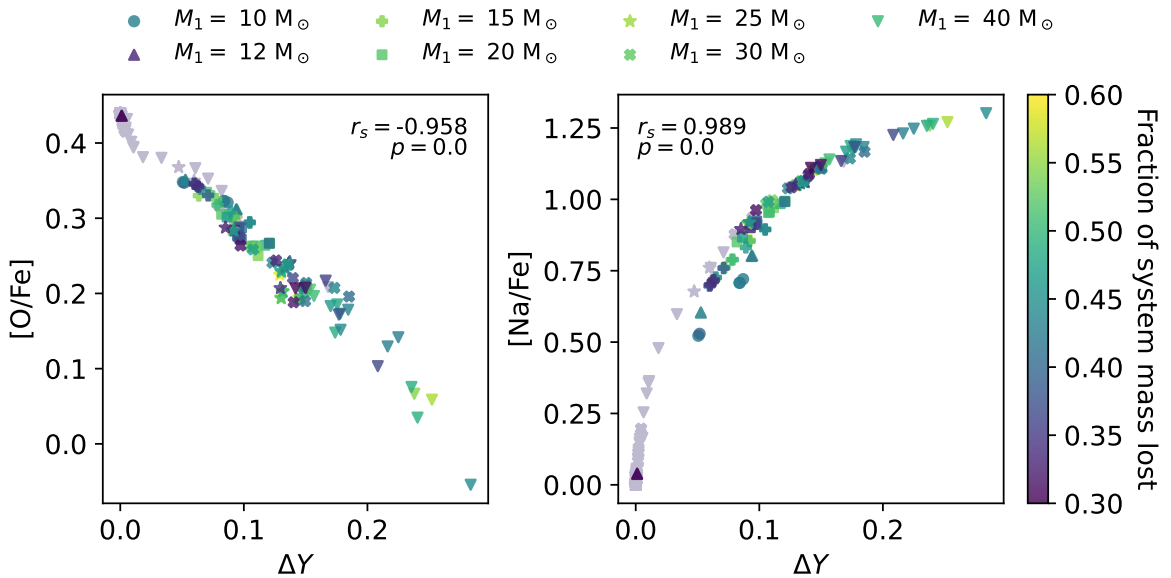


Figure 3.33: The relative change in [O/Fe] and [Na/Fe] from the initial composition as a function of the helium mass fraction increase seen ΔY . Similar format as figure 3.32.

ejecta calculated through modelling the non-conservative mass transfer in MESA are shown as grey background points. Both correlations are strong and binaries generally show much higher Na enhancement, N enhancement, and O depletion than they did without envelope ejection since there is high-T H-burned material remaining in the envelopes. All ejecta show significant [N/Fe] enhancement ($\gtrsim 0.06$ dex).

Similarly, we show the enhancement of [O/Fe] and [Na/Fe] relative to the enhancement in He, ΔY in figure 3.33. Apparent in both figures 3.32 and 3.33, some of the high mass binaries with $M_1 = 40 M_\odot$ eject material that is more enriched than in our unaltered yields. We now get maximum spreads of roughly $\Delta Y \sim 0.3$, $\Delta[\text{O/Fe}] \sim -0.5$, $\Delta[\text{Na/Fe}] \sim 1.3$, and $\Delta[\text{N/Fe}] \sim 1.4$. As expected and as seen in earlier sections, the yields from binaries are highly dependent on how much envelope mass they eject.

If envelope ejection is efficient in these systems and $\sim 1/2$ of the binaries in our parameter space are affected by incomplete ejection due to stopping conditions: then the expected yields per binary may be underestimated by as much as a few M_\odot . As such, a “typical” binary may eject $\sim 10 M_\odot$. We also expect relatively few binaries in our region would eject only unenriched material.

The yields from our envelope ejection calculations depend on how we define the envelope. Results, where we take the smallest, non-zero, core mass of the stars, are shown in figures 3.34, 3.35, and 3.36. For the majority of the binaries, the results are similar to results when using the largest core mass. However, the binaries now eject as much as $\sim 80\%$ of their system mass and they all eject more mass than they do in the initial sample as seen in figure 3.34. From figure 3.35, there are now binaries that exhibit a spread in [N/Fe] and a considerably enhanced [O/Fe] at the same [Na/Fe] previously seen. In the O-He and Na-He plots seen in figure 3.36 it is apparent that these binaries have ejected material that

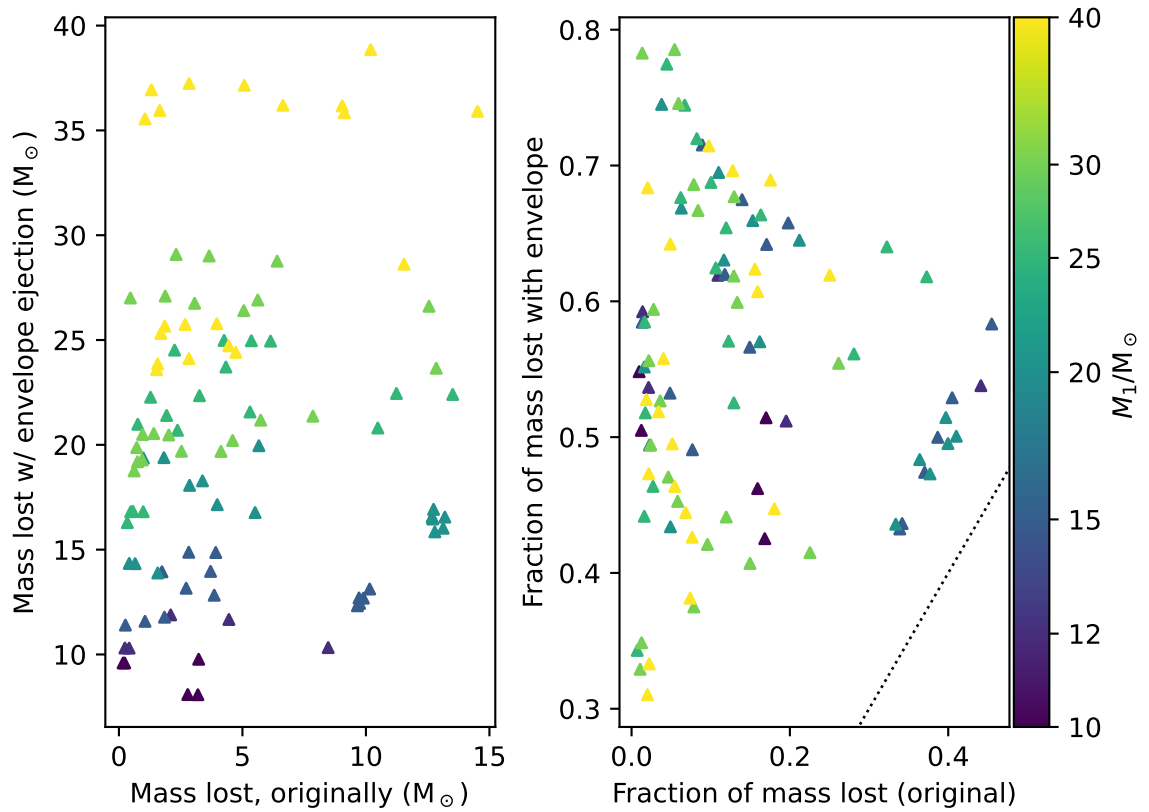


Figure 3.34: The ejected mass when including the largest possible definition of the envelope of the primary. The figure is analogous to figure 3.31.

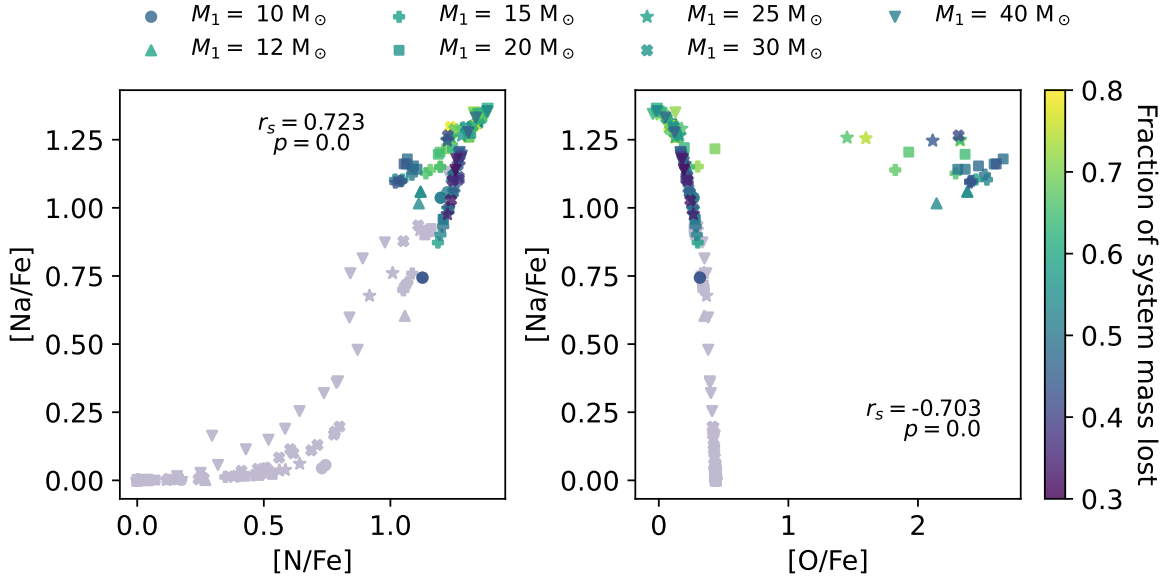


Figure 3.35: The Na-N and Na-O relations for the large envelope ejection calculations, similar to figure 3.32.

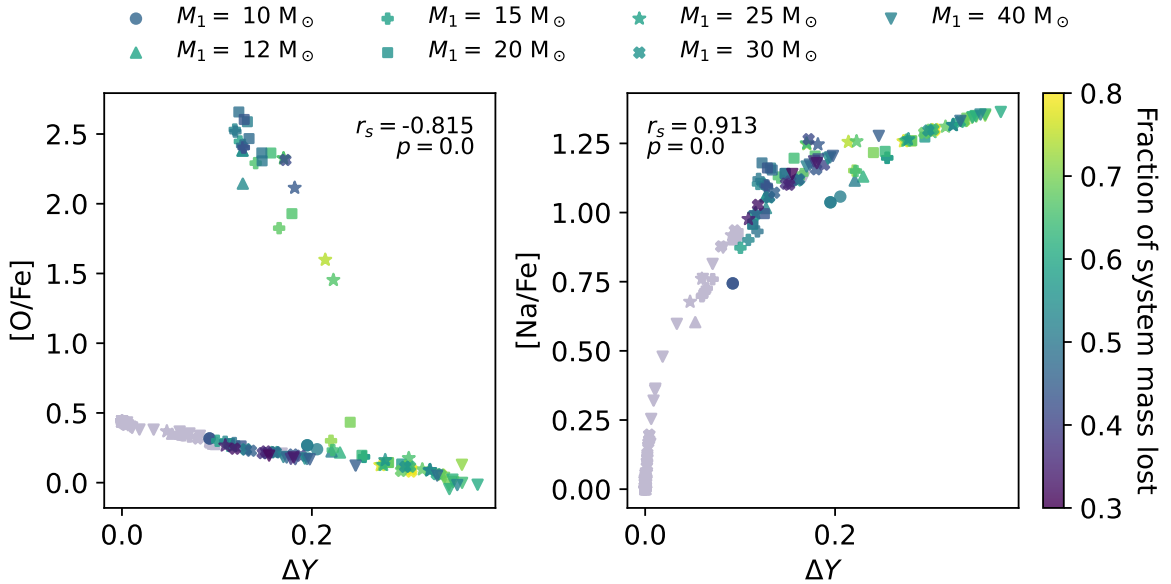


Figure 3.36: Similar to figure 3.33, but where the ejected envelope follows the largest defined envelope.

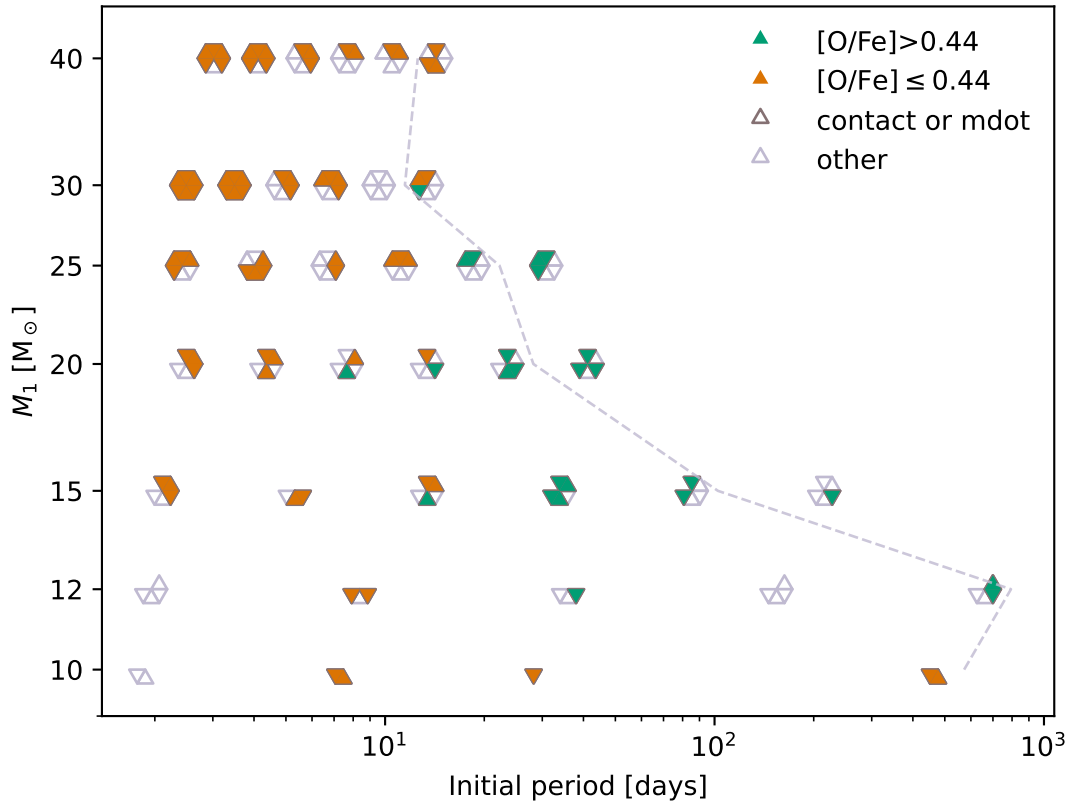


Figure 3.37: The parameter space occupied by the binaries for which we calculate additional primary envelope ejection. The colour of the points indicates if they contained He-burning products in their primary envelopes at their endpoints, resulting in an enhancement of $[O/Fe]$ as shown in the legend.

has undergone He burning as relative to the extreme enrichment of these trends, their ejecta is depleted in He and highly enhanced in O.

We show which runs enhance $[O/Fe]$ above the initial abundance in the parameter space plot in figure 3.37. When we use the smallest, non-zero, core mass to determine the envelope mass to eject, some binaries at intermediate to long periods eject material that has gone under He-burning. The fate of these binaries, particularly in how much mass the primary can eject at the end of their lifetimes, affects the ability of massive binaries to act as suitable enrichment sources.

Chapter 4

Summary and discussion

We simulated and analyzed the non-conservative mass transfer of 190 alpha-enhanced binaries within a range of $10 \leq M_1 \leq 40 M_\odot$, $0.15 \leq q \leq 0.9$, and $2 \lesssim P \lesssim 700$ days. These binaries eject as much as $\sim 50\%$ of their initial system mass. Within the parameter space, we find some binaries are enriching while others are not. This provides a mechanism to alleviate the need for the dilution of enriched material by natal cluster gas. Overall, the yields of our binaries produce the required qualitative trends in HeNaCNOAl. However, variations in heavier elements (iron-peak, and heavy alpha elements) are negligible. In particular, we find massive binaries can eject material enhanced in He, N, Na, and Al; depleted in C and O; with the associated abundance correlations that are hallmarks of high-T H-burning. These include the Na-O and C-N anti-correlations and the Na-N and C-O correlations. The C+N+O abundance and Fe abundance are constant in the ejecta.

Considering the expected values from a population of binaries following observed distribution functions, the depletion, enhancement, and constancy of these elements persist. Binaries within our parameter space are relatively rare, with primaries making up only $\sim 2.5\%$ of the total mass in primaries for a “typical” stellar population. This suggests that,

on their own, the binaries within our bounds cannot alleviate the mass budget problem in the formation of MPs. On average, binaries eject about 22% of their initial system mass ($6.7 M_{\odot}$) on a mass-weighted timescale of ~ 11 Myr. Some binaries, generally those at the highest mass we simulate $M_1 = 40 M_{\odot}$, eject material with extreme abundance changes relative to the IQR (middle 50%) of ejecta composition. The combination of rarity and extremity makes massive binaries a potential avenue for stochasticity.

Our analysis of 181 solar-scaled binary models indicates similar results as from our alpha-enhanced binaries.

Considering the envelope ejection of alpha-enhanced binaries that initiate contact or show unstable mass loss rates suggests stronger enrichment and more mass ejection is possible, while still preserving abundance correlations and anti-correlations. If envelope ejection is too efficient, ejecting especially deep layers, He-burning products contaminate the ejecta.

We discuss further implications of our results and avenues for future work in the remaining sections.

4.1 Grids of binary models

We demonstrate that massive binaries spanning a parameter space in M_1 , q , and P are enriching and that this mechanism is not isolated to systems similar to the one simulated by de Mink et al. (2009). These binaries eject material enriched in He, Na, N, and Al, and depleted in C and O, consistent with the abundance anomalies seen in enriched populations in clusters. Several binaries do not eject as large a fraction of their primary envelopes, ejecting unenriched material depleted in fragile elements only (Li, Be, B, F). The most enriching binaries have higher primary masses, longer periods, and higher mass ratios.

Higher mass primaries reach higher temperatures and densities in their cores, so we expect them to eject more processed material. Enriching binaries also tend to be the binaries that eject the largest portions of their initial system mass, as deeper portions of the envelope where processed material resides are ejected.

The influences of period and mass ratio are less direct. Shorter periods and higher mass ratios correspond to stronger tidal forces which can lead to greater rotational mixing and more accretion by the secondary. Longer initial periods mean the primary initiates mass transfer at later evolutionary phases and can lead to the primary overflowing its Roche lobe more significantly. For binaries that undergo multiple phases of mass transfer, the influences of period and mass ratio are complicated by the mass loss of the primary and the evolution of the period due to mass transfer leading up to each additional phase of mass transfer. Spin down of the secondary between phases of mass transfer also affects how much mass the secondary can accrete before the mass transfer becomes non-conservative again. Although, we reiterate that the secondary generally accretes $\lesssim 1 M_{\odot}$ from the primary.

Short-period binaries are likely to initiate contact, which we do not simulate. Similarly, lower mass ratio binaries are more likely than high mass ratio binaries to have unstable mass loss rates. When we considered the envelope ejection of the primary in section 3.4, we see that the majority of these systems can be enriching if they effectively eject their envelopes. In general, these systems are not expected to eject their entire envelopes. We also did not consider the possibility of envelope ejection from the secondary, which would reduce the enrichment by incorporating less-processed material.

First, we discuss the general, qualitative, properties of binary ejecta in the context of the observations of clusters. We consider the implications of enrichment values and spreads in section 4.2.

4.1.1 Light element abundance correlations

The ejecta of massive binaries naturally produces the main abundance trends observed in MPs, with Na-N, C-O, He-Na, Al-N correlations and Na-O, C-N, He-O anti-correlations at high confidence, $p > 0.999$. Massive binary ejecta also preserves C+N+O number abundance. These are intrinsic to the HeNaCNOAl variations caused by high-temperature hydrogen burning. Since these correlations are generally tightly monotonic $r_s > 0.95$ and some binaries eject non-enriching material, stars that form from this binary-ejected material should still preserve the (anti-)correlations even with mixing and additional dilution. Unlike AGB stars, dilution from primordial gas is unnecessary in producing an Na-O anti-correlation.

The spread seen in $A(\text{C+N+O})$ due to He variation is also generally consistent with no spread in observations, where typical uncertainties are $0.05 \sim 0.1$ dex (e.g. Masseron et al., 2019; Mészáros et al., 2020).

4.1.2 Magnesium

Our models also produce an Mg-Al correlation that is seen in some clusters. This correlation is relatively small due to the small variation in Mg, at a maximum level of ~ 0.02 dex. Larger spreads may be possible with higher-mass primary binaries. The ejected material tends to be depleted in Mg^{25} , sometimes showing depletion or minor enhancement in Mg^{26} , with no change in Mg^{24} . This contrasts to expectations in AGB yields where Mg^{25} is enhanced with $\text{Mg}^{25}/\text{Mg}^{24}$ higher than $\text{Mg}^{26}/\text{Mg}^{24}$, both of which are at odds with expectations with observations (Thygesen et al., 2016; Ventura et al., 2018). The yields from massive binaries are more consistent with observed isotopic ratios. However, the range of $[\text{Mg}/\text{Fe}]$ seen in our ejecta is much narrower than observed (e.g. 0.5 dex in metal-intermediate GCs NGC

6205, NGC 2808; Ventura et al., 2018). Larger spreads in $[Mg/Fe]$ can be produced in AGB simulations, but in general nucleosynthetic rates for the key Mg and Al reactions are uncertain (Ventura et al., 2018). Relatively few clusters have measurements of their Mg isotopic abundances, so there is a need for constraints on both the theoretical and observational ends to utilize them to distinguish enrichment sources.

4.1.3 Lithium and fragile elements

Although all of our massive binary ejecta were depleted in Li (Be, B, and F), we do not find a considerable depletion of Li in ejecta enriching in HeNaCNO compared to non-enriching ejecta. Li abundance in both selections can vary considerably by as much as ~ 2.5 dex, though many of the enriching binaries ejected more Li-poor ejecta than many non-enriching binaries. As the hot-H burning temperatures destroy Li, this is one of the challenges in explaining all Li variations among MPs. The depletion of Li in both enriching and non-enriching material may explain why the relative Li abundance between enriched and unenriched populations in clusters is not unidirectional if both contain stars forming from massive binary ejecta.

4.1.4 Variations in heavier elements

The ejecta from our binary does not show significant differences in the heavy elements: Fe, Si, Ca, Ti, Ni, and Cr. This includes iron-peak elements Fe, Ti, Cr, and Ni; and alpha-elements Si, Ca. As such, our binary yields cannot explain the formation of MPs with variations in their heavy elements. With 15~20% of photometrically studied clusters with MPs having heavy element abundance variations, other sources or formation theories are needed to explain these clusters (Milone & Marino, 2022). These anomalous clusters may

be impacted by longer star formation times, allowing for the pollution of heavy elements, or due to their similarities to dwarf galaxies, be remnants or cores of former dwarf galaxies (Milone & Marino, 2022). Recent spectroscopic measurements of cluster NGC 6752 by Schiappacasse-Ulloa & Lucatello (2023) indicate variations in the heavy elements are not linked to those in the light elements.

Overall, binaries reproduce many of the ubiquitous trends seen with enrichment but cannot produce all abundance variations associated with MPs on their own.

4.2 Suitability of massive binaries as sources of enrichment

Based on our results on the yields from a typical binary population, we can assess how well binary ejecta quantitatively matches the expectations for an enrichment source. In particular, we focus on He, C, N, O, Na, Mg, and Al.

In comparing our binary yields directly to the MP properties in clusters, we do not include the effects of dilution and mixing of gas or stellar evolution of the stars that would form out of the ejecta. As such, we only consider if the yields from massive interacting binaries are consistent under the self-enrichment scenario, with minimal and relaxed assumptions about the details. Discrepancies between our predictions and the observed properties indicate issues with our assumptions about binaries as the sole enrichment source and the general picture of self-enrichment.

4.2.1 Abundance spreads relative to observations

We compare our typical yields and spreads to observations using large surveys. Mészáros et al. (2020) analyze the spectra homogeneously for stars in a total of 31 globular clusters,

with data from the Apache Point Observatory Galactic Evolution Experiment 2 (APOGEE-2) survey and the Sloan Digital Sky Survey (SDSS-IV). This expands on previous work of Masseron et al. (2019). They consider Al-Mg and C-N relations and cover Fe, Mg, Al, C, N, and O. Their spreads in abundance are reported as RMS scatter. We also compare our results to measurements of He, C, N, O, Na, Mg, Al, and Fe from (Marino et al., 2019) and (Milone et al., 2018), as part of the Hubble Space Telescope (HST) UV Legacy Survey of Galactic Globular Clusters. They measured He abundances for 57 clusters and listed spreads in C, N, O, Mg, and Al in their tables 2 (for the difference between populations) and 3 (for the maximum difference). They combine spectroscopic and photometric data to derive their abundances. Marino et al. (2019) utilize photometric chromosome maps to determine N, O, Na, Mg, Al, and Fe abundances for 29 GCs, showing the distribution of their abundance spreads between the enriched and unenriched populations for the clusters in their figure 7. As our binary ejecta tends to not correspond to material with heavy-element variations associated with MPs, we only compare our results to their results for typical MPs.

The observed extremes in ΔY from our yields cover the entire range of observed He variations, which are as high as 0.124 dex (NGC 2808) for the maximum He variation (Milone et al., 2018). The average difference in Y between the enriched and unenriched population for all clusters analyzed in Milone et al. (2018) was ~ 0.01 dex, with the largest difference being ~ 0.048 dex. With our yields showing $\text{IQR}=0.078$ and $\sigma=0.049$ dex, both values are consistent with observations. The lower average variation of Y between the observed populations suggests there may be more dilution of the yields than at the level included from the ejecta of non-enriching binaries in our parameter space.

Milone et al. (2018) also show that the width of He variation correlates with the cluster mass. As noted in section 3.2, the spreads from binary ejecta are expected to increase with

cluster mass as higher mass binaries are sampled due to their relative rarity.

The scatter of N in clusters measured by Mészáros et al. (2020) ranges from ~ 0.1 - 0.5 dex. They find a weak positive correlation of the N scatter with $[\text{Fe}/\text{H}]$, with the typical scatter being ~ 0.25 dex at our simulated metallicity. Only 3 typical clusters in Marino et al. (2019) have measured $[\text{N}/\text{Fe}]$ with their $\Delta[\text{N}/\text{Fe}]$ falling between 0 and 0.5 dex. The spreads used in Milone et al. (2018) range from 0.3 to 1.1 dex. All these spreads are within our predicted $\Delta[\text{N}/\text{Fe}]$, with the extremes at 1.337 dex, IQR of 0.556 dex, and σ of 0.392 dex. Our median $[\text{N}/\text{Fe}]$ was relatively high at 0.983 dex. The clusters of similar metallicity in Mészáros et al. (2020) have their least enriched stars near $[\text{N}/\text{Fe}] \sim 0.5$ dex. Dilution of binary ejecta with primordial material to bring the median $[\text{N}/\text{Fe}]$ down could still have spreads on par with observations, as our undiluted yields have slightly larger spreads than the observed values.

In the work by Marino et al. (2019), the $\Delta[\text{Na}/\text{Fe}]$ observed has a mean of ~ 0.35 dex with values ranging from 0 to 0.9 dex. The IQR and σ for $[\text{Na}/\text{Fe}]$ in our binaries are 0.677 and 0.37 dex, respectively. The σ is similar to the mean $\Delta[\text{Na}/\text{Fe}]$ seen in the observations but is low if considerable dilution occurs. However, the IQR is significantly higher and could cover the typical spreads. The extreme of $\Delta[\text{Na}/\text{Fe}] = 1.337$ (with 75th percentile 1.109 dex) would easily explain the presence of the most Na-enhanced observations.

As determined by Mészáros et al. (2020, figure 17), the typical spread of $[\text{C}/\text{Fe}]$ is ~ 1 dex at the extremes. For the clusters with similar metallicities of $-1.458 \leq [\text{Fe}/\text{H}] \leq -1.402$, the typical maximum spread is ~ 0.5 dex. The range of $\Delta[\text{C}/\text{Fe}]$ adopted by (Milone et al., 2018) range from 0 to -0.7 dex. Our maximum $\Delta[\text{C}/\text{Fe}]$ of -0.477 is in rough agreement with the observations of clusters at a similar metallicity to our simulated binaries. However, the yields from our binaries cannot explain the full range of $[\text{C}/\text{Fe}]$ observed in other clusters.

As measured by Mészáros et al. (2020), Al scatter is roughly 0.35 dex for $[\text{Fe}/\text{H}] < -1.3$ dex or $\gtrsim 0.2$ dex when excluding extreme $[\text{Al}/\text{Fe}] > 0.3$. The $\Delta[\text{Al}/\text{Fe}]$ considered by Marino et al. (2019) range from 0 to 0.8 dex with a mean of ~ 0.5 dex. Similarly, Milone et al. (2018) consider $[\text{Al}/\text{Fe}]$ spreads ranging from 0 to 1 dex. Typical spreads seen by Mészáros et al. (2020) correspond to a similar level of $[\text{Al}/\text{Fe}]$ as seen in our most extreme Al-enriching binaries. The IQR and σ we obtain are too small to explain these spreads (0.138 and 0.084 dex). The mean and upper limits of $[\text{Al}/\text{Fe}]$ observed by (Marino et al., 2019) are too large for our expected yields.

We noted that our anti-correlation between Mg-Al occurred over a short range in $[\text{Mg}/\text{Fe}]$. The typical spreads seen by (Mészáros et al., 2020) span about 0.4 dex. Marino et al. (2019) find the typical $\Delta[\text{Mg}/\text{Fe}]$ to be zero with some clusters exhibiting spreads as low as ~ -0.3 dex to ~ 0.1 dex. Spreads $\Delta[\text{Mg}/\text{Fe}]$ used for clusters analyzed by (Milone et al., 2018) range from -0.25 to 0 dex which is not covered by our extremes. Massive binary ejecta for binaries in the parameter space we simulate does not appear to produce large enough ranges in Al and Mg on their own.

From the measurements of Mészáros et al. (2020), maximum spreads in $[\text{O}/\text{Fe}]$ are ~ 1 dex. The typical mean $\Delta[\text{O}/\text{Fe}]$ seen by Marino et al. (2019) is ~ -0.25 dex, though they get as large as ~ -0.5 dex. Uncertainties on their individual measurements of $[\text{O}/\text{Fe}]$ were typically 0.1~0.2 dex. The $\Delta[\text{O}/\text{Fe}]$ used by Milone et al. (2018) to determine He spreads ranged from 0 to -1 dex. In general, our binaries do not produce the required O spreads, with the extreme depletion leading to only a -0.357 dex change in $[\text{O}/\text{Fe}]$. The typical spreads we predict with an IQR of 0.119 dex and a σ of 0.076 dex are also small relative to observations. This highlights the issue discussed by Bastian et al. (2015) about the yields from de Mink et al. (2009), the predicted O spread from our model is too narrow. The

inclusion of other sources that do create the observed [O/Fe] spread can help the enrichment to better follow the observed relations. We note that Bastian et al. (2015) also suggest that relatively large He variations should be seen for a given [O/Fe] or [Na/Fe] to capture the stochastic nature of clusters. In our models, higher [O/Fe] depletion and scatter in the O-He and Na-He relations were associated with high-mass primary systems. If binaries above $M_1 = 40 M_\odot$ continue with these trends, then massive binaries can eject larger [O/Fe] spreads and also have higher O-He and Na-He variability. The relative increase in [Na/Fe] with primary mass is smaller than in [O/Fe] at high mass in our samples, given the spreads in figure 3.17. So, higher mass stars may make the relative spreads in [O/Fe] and [Na/Fe] more on par with observations. However, this is also associated with larger He spreads, so ample dilution is required.

To examine the Na-O correlation further we also make comparisons to empirically calibrated determinations of the IQR of [O/Na] in 95 GCs by Carretta (2019). Calibrations were performed using spectroscopic measurements of 22 GCs. In particular, we compare their measure labelled IQR2 which is calculated for 117 GCs. As noted in 3.2, our [O/Na] IQR is about 0.2 dex larger than the typical IQR seen in their estimations. The spread in [O/Na] is relatively wide, covering ~ 1.5 dex. The most extreme [O/Na] IQR calculated by Carretta (2019) is within this range, at ~ 1.2 dex. Due to the coverage of this IQR and the spread of [Na/Fe] by our models, it is clear that the extent of the Na-O relation in our binary ejecta is sufficiently large. However, the direction or slope of our Na-O anti-correlation is too steep in Na relative to O.

Relatively small scatters in O relative to Na have been observed in a few clusters, resulting in “vertical” Na-O relations (Muñoz et al., 2020, and references therein). These are generally not typical of metal-intermediate or metal-poor clusters.

The abundance spreads seen in He, N, and Na in MPs show agreement with predictions from the expected yields of alpha-enhanced binaries in our parameter space. C and Al show some similar, but also larger, variations in observations to what our binaries produce. Mg and O have short extents in our binary yields compared to observations, indicating the need for higher mass binaries, additional enrichment sources, and/or different MP formation scenarios.

We also consider the variation of Li in the context of observed MPs. The typical $A(\text{Li})$ seen in our ejecta, ~ -0.32 dex is drastically lower than the inferred initial abundance of the observed stars $A(\text{Li}) \sim 2.1 - 2.3$ dex in 5 GCs showing similar Li abundances between enriched and unenriched stars by Aguilera-Gómez et al. (2022). This is in part due to the assumption of initially solar $[\text{Li}/\text{Fe}]$, leading to an initial $A(\text{Li}) < 2$ dex. If we consider the primordial $A(\text{Li})$ to be 2.72 dex (Cyburt et al., 2008), then the destruction of Li in the massive stars still brings down the typical $A(\text{Li})$ to ~ 1.2 dex. This is too depleted to correspond to the observed clusters. We note that the primordial Li abundance is controversial (see Norris et al., 2023; Fields & Olive, 2022; Cyburt et al., 2016). The IQR is relatively large, at ~ 0.4 dex. This is similar to the spreads observed in the RGB stars of Aguilera-Gómez et al. (2022), but this is after these stars have evolved their Li abundances. Marino et al. (2019) show the measurements of $A(\text{Li})$ for stars in 5 clusters, seeing a maximum spread from $A(\text{Li}) \sim 0.4$ to ~ 1.4 . A spread of 1 dex in $A(\text{Li})$ is well within the maximum spread of $A(\text{Li})$ we obtain in our binary ejecta. For material that has only been enriched (or has been dominantly enriched) by massive binaries, extreme dilution with primordial gas must occur before forming the enriched population, or the enriched and unenriched populations need to be coeval out of the ejecta that has been processed by massive binaries. The issue of depleted Li can also be alleviated by mixing with gas from AGB stars which are predicted

to produce Li (Bastian & Lardo, 2018).

4.2.2 Timescales

The typical timescale we find for non-conservative mass transfer is 11~12 Myr. This agrees with measured age spreads between enriched and unenriched populations observed in clusters (-6 ± 12 Myr, Saracino et al., 2020; 1 ± 20 Myr, Martocchia et al., 2018; 17 ± 170 Myr, Oliveira et al., 2020). Though greatly lacking constraints, massive clusters may be capable of forming stars over periods of ~ 20 Myr (Eldridge et al., 2013; Krumholz et al., 2019). As such, binary ejecta can be diluted by pristine cluster gas and go on to form stars. However, this likelihood also depends on how effectively the ejecta can collapse to form stars. Dependence on the ejecta properties (velocity, temperature) and the surrounding gas properties will affect how shortly after ejection the formation of a new stellar population can occur. We also note that the enrichment provided by high-mass binaries occurs sooner than that of lower-mass primaries. If more massive stars than $40 M_{\odot}$ as primaries in binaries undergo non-conservative mass transfer in a given cluster, more mass will be ejected on shorter timescales than we already see.

The average timescales are longer than the expected timescale that the first core-collapse SNe occur on ($3 \sim 8$ Myr). Spreads of Fe and other abundance variations can be affected by the yields of SNe in this case (Bastian & Lardo, 2018).

4.2.3 Mass budget

A strength of interacting binaries is that they can eject considerable fractions of their initial mass, with a typical value for our sample being 22%. This is higher if binaries that reach contact or unstable mass loss also undergo significant envelope ejection. As our binaries

eject $6 \sim 10\times$ what they would as single stars and most massive stars are in multiples, this is a considerable mass loss. Treating these stars as singles would greatly underestimate the mass ejected by high-mass stars before the end of their lifetimes.

The ejection of non-enriching material by some binaries can also alleviate issues with the mass budget in terms of providing mass for dilution.

For a Kroupa IMF with $0.08 < M < 150 M_{\odot}$ as the limits, $\sim 20\%$ of the mass in primaries is in the massive stars ($\geq 10 M_{\odot}$). For massive stars with $M \leq 40 M_{\odot}$, this fraction is about 12% of the total primary mass. If we assume that the typical fraction of 22% of the system mass being lost is consistent over the entire massive star range only as much as $\sim 7\%$ of the total initial primary mass is ejected by massive binaries (for average $q \sim 0.5$). We note that an underestimation of this quantity comes from not simulating the envelope ejection of some binaries in our sample (e.g. contact, unstable mass loss). The expected mass from all massive binaries is also subject to overestimation, as not all primaries will be in an interacting binary, as well as variation due to the different distributions in primary mass, period, and q . Massive binaries are expected to eject similar masses to what is expected for other enrichment sources but do not fully resolve the mass budget problem (de Mink et al., 2009; Bastian & Lardo, 2018).

Interacting binaries are also relatively rare overall, based on sums of the probabilities enclosed by our binary parameter space. This limits their usefulness in alleviating the mass budget problem in terms of absolute mass.

4.2.4 Stochasticity

The relative rarity of binaries and the complex parameter space affecting mass transfer supports the idea that massive binaries can explain the stochastic nature of MPs. $M_1 =$

$40 M_{\odot}$ binaries are the most extreme in our sample, while also being the rarest. Higher mass stars ($M_1 > 40 M_{\odot}$) are rarer and may eject even more (unusually) enriching material. The ejecta from massive binaries, with similar fractions of system mass ejected for each primary mass, are also likely to contribute to the formation of more stars than lower-mass ones. In this scheme, a few “unusual” binaries can cause variations in a particular cluster’s chemical abundances.

The rarity of interacting binaries can also explain how spreads increase with cluster mass. Massive binaries are rare enough that they are not fully sampled in low-mass clusters. This is coupled with the expectation that binaries form more readily in dense environments and with interactions being more common due to dynamical interactions tightening binaries. With higher relative probabilities of high-mass clusters hosting high-mass, interacting binaries, the maximum spreads in enriched abundances are larger.

4.3 Caveats and additional considerations

4.3.1 Limitations of our parameter space

We preferentially selected the parameter space of binaries to be ones we thought were likely to provide enrichment. In particular, we restricted lower-mass $M_1 \leq 20 M_{\odot}$ systems to high q progressively, with only $q = 0.75, 0.9$ for $M_1 = 10 M_{\odot}$. Based on the radius at core-He ignition, we typically restrict the upper period limit with higher M_1 . Most of our selections are so hot-H burning products that are in the envelope of the primary and accessible for ejection. Our lower limit on period ensures that the systems eject mass after core-H processing. This means that we are excluding the binaries that initiate RLOF earlier and are more likely to eject unenriched material. We note however, that (Moe & Di Stefano,

2017) only report binary period distributions down to $\log(P/\text{days}) = 0.2$, or $P \sim 1.6$ days.

We also do not simulate low-mass stars with low mass ratios that are also enriching. The omission of low- q systems for low-mass binaries also limits the non-enriching binaries simulated.

Due to the narrow range of periods associated with core-H exhaustion and core-He ignition in the higher mass end of our primaries, we did not simulate high-mass long-period binaries. For $M_1 \gtrsim 15 M_\odot$, our highest-period binaries generally initiate non-conservative mass transfer. This indicates that for these high masses, we are neglecting a parameter space where interacting binaries lie. These binaries have the potential to eject more enriching material, but may also eject material contaminated with more advanced burning products. In the case that contamination occurs, the yields may be similar to what was seen with the maximized envelope ejection in section 3.4.

The omission of more non-enriching and binary ejecta with more extreme abundance variations skews our calculated spreads to be smaller.

From our simulations, we can describe which are enriching as well as the yields we obtain from them. However, the implications of their ejecta on MP formation are dependent on assumptions of cluster formation.

4.3.2 Impact of stopping conditions

We do not follow the evolution of the binary until the end of its lifetime due to the limitations of our implementations in MESA. In particular, we do not go as far as SNe nor do we simulate contact phases or unstable mass loss phases of binaries. Under our current prescriptions, these phases cannot be reliably simulated.

For a complete understanding of the MP formation scheme, the timing, composition,

and energetics of the SNe ejecta are necessary. SNe are expected to pollute the cluster gas with higher levels of iron and to affect star formation in the cluster as gas is blown out by the highly energetic envelope (Wirth et al., 2021). Their ejecta is also expected to be enriched by more advanced burning products, which will disrupt the abundance trends seen in MPs in clusters. As multiple populations exist at the same iron abundance in many clusters, stars must be able to form from an enrichment source before the explosion of these SNe under the typical self-enrichment scheme. We do not know when these models will undergo an explosive phase, nor do we know how much mass will be ejected, based on how far our simulations run now. From section 3.4, where we considered envelope ejection, we do know that extreme ejection of the outer layers of the primary can eject He-burning products in our binary parameter space. This highlights the need to constrain the potential yields of massive binaries, up until the end of their lifetimes.

4.4 Future work

4.4.1 On interpreting binary yields for multiple population formation

For our calculations of the typical yields for a population of binaries, we essentially summed the contribution of all of the yields. We disregarded two aspects that would be important for the subsequent properties of the formed stellar population: spatial separation and temporal separation.

Especially with the interacting binaries being relatively rare, pockets of enriched material from their ejecta are expected. Mixing is not expected to occur uniformly between all of the yields. The timescale of binary mass ejection varies in our simulations, which further separates which yields can mix and can impact when stars form.

To understand the properties of the stars that form from the binary ejecta, yields should be implemented into a cluster formation simulation that includes binaries. Including stellar feedback and evolution would allow for consistent modelling of the entire self-enrichment scheme. It could be determined if sufficient gas mass is retained and enough enrichment is ejected to produce an enriched population fraction of $\sim 50\%$. Modelling the dynamics of the stars also means that the ejection of unenriched stars and enriched stars can impact the fractions of the populations. This could be done as an extension to the cluster formation simulations of Cournoyer-Cloutier et al. (2023).

Based on our expected yields, especially for Mg and O, other sources are expected to significantly impact our abundances. The mass ejected by interacting binaries overall is also too small to accommodate the mass fraction, further suggesting the need for a variety of sources. The yields from other enrichment sources could be implemented simultaneously to investigate the enrichment provided by these combinations of sources. Since the timescales vary between enrichment sources, the time evolution in cluster formation simulation will be an important factor in understanding the interplay between enrichment sources. This would be one of the major tests of whether the self-enrichment scenario can produce MPs.

With the simulation of multiple clusters, the properties of MPs in populations of GCs can be investigated. MP properties could be tagged onto star clusters within a galaxy formation simulation. This may be helpful in understanding the influence of processes like mergers. Additionally, tests of the dependence of MP properties on their host star cluster can be examined. For example, trends of abundance spreads with cluster mass, age, and metallicity. In particular, it would be interesting to see how the disruption of low-mass clusters over time impacts the MPs observed in the remaining cluster population. The disruption of clusters would also provide insight into the relative absence of enriched stars

in the field.

4.4.2 On binary simulations

The relatively small spreads of O and Mg that we see in our binaries may be improved with an extension of our parameter space to higher masses and for the high- M_1 binaries, to longer periods. Higher mass primaries burn hydrogen at higher temperatures and more enriched layers tend to be ejected for longer periods. More coverage of the parameter space overall will also be helpful for implementation in larger-scale simulations, providing a grid of consistently-calculated binary ejecta. This extension will also show how our limited parameter space is impacting the ability of massive interacting binaries to match the abundance spreads of MPs.

To consider how the abundance variations change with the metallicity of the host cluster, additional grids of binaries simulated with different initial metallicities are needed. Ideally, the range of metallicities tested would span the whole range observed in GCs, $-3 \lesssim [\text{Fe}/\text{H}] \lesssim 0$.

Another area for improvement beyond this work is in the simulation of the binaries to the end of their lifetimes. This would resolve how much mass truly gets ejected from the system and also determine if and when these systems become SNe. If these binaries do become SNe, simulating the ejection in detail may be necessary to understand the impact it has on the surrounding cluster gas. This can be implemented through the coupling of MESA to STELLA (Paxton et al., 2018; Blinnikov & Sorokina, 2004; Baklanov et al., 2005; Blinnikov et al., 2006).

With regards to running binaries past our stopping conditions, efforts are being made to simulate contact phases and unstable mass transfer using MESA (e.g. Fabry et al., 2022,

2023; Temmink et al., 2023; Marchant et al., 2021). As prescriptions and implementations for simulations of these phases are being developed, they could be applied to simulate our binary models past our current limitations.

In simulating our binaries and extrapolating/interpolating yields we made a few assumptions about their properties.

All of our simulations assume initially circular orbits. Eccentricity affects mass transfer, as RLOF can be initiated on an eccentric orbit near perihelion where it would not be on a circular orbit of the same orbital period (Moe & Di Stefano, 2017). This can impact the number of binaries expected to undergo interaction. Simulating a few systems with different initial eccentricities would indicate how significant the eccentricity is for the yields.

We do not consider higher-order multiples, under the assumption that we are simulating the inner binary. Simulating triples and beyond is not currently implemented in MESA. Triples increase the likelihood of the inner binary interacting, relative to an isolated binary, from $\sim 52\%$ to $\sim 67\%$ according to models by Kummer et al. (2023). As such, we may be underestimating the contribution of binary ejecta by not considering higher-order multiples. RLOF involving the outer tertiary are rare ($\sim 0.06\%$ of all triples), so the yields of outer stars in higher-order multiples should be largely irrelevant (Hamers et al., 2022). Simulating some triple systems may be useful for determining an upper limit of mass ejected and abundance trends from multiples.

Appendix A

Base inlists and files

Here we provide the base inlists used to run our binaries, the `run_star_extras.f90` to set additional settings, and `run_binary_extras.f90` used to calculate the yields of the ejecta. Inlists are based off of Paxton et al. (2015) and Choi et al. (2016).

List of files

1	Binary inlist (<code>inlist_project</code>)	133
2	Primary inlist (<code>inlist1</code>)	134
3	Secondary inlist (<code>inlist2</code>)	138
4	Extra settings (<code>run_star_extras.f90</code>)	142
5	Extra calculations (<code>run_binary_extras.f90</code>)	149

File 1: The inlist setting the binary controls.

```

! Modified inlist from:
! MESA VERSION: r7624
! Reproduces figure 8 of Paxton et al. 2015
! To use, make a local copy of $MESA_DIR/binary/work, copy the provided
! run_binary_extras.f (use the default run_star_extras.f),
! compile it (./clean && ./mk) and copy
! inlist1, inlist2 and inlist_project there.
! To switch between the tide form Hurley 2002 and Zahn 1977,
! change use_other_tsync in the binary_controls
! section of inlist_project.

! Adapted for r15140

&binary_job

    inlist_names(1) = 'inlist1'
    inlist_names(2) = 'inlist2'

    evolve_both_stars = .true.

    warn_binary_extra=.false.

/ ! end of binary_job namelist

&binary_controls
    terminal_interval = 1000
    history_interval = 1
    write_header_frequency = 100
    do_tidal_sync = .true.
    do_j_accretion = .true.
    ! be 100% sure MB is always off
    do_jdot_mb = .false.
    do_jdot_missing_wind = .true.

    mdot_scheme = "Ritter"

    ! initial conditions specified in extra inlist
    m1 = 20.0d0 ! donor mass in Msun
    m2 = 15.0d0 ! companion mass in Msun
    initial_period_in_days = 12.0d0

    ! timestep controls
    fr = 0.01
    fr_limit = 2.5d-2
    fm = 0.01

```

```

fm_limit = 1d-1
varcontrol_case_a = 4d-4
varcontrol_case_b = 4d-4
varcontrol_ms = 1d-4
varcontrol_post_ms = 4d-4
dt_softening_factor = 0.4

limit_retention_by_mdot_edd = .false.
implicit_scheme_tolerance = 2.5d-4
max_tries_to_achieve = 100
min_change_factor = 1.02d0
max_change_factor = 1.2d0
initial_change_factor = 1.2d0
change_factor_fraction = 0.8d0
implicit_lambda = 0.4d0

sync_mode_1 = "Uniform"
sync_type_1 = "Hut_rad"
Ftid_1 = 1
sync_mode_2 = "Uniform"
sync_type_2 = "Hut_rad"
Ftid_2 = 1
! use_other_tsync will use the Zahn timescale as defined in run_binary_extras.f
!use_other_tsync = .true.
do_initial_orbit_sync_1 = .true.
do_initial_orbit_sync_2 = .true.

min_mdot_for_implicit = 1d-10
!allow a bit of space for contact
accretor_overflow_terminate = 0.05d0

/ ! end of binary_controls namelist

```

File 2: The inlist setting the controls for the primary.

```

! Modified inlist from:
! MESA VERSION: r7624
! Reproduces figure 8 of Paxton et al. 2015
! To use, make a local copy of $MESA_DIR/binary/work, copy the provided
! run_binary_extras.f (use the default run_star_extras.f),
! compile it (./clean && ./mk) and copy
! inlist1, inlist2 and inlist_project there.
! To switch between the tide form Hurley 2002 and Zahn 1977,
! change use_other_tsync in the binary_controls
! section of inlist_project.

! Changes made are based off of Choi et al. 2016

```

```
! For version r15140

&star_job

    show_log_description_at_start = .false.

    new_rotation_flag = .true.
    change_rotation_flag = .true.
    set_initial_surface_rotation_v = .true.
    ! this is just a random number, tidal sync takes care of it
    new_surface_rotation_v = 50

    save_model_when_terminate = .true.
    save_model_filename = "model1.dat"

    warn_run_star_extras = .false.

    !set reaction network
    change_net = .true.
    new_net_name = 'massive.net'

/ ! end of star_job namelist

&eos
    ! eos options
    ! see eos/defaults/eos.defaults

/ ! end of eos namelist

&kap
    ! kap options
    ! see kap/defaults/kap.defaults
    use_Type2_opacities = .true.
    Zbase = 1.2794982692730061d-3

    kap_file_prefix = 'a09'
    kap_lowT_prefix = 'lowT_fa05_a09p'
    kap_CO_prefix = 'a09_co'

/ ! end of kap namelist

&controls

    ! set the initial z
    initial_z = 1.2794982692730061d-3
```

```

zams_filename = 'z0.128m2_y25.092_alpha_fixedFe.data'

mesh_delta_coeff = 0.8
max_dq = 0.002
! min_dq_for_xa = 1d-5
max_allowed_nz = 40000

! convective premixing while on MS
do_conv_premix = .true.

redo_limit = -1

solver_iters_timestep_limit = 6

! max_model_number = 40000

! extra controls for timestep
! these are for changes in mdot
delta_mdot_atol = 1d-10
delta_mdot_rtol = 0.1
delta_mdot_limit = 1
! these are to properly resolve core hydrogen depletion
delta_lg_XH_cnr_limit = 0.02d0
delta_lg_XH_cnr_max = 0.0d0
delta_lg_XH_cnr_min = -6.0d0
delta_lg_XH_cnr_hard_limit = 0.03d0
! these are to properly resolve core helium depletion
delta_lg_XHe_cnr_limit = 0.02d0
delta_lg_XHe_cnr_max = 0.0d0
delta_lg_XHe_cnr_min = -6.0d0
delta_lg_XHe_cnr_hard_limit = 0.03d0
! these are to properly resolve core carbon depletion
delta_lg_XC_cnr_limit = 0.02d0
delta_lg_XC_cnr_max = 0.0d0
delta_lg_XC_cnr_min = -5.0d0
delta_lg_XC_cnr_hard_limit = 0.03d0
! this is mainly to resolve properly when the star goes off the main sequence
delta_HR_limit = 0.005d0

! increase resolution
mesh_logX_species(1) = 'h1'
mesh_logX_min_for_extra(1) = -6
mesh_dlogX_dlogP_extra(1) = 0.25

mesh_logX_species(2) = 'he4'
mesh_logX_min_for_extra(2) = -6
mesh_dlogX_dlogP_extra(2) = 0.25

```

```

mesh_logX_species(3) = 'c12'
mesh_logX_min_for_extra(3) = -6
mesh_dlogX_dlogP_extra(3) = 0.25

extra_terminal_output_file = 'log1'
photo_directory = 'photos1'
log_directory = 'LOGS1'

profile_interval = 20
history_interval = 1
terminal_interval = 50
write_header_frequency = 50
max_num_profile_models = 10000

! stop when the center mass fraction of h1 drops below this limit
xa_central_lower_limit_species(1) = 'c12'
xa_central_lower_limit(1) = 1d-6

use_ledoux_criterion = .true.
mixing_length_alpha = 1.82
alpha_semiconvection = 1d0
thermohaline_coeff = 1d0
remove_small_D_limit = 1d-10
mixing_D_limit_for_log = 1d-10

! rotational mixing coeffs
am_nu_ST_factor = -1 !1.0
D_visc_factor = 0.0
am_nu_SH_factor = -1 !0.0
D_ST_factor = 0.0
D_SH_factor = 1.0 !0.0
D_GSF_factor = 1.0
D_ES_factor = 1.0
D_SSI_factor = 1.0
D_DSI_factor = 1.0
am_D_mix_factor = 0.0333d0
am_gradmu_factor = 0.05d0
num_cells_for_smooth_gradL_composition_term = 2

! premix omega to avoid doing the newton with crazily shearing material
premix_omega = .true.

! wind options
hot_wind_scheme = 'Dutch' ! make sure you have hot winds!!
cool_wind_RGB_scheme = 'Dutch'
cool_wind_AGB_scheme = 'Dutch'
Dutch_wind_lowT_scheme = 'de Jager'
RGB_to_AGB_wind_switch = 1d-4

```



```
Dutch_scaling_factor = 1.0

! this is to avoid odd behaviour when a star switches from accreting to mass losing
max_mdot_jump_for_rotation = 1d99

! add for r15140
default_net_name = 'massive.net'

! add overshoot
overshoot_scheme(:) = 'exponential'

overshoot_zone_type(1) = 'any'
overshoot_zone_loc(1) = 'core'
overshoot_bdy_loc(1) = 'top'
overshoot_f(1) = 0.016
overshoot_f0(1) = 0.008

overshoot_zone_type(2) = 'any'
overshoot_zone_loc(2) = 'shell'
overshoot_bdy_loc(2) = 'any'
overshoot_f(2) = 0.0174
overshoot_f0(2) = 0.0087

/ ! end of controls namelist

&pgstar

/ ! end of pgstar namelist
```

File 3: The inlist setting the controls for the secondary.

```
! Modified inlist from:
! MESA VERSION: r7624
! Reproduces figure 8 of Paxton et al. 2015
! To use, make a local copy of $MESA_DIR/binary/work, copy the provided
! run_binary_extras.f (use the default run_star_extras.f),
! compile it (./clean && ./mk) and copy
! inlist1, inlist2 and inlist_project there.
! To switch between the tide form Hurley 2002 and Zahn 1977,
! change use_other_tsync in the binary_controls
! section of inlist_project.

! Changes made are based off of Choi et al. 2016
! For version r15140
```

```
&star_job

  show_log_description_at_start = .false.

  new_rotation_flag = .true.
  change_rotation_flag = .true.
  set_initial_surface_rotation_v = .true.
  ! this is just a random number, tidal sync takes care of it
  new_surface_rotation_v = 50

  save_model_when_terminate = .true.
  save_model_filename = "model2.dat"

  !set reaction network
  change_net = .true.
  new_net_name = 'massive.net'

  warn_run_star_extras = .false.

/ ! end of star_job namelist

&eos
  ! eos options
  ! see eos/defaults/eos.defaults

/ ! end of eos namelist

&kap
  ! kap options
  ! see kap/defaults/kap.defaults
  use_Type2_opacities = .true.
  Zbase = 1.2794982692730061d-3

  kap_file_prefix = 'a09'
  kap_lowT_prefix = 'lowT_fa05_a09p'
  kap_CO_prefix = 'a09_co'

/ ! end of kap namelist

&controls
  ! set the initial z
  initial_z = 1.2794982692730061d-3
  zams_filename = 'z0.128m2_y25.092_alpha_fixedFe.data'

  mesh_delta_coeff = 0.8
```

```

max_dq = 0.002
! min_dq_for_xa = 1d-5
max_allowed_nz = 40000

! convective premixing while on MS
do_conv_premix = .true.

redo_limit = -1

! smoothing for secondary
smooth_outer_xa_big = 0.05d0
smooth_outer_xa_small = 0.03d0

solver_iters_timestep_limit = 6

! max_model_number = 40000

! extra controls for timestep
! these are for changes in mdot
delta_mdot_atol = 1d-10
delta_mdot_rtol = 0.1
delta_mdot_limit = 1
! these are to properly resolve core hydrogen depletion
delta_lg_XH_cntr_limit = 0.02d0
delta_lg_XH_cntr_max = 0.0d0
delta_lg_XH_cntr_min = -6.0d0
delta_lg_XH_cntr_hard_limit = 0.03d0
! these are to properly resolve core helium depletion
delta_lg_XHe_cntr_limit = 0.02d0
delta_lg_XHe_cntr_max = 0.0d0
delta_lg_XHe_cntr_min = -6.0d0
delta_lg_XHe_cntr_hard_limit = 0.03d0
! these are to properly resolve core carbon depletion
delta_lg_XC_cntr_limit = 0.02d0
delta_lg_XC_cntr_max = 0.0d0
delta_lg_XC_cntr_min = -5.0d0
delta_lg_XC_cntr_hard_limit = 0.03d0
! this is mainly to resolve properly when the star goes off the main sequence
delta_HR_limit = 0.005d0

! increase resolution
mesh_logX_species(1) = 'h1'
mesh_logX_min_for_extra(1) = -6
mesh_dlogX_dlogP_extra(1) = 0.25

mesh_logX_species(2) = 'he4'
mesh_logX_min_for_extra(2) = -6
mesh_dlogX_dlogP_extra(2) = 0.25

```

```
mesh_logX_species(3) = 'c12'  
mesh_logX_min_for_extra(3) = -6  
mesh_dlogX_dlogP_extra(3) = 0.25  
  
extra_terminal_output_file = 'log2'  
photo_directory = 'photos2'  
log_directory = 'LOGS2'  
  
profile_interval = 20  
history_interval = 1  
terminal_interval = 50  
write_header_frequency = 50  
max_num_profile_models = 10000  
  
use_ledoux_criterion = .true.  
mixing_length_alpha = 1.82  
alpha_semiconvection = 1d0  
thermohaline_coeff = 1d0  
remove_small_D_limit = 1d-10  
mixing_D_limit_for_log = 1d-10  
  
! rotational mixing coeffs  
am_nu_ST_factor = -1 !1.0  
D_visc_factor = 0.0  
am_nu_SH_factor = -1 !0.0  
D_ST_factor = 0.0  
D_SH_factor = 1.0 !0.0  
D_GSF_factor = 1.0  
D_ES_factor = 1.0  
D_SSI_factor = 1.0  
D_DSI_factor = 1.0  
am_D_mix_factor = 0.0333d0  
am_gradmu_factor = 0.05d0  
num_cells_for_smooth_gradL_composition_term = 2  
  
! premix omega to avoid doing the newton with crazily shearing material  
premix_omega = .true.  
  
! wind options  
hot_wind_scheme = 'Dutch' ! make sure you have hot winds!!  
cool_wind_RGB_scheme = 'Dutch'  
cool_wind_AGB_scheme = 'Dutch'  
Dutch_wind_lowT_scheme = 'de Jager'  
RGB_to_AGB_wind_switch = 1d-4  
Dutch_scaling_factor = 1.0  
  
! controls for implicit wind
```

```

surf_avg_tau_min = 0
surf_avg_tau = 10
max_mdot_redo_cnt = 200
min_years_dt_for_redo_mdot = 0
surf_w_div_w_crit_limit = 0.99d0
surf_w_div_w_crit_tol = 0.06d0
rotational_mdot_boost_fac = 1d10
rotational_mdot_kh_fac = 1d10
mdot_revise_factor = 1.2
implicit_mdot_boost = 0.1

! this is to avoid odd behaviour when a star switches from accreting to mass losing
max_mdot_jump_for_rotation = 1d99

! add for r15140
default_net_name = 'massive.net'

! add overshoot
overshoot_scheme(:) = 'exponential'

overshoot_zone_type(1) = 'any'
overshoot_zone_loc(1) = 'core'
overshoot_bdy_loc(1) = 'top'
overshoot_f(1) = 0.016
overshoot_f0(1) = 0.008

overshoot_zone_type(2) = 'any'
overshoot_zone_loc(2) = 'shell'
overshoot_bdy_loc(2) = 'any'
overshoot_f(2) = 0.0174
overshoot_f0(2) = 0.0087

/ ! end of controls namelist

&pgstar

/ ! end of pgstar namelist

```

File 4: Source code used to set additional settings for the stars.

```

! *****
!
! Copyright (C) 2010-2019 Bill Paxton & The MESA Team
!
! this file is part of mesa.
!

```

```

!  mesa is free software; you can redistribute it and/or modify
!  it under the terms of the gnu general library public license as published
!  by the free software foundation; either version 2 of the license, or
!  (at your option) any later version.
!
!  mesa is distributed in the hope that it will be useful,
!  but without any warranty; without even the implied warranty of
!  merchantability or fitness for a particular purpose.  see the
!  gnu library general public license for more details.
!
!  you should have received a copy of the gnu library general public license
!  along with this software; if not, write to the free software
!  foundation, inc., 59 temple place, suite 330, boston, ma 02111-1307 usa
!
! *****
module run_star_extras

use star_lib
use star_def
use const_def
use math_lib

implicit none

real(dp) :: turn_off_premix = 0.0

! these routines are called by the standard run_star check_model
contains

    subroutine extras_controls(id, ierr)
integer, intent(in) :: id
integer, intent(out) :: ierr
type (star_info), pointer :: s
    ierr = 0
    call star_ptr(id, s, ierr)
    if (ierr /= 0) return

! this is the place to set any procedure pointers you want to change
! e.g., other_wind, other_mixing, other_energy (see star_data.inc)

! the extras functions in this file will not be called
! unless you set their function pointers as done below.
! otherwise we use a null_ version which does nothing (except warn).

s% extras_startup => extras_startup
s% extras_start_step => extras_start_step

```

```

!   s% extras_check_model => extras_check_model
!   s% extras_finish_step => extras_finish_step
!   s% extras_after_evolve => extras_after_evolve
!   s% how_many_extra_history_columns => how_many_extra_history_columns
!   s% data_for_extra_history_columns => data_for_extra_history_columns
!   s% how_many_extra_profile_columns => how_many_extra_profile_columns
!   s% data_for_extra_profile_columns => data_for_extra_profile_columns

!   s% how_many_extra_history_header_items => how_many_extra_history_header_items
!   s% data_for_extra_history_header_items => data_for_extra_history_header_items
!   s% how_many_extra_profile_header_items => how_many_extra_profile_header_items
!   s% data_for_extra_profile_header_items => data_for_extra_profile_header_items

end subroutine extras_controls

subroutine extras_startup(id, restart, ierr)
  integer, intent(in) :: id
  logical, intent(in) :: restart
  integer, intent(out) :: ierr
  type (star_info), pointer :: s
  ierr = 0
  call star_ptr(id, s, ierr)
  if (ierr /= 0) return

  ! increase varcontrol_target for higher mass stars
  if (s% star_mass >= 30.0) then
    if (s% star_mass == 40.0) then
      if (s% w_div_wcrit_max > 0) then
        s% varcontrol_target = 6d-4
        write(*,*) '+++++ varcontrol_target increased to 6d-4 +++++'
      else
        s% varcontrol_target = 5d-4
        write(*,*) '+++++ varcontrol_target increased to 5d-4 +++++'
      end if
    else
      s% varcontrol_target = 4d-4
      write(*,*) '+++++ varcontrol_target increased to 4d-4 +++++'
    end if
  end if
end subroutine extras_startup

integer function extras_start_step(id)
  integer, intent(in) :: id
  integer :: ierr
  type (star_info), pointer :: s
  ierr = 0

```

```
call star_ptr(id, s, ierr)
if (ierr /= 0) return
extras_start_step = 0

! once we reach core H exhaustion, turn of premixing
if ((s% center_h1 < 1d-4) .and. (turn_off_premix == 0.0)) then
  s% do_conv_premix = .false.
  write(*,*) 'reached core H exhaustion, turned off convective premixing'
  turn_off_premix = 1.0
end if
end function extras_start_step

! returns either keep_going, retry, or terminate.
integer function extras_check_model(id)
  integer, intent(in) :: id
  integer :: ierr
  type (star_info), pointer :: s
  ierr = 0
  call star_ptr(id, s, ierr)
  if (ierr /= 0) return
  extras_check_model = keep_going
  if (.false. .and. s% star_mass_h1 < 0.35d0) then
    ! stop when star hydrogen mass drops to specified level
    extras_check_model = terminate
    write(*, *) 'have reached desired hydrogen mass'
    return
  end if

! if you want to check multiple conditions, it can be useful
! to set a different termination code depending on which
! condition was triggered. MESA provides 9 customizable
! termination codes, named t_xtra1 .. t_xtra9. You can
! customize the messages that will be printed upon exit by
! setting the corresponding termination_code_str value.
! termination_code_str(t_xtra1) = 'my termination condition'

! by default, indicate where (in the code) MESA terminated
if (extras_check_model == terminate) s% termination_code = t_extras_check_model
end function extras_check_model

integer function how_many_extra_history_columns(id)
  integer, intent(in) :: id
  integer :: ierr
  type (star_info), pointer :: s
  ierr = 0
```



```

    call star_ptr(id, s, ierr)
    if (ierr /= 0) return
    how_many_extra_history_columns = 0
end function how_many_extra_history_columns

subroutine data_for_extra_history_columns(id, n, names, vals, ierr)
    integer, intent(in) :: id, n
    character (len=maxlen_history_column_name) :: names(n)
    real(dp) :: vals(n)
    integer, intent(out) :: ierr
    type (star_info), pointer :: s
    ierr = 0
    call star_ptr(id, s, ierr)
    if (ierr /= 0) return

    ! note: do NOT add the extras names to history_columns.list
    ! the history_columns.list is only for the built-in history column options.
    ! it must not include the new column names you are adding here.

end subroutine data_for_extra_history_columns

integer function how_many_extra_profile_columns(id)
    integer, intent(in) :: id
    integer :: ierr
    type (star_info), pointer :: s
    ierr = 0
    call star_ptr(id, s, ierr)
    if (ierr /= 0) return
    how_many_extra_profile_columns = 0
end function how_many_extra_profile_columns

subroutine data_for_extra_profile_columns(id, n, nz, names, vals, ierr)
    integer, intent(in) :: id, n, nz
    character (len=maxlen_profile_column_name) :: names(n)
    real(dp) :: vals(nz,n)
    integer, intent(out) :: ierr
    type (star_info), pointer :: s
    integer :: k
    ierr = 0
    call star_ptr(id, s, ierr)
    if (ierr /= 0) return

    ! note: do NOT add the extra names to profile_columns.list
    ! the profile_columns.list is only for the built-in profile column options.

```

```

        ! it must not include the new column names you are adding here.

        ! here is an example for adding a profile column
        !if (n /= 1) stop 'data_for_extra_profile_columns'
        !names(1) = 'beta'
        !do k = 1, nz
        !   vals(k,1) = s% Pgas(k)/s% P(k)
        !end do

end subroutine data_for_extra_profile_columns

integer function how_many_extra_history_header_items(id)
  integer, intent(in) :: id
  integer :: ierr
  type (star_info), pointer :: s
  ierr = 0
  call star_ptr(id, s, ierr)
  if (ierr /= 0) return
  how_many_extra_history_header_items = 0
end function how_many_extra_history_header_items

subroutine data_for_extra_history_header_items(id, n, names, vals, ierr)
  integer, intent(in) :: id, n
  character (len=maxlen_history_column_name) :: names(n)
  real(dp) :: vals(n)
  type(star_info), pointer :: s
  integer, intent(out) :: ierr
  ierr = 0
  call star_ptr(id,s,ierr)
  if(ierr/=0) return

  ! here is an example for adding an extra history header item
  ! also set how_many_extra_history_header_items
  ! names(1) = 'mixing_length_alpha'
  ! vals(1) = s% mixing_length_alpha

end subroutine data_for_extra_history_header_items

integer function how_many_extra_profile_header_items(id)
  integer, intent(in) :: id
  integer :: ierr
  type (star_info), pointer :: s
  ierr = 0
  call star_ptr(id, s, ierr)
  if (ierr /= 0) return

```

```

        how_many_extra_profile_header_items = 0
    end function how_many_extra_profile_header_items

subroutine data_for_extra_profile_header_items(id, n, names, vals, ierr)
    integer, intent(in) :: id, n
    character (len=maxlen_profile_column_name) :: names(n)
    real(dp) :: vals(n)
    type(star_info), pointer :: s
    integer, intent(out) :: ierr
    ierr = 0
    call star_ptr(id,s,ierr)
    if(ierr/=0) return

    ! here is an example for adding an extra profile header item
    ! also set how_many_extra_profile_header_items
    ! names(1) = 'mixing_length_alpha'
    ! vals(1) = s% mixing_length_alpha

end subroutine data_for_extra_profile_header_items

! returns either keep_going or terminate.
! note: cannot request retry; extras_check_model can do that.
integer function extras_finish_step(id)
    integer, intent(in) :: id
    integer :: ierr
    type (star_info), pointer :: s
    ierr = 0
    call star_ptr(id, s, ierr)
    if (ierr /= 0) return
    extras_finish_step = keep_going

    ! to save a profile,
    !   s% need_to_save_profiles_now = .true.
    ! to update the star log,
    !   s% need_to_update_history_now = .true.

    ! see extras_check_model for information about custom termination codes
    ! by default, indicate where (in the code) MESA terminated
    if (extras_finish_step == terminate) s% termination_code = t_extras_finish_step
end function extras_finish_step

subroutine extras_after_evolve(id, ierr)
    integer, intent(in) :: id
    integer, intent(out) :: ierr
    type (star_info), pointer :: s

```

```

        ierr = 0
        call star_ptr(id, s, ierr)
        if (ierr /= 0) return
    end subroutine extras_after_evolve

end module run_star_extras

```

File 5: Source code to calculate additional values for the binaries.

```

! *****
!
!   Copyright (C) 2012  Bill Paxton
!
!   this file is part of mesa.
!
!   mesa is free software; you can redistribute it and/or modify
!   it under the terms of the gnu general library public license as published
!   by the free software foundation; either version 2 of the license, or
!   (at your option) any later version.
!
!   mesa is distributed in the hope that it will be useful,
!   but without any warranty; without even the implied warranty of
!   merchantability or fitness for a particular purpose.  see the
!   gnu library general public license for more details.
!
!   you should have received a copy of the gnu library general public license
!   along with this software; if not, write to the free software
!   foundation, inc., 59 temple place, suite 330, boston, ma 02111-1307 usa
!
! *****
!added isotope abundances
  module run_binary_extras

    use star_lib
    use star_def
    use const_def
    use math_lib
    use binary_def

    use chem_def
    use chem_lib

    implicit none

    integer, parameter :: n_isotopes = 50
    character (len=solnamelen) :: mdot_isotopes(n_isotopes)

```

contains

subroutine init_mdot_iso

```
mdot_isotopes = (/ &
'h1 ', 'h2 ', 'he3 ', 'he4 ', 'li6 ', 'li7 ', 'be7 ', 'be9 ', 'be10 ', &
'b8 ', 'b10 ', 'b11 ', 'c12 ', 'c13 ', 'n13 ', 'n14 ', 'n15 ', 'o14 ', &
'o15 ', 'o16 ', 'o17 ', 'o18 ', 'f17 ', 'f18 ', 'f19 ', 'na21 ', 'na22 ', &
'na23 ', 'na24 ', 'mg22 ', 'mg23 ', 'mg24 ', 'mg25 ', 'mg26 ', 'al25 ', 'al26 ', &
'al27 ', 'si27 ', 'si28 ', 'si29 ', 'si30 ', 'ca40 ', 'ti44 ', 'ti48 ', 'ni56 ', &
'cr48 ', 'cr56 ', 'fe52 ', 'fe54 ', 'fe56 ' /)
```

end subroutine init_mdot_iso

subroutine extras_binary_controls(binary_id, ierr)

```
integer :: binary_id
integer, intent(out) :: ierr
type (binary_info), pointer :: b
ierr = 0
```

```
call binary_ptr(binary_id, b, ierr)
```

```
if (ierr /= 0) then
  write(*,*) 'failed in binary_ptr'
  return
end if
```

```
end if
```

```
b% other_tsync => my_tsync
```

```
! Set these function pointers to point to the functions you wish to use in
! your run_binary_extras. Any which are not set, default to a null_ version
! which does nothing.
```

```
b% how_many_extra_binary_history_header_items => &
```

```
  how_many_extra_binary_history_header_items
```

```
b% data_for_extra_binary_history_header_items => &
```

```
  data_for_extra_binary_history_header_items
```

```
b% how_many_extra_binary_history_columns => &
```

```
  how_many_extra_binary_history_columns
```

```
b% data_for_extra_binary_history_columns => &
```

```
  data_for_extra_binary_history_columns
```

```
b% extras_binary_startup=> extras_binary_startup
```

```
b% extras_binary_start_step=> extras_binary_start_step
```

```
b% extras_binary_check_model=> extras_binary_check_model
```

```
b% extras_binary_finish_step => extras_binary_finish_step
```

```
b% extras_binary_after_evolve=> extras_binary_after_evolve
```

```
! Once you have set the function pointers you want,
! then uncomment this (or set it in your star_job inlist)
! to disable the printed warning message,
```

```
b% warn_binary_extra =.false.
```

```

end subroutine extras_binary_controls

subroutine my_tsync(id, sync_type, Ftid, qratio, m, r_phot, osep, t_sync, ierr)
  integer, intent(in) :: id
  character (len=strlen), intent(in) :: sync_type ! synchronization timescale
  real(dp), intent(in) :: Ftid ! efficiency of tidal synchronization.
  ! (time scale / Ftid ).
  real(dp), intent(in) :: qratio ! mass_other_star/mass_this_star
  real(dp), intent(in) :: m
  real(dp), intent(in) :: r_phot
  real(dp), intent(in) :: osep ! orbital separation (cm)
  real(dp), intent(out) :: t_sync
  integer, intent(out) :: ierr
  real(dp) :: rGyr_squared, moment_of_inertia
  type (binary_info), pointer :: b
  type (star_info), pointer :: s

  ierr = 0
  call star_ptr(id, s, ierr)
  if (ierr /= 0) then
    write(*,*) 'failed in star_ptr'
    return
  end if

  call binary_ptr(s% binary_id, b, ierr)
  if (ierr /= 0) then
    write(*,*) 'failed in binary_ptr'
    return
  end if
  t_sync = 1/(qratio*qratio)*pow6(osep/r_phot)*secyer
end subroutine my_tsync

integer function how_many_extra_binary_history_header_items(binary_id)
  use binary_def, only: binary_info
  integer, intent(in) :: binary_id
  how_many_extra_binary_history_header_items = 0
end function how_many_extra_binary_history_header_items

integer function how_many_extra_binary_history_columns(binary_id)
  use binary_def, only: binary_info
  integer, intent(in) :: binary_id
  ! set number of extra columns
  how_many_extra_binary_history_columns = n_isotopes + 5
end function how_many_extra_binary_history_columns

subroutine data_for_extra_binary_history_header_items( &
  binary_id, n, names, vals, ierr)

```

```

type (binary_info), pointer :: b
integer, intent(in) :: binary_id, n
character (len=maxlen_binary_history_column_name) :: names(n)
real(dp) :: vals(n)
integer, intent(out) :: ierr
ierr = 0
call binary_ptr(binary_id, b, ierr)
if (ierr /= 0) then
    write(*,*) 'failed in binary_ptr'
    return
end if
end subroutine data_for_extra_binary_history_header_items

subroutine data_for_extra_binary_history_columns(binary_id, n, names, vals, ierr)
use const_def, only: dp
type (binary_info), pointer :: b
integer, intent(in) :: binary_id
integer, intent(in) :: n
character (len=maxlen_binary_history_column_name) :: names(n)
real(dp) :: vals(n)
real(dp) :: vrot1, vrot2, wcrit1, wcrit2
integer, intent(out) :: ierr
real(dp) :: beta

! adding required values
integer :: i, j, k
real(dp) :: val

! isotopes to calculate mdot system for
call init_mdot_iso

ierr = 0
call binary_ptr(binary_id, b, ierr)
if (ierr /= 0) then
    write(*,*) 'failed in binary_ptr'
    return
end if

!w/w_crit stuff
wcrit1 = b% s_donor% w_div_w_crit_roche(1)
wcrit2 = b% s_accretor% w_div_w_crit_roche(1)

vrot1 = b% s_donor% v_rot_avg_surf / 1.0e+5
vrot2 = b% s_accretor% v_rot_avg_surf / 1.0e+5

names(1) = "v_rot_1"
vals(1) = vrot1
names(2) = "v_rot_2"

```

```
vals(2) = vrot2
names(3) = "w_crit_1"
vals(3) = wcrit1
names(4) = "w_crit_2"
vals(4) = wcrit2

! copied from ver 10000 with updates,
! evaluating log mdot for different isotopes
! writing names
do j=1,n_isotopes
  i = get_nuclide_index(mdot_isotopes(j))
  names(j+4) = 'mdot_system_' // trim(mdot_isotopes(j))

  ! evaluate
  k = b% s_donor% net_iso(i)
  val = 0
  if (k > 0) then
    if (b% s_donor% mstar_dot < 0) then
      val = b% s_donor% xa_removed(k) * b% s_donor% mstar_dot
    end if
  end if
  if (b% point_mass_i == 0) then
    if (b% s_accretor% mstar_dot > 0) then
      if (k > 0) &
        val = val + b% s_donor% xa_removed(k) * b% s_accretor% mstar_dot
    else
      k = b% s_accretor% net_iso(i)
      if (k > 0) &
        val = val + b% s_accretor% xa_removed(k) * b% s_accretor% mstar_dot
    end if
  else
    val = val - b% mtransfer_rate * b% fixed_xfer_fraction
  end if
  val = -val / Msun * secyer

  ! write out
  vals(j+4) = val
end do

! evaluate system log_mdot
val = b% s_donor% mstar_dot

if (b% point_mass_i == 0) then
  val = val + b% s_accretor% mstar_dot
end if
val = -val / Msun * secyer

vals(n_isotopes + 5) = val
```



```

names(n_isotopes + 5) = 'mdot_system_total'
end subroutine data_for_extra_binary_history_columns

integer function extras_binary_startup(binary_id,restart,ierr)
  type (binary_info), pointer :: b
  integer, intent(in) :: binary_id
  integer, intent(out) :: ierr
  logical, intent(in) :: restart
  call binary_ptr(binary_id, b, ierr)
  if (ierr /= 0) then ! failure in binary_ptr
    return
  end if

!       b% s1% job% warn_run_star_extras = .false.
  extras_binary_startup = keep_going
end function extras_binary_startup

integer function extras_binary_start_step(binary_id,ierr)
  type (binary_info), pointer :: b
  integer, intent(in) :: binary_id
  integer, intent(out) :: ierr

  extras_binary_start_step = keep_going
  call binary_ptr(binary_id, b, ierr)
  if (ierr /= 0) then ! failure in binary_ptr
    return
  end if

end function extras_binary_start_step

!Return either rety,backup,keep_going or terminate
integer function extras_binary_check_model(binary_id)
  type (binary_info), pointer :: b
  integer, intent(in) :: binary_id
  integer :: ierr
  call binary_ptr(binary_id, b, ierr)
  if (ierr /= 0) then ! failure in binary_ptr
    return
  end if
  extras_binary_check_model = keep_going

end function extras_binary_check_model

! returns either keep_going or terminate.
! note: cannot request retry or backup; extras_check_model can do that.
integer function extras_binary_finish_step(binary_id)
  type (binary_info), pointer :: b

```

```
integer, intent(in) :: binary_id
integer :: ierr
call binary_ptr(binary_id, b, ierr)
if (ierr /= 0) then ! failure in binary_ptr
    return
end if
extras_binary_finish_step = keep_going

end function extras_binary_finish_step

subroutine extras_binary_after_evolve(binary_id, ierr)
type (binary_info), pointer :: b
integer, intent(in) :: binary_id
integer, intent(out) :: ierr
call binary_ptr(binary_id, b, ierr)
if (ierr /= 0) then ! failure in binary_ptr
    return
end if

end subroutine extras_binary_after_evolve
end module run_binary_extras
```

Appendix B

Tables of runs

Here we provide tables on the alpha-enhanced (table B.1) and the solar-scaled (table B.2) binaries. We list the initial parameters, M_1 , M_2 , P . The “Changed” column indicates which `varcontrol` setting was modified (‘-’ if none were). The “Best” column provides the best setting found for that changed setting, with ‘default’ referring to the base settings. We also list the stopping or exclusion condition reached by the binaries. In notes, we highlight some runs that had issues: ‘vc’ indicates instability with different `varcontrol` settings, ‘ts’ indicates runs that had small timesteps and may benefit from longer runtimes, ‘s’ indicates the secondary evolution was unstable. Additional changes to `varcontrol`, or possibly timestep and resolution settings may be helpful for these runs in particular.

M_1 (M_\odot)	M_2 (M_\odot)	P (days)	Changed	Best	Condition	Notes
10	7.5	1.87	-	default	none	
10	7.5	7.47	case	default	mdot	
10	7.5	29.86	case	default	no eject	

Continued on the next page

Continued from previous page

M_1 (M_\odot)	M_2 (M_\odot)	P (days)	Changed	Best	Condition	Notes
10	7.5	119.34	case	default	no eject	
10	7.5	476.89	post_ms	5d-4	mdot	vc
10	7.5	1905.73	post_ms	5d-4	no overflow	
10	9	1.87	case	default	none	vc
10	9	7.47	case	default	mdot	
10	9	29.86	case	default	mdot	
10	9	119.34	case	default	no eject	ts
10	9	476.89	post_ms	3d-4	mdot	vc
10	9	1905.73	post_ms	default	no overflow	
12	5.4	1.95	case	default	none	vc
12	5.4	8.37	case	default	no eject	vc, ts, s
12	5.4	35.92	case	default	no eject	ts, s
12	5.4	154.16	case	default	carbon	s
12	5.4	661.65	case	3d-4	mdot	
12	5.4	2839.73	post_ms	5d-4	no overflow	
12	7.2	1.95	case	3d-4	none	vc
12	7.2	8.37	case	default	mdot	
12	7.2	35.92	-	default	mdot	
12	7.2	154.16	case	3d-4	carbon	
12	7.2	661.65	case	default	mdot	
12	7.2	2839.73	post_ms	default	no overflow	

Continued on the next page

Continued from previous page

M_1 (M_\odot)	M_2 (M_\odot)	P (days)	Changed	Best	Condition	Notes
12	9	1.95	case	default	none	vc
12	9	8.37	case	5d-4	none	s
12	9	35.92	-	default	carbon	
12	9	154.16	case	3d-4	carbon	
12	9	661.65	case	3d-4	carbon	
12	9	2839.73	post_ms	default	no overflow	
12	10.8	1.95	case	5d-4	none	vc
12	10.8	8.37	case	3d-4	mdot	vc
12	10.8	35.92	case	default	carbon	
12	10.8	154.16	case	3d-4	carbon	
12	10.8	661.65	-	default	carbon	
12	10.8	2839.73	post_ms	default	no overflow	
15	4.5	2.11	case	3d-4	mdot	
15	4.5	5.32	case	3d-4	no eject	ts
15	4.5	13.42	case	3d-4	mdot	
15	4.5	33.84	case	default	mdot	
15	4.5	85.33	case	default	mdot	
15	4.5	215.18	case	5d-4	carbon	
15	6.75	2.11	case	default	mdot	
15	6.75	5.32	case	default	no eject	
15	6.75	13.42	case	default	mdot	

Continued on the next page

Continued from previous page

M_1 (M_\odot)	M_2 (M_\odot)	P (days)	Changed	Best	Condition	Notes
15	6.75	33.84	case	5d-4	mdot	
15	6.75	85.33	-	default	carbon	
15	6.75	215.18	-	default	carbon	
15	9	2.11	case	default	contact	vc
15	9	5.32	case	default	contact	
15	9	13.42	-	default	carbon	
15	9	33.84	-	default	carbon	
15	9	85.33	-	default	carbon	
15	9	215.18	-	default	mdot	
15	11.25	2.11	case	default	none	vc
15	11.25	5.32	case	default	contact	
15	11.25	13.42	-	default	mdot	
15	11.25	33.84	-	default	mdot	
15	11.25	85.33	-	default	carbon	
15	11.25	215.18	-	default	carbon	
15	13.5	2.11	-	default	none	
15	13.5	5.32	-	default	carbon	
15	13.5	13.42	case	default	carbon	
15	13.5	33.84	case	default	mdot	
15	13.5	85.33	-	default	mdot	
15	13.5	215.18	-	default	carbon	

Continued on the next page

Continued from previous page

M_1 (M_\odot)	M_2 (M_\odot)	P (days)	Changed	Best	Condition	Notes
20	6	2.49	case	default	mdot	
20	6	4.36	case	default	mdot	
20	6	7.65	-	default	none	
20	6	13.4	case	default	mdot	vc
20	6	23.49	case	default	mdot	
20	6	41.17	case	default	mdot	
20	9	2.49	case	default	mdot	vc
20	9	4.36	case	3d-4	contact	
20	9	7.65	case	3d-4	contact	vc
20	9	13.4	-	default	none	
20	9	23.49	-	default	carbon	
20	9	41.17	-	default	carbon	
20	12	2.49	case	default	mdot	vc
20	12	4.36	case	default	none	vc
20	12	7.65	-	default	none	
20	12	13.4	-	default	mdot	
20	12	23.49	-	default	mdot	
20	12	41.17	case	default	mdot	
20	15	2.49	case	default	none	vc
20	15	4.36	case	default	contact	
20	15	7.65	-	default	mdot	

Continued on the next page

Continued from previous page

M_1 (M_\odot)	M_2 (M_\odot)	P (days)	Changed	Best	Condition	Notes
20	15	13.4	-	default	carbon	
20	15	23.49	-	default	mdot	
20	15	41.17	-	default	carbon	
20	18	2.49	-	default	none	
20	18	4.36	-	default	none	
20	18	7.65	-	default	carbon	
20	18	13.4	-	default	carbon	
20	18	23.49	case	default	carbon	
20	18	41.17	-	default	mdot	
25	3.75	2.42	case	default	contact	vc
25	3.75	4.03	-	default	none	
25	3.75	6.7	-	default	none	
25	3.75	11.14	case	default	mdot	vc
25	3.75	18.54	case	default	mdot	
25	3.75	30.84	case	default	mdot	
25	7.5	2.42	case	default	mdot	vc
25	7.5	4.03	case	3d-4	none	s
25	7.5	6.7	case	default	none	
25	7.5	11.14	case	default	mdot	vc
25	7.5	18.54	case	default	mdot	
25	7.5	30.84	case	default	mdot	

Continued on the next page

Continued from previous page

M_1 (M_\odot)	M_2 (M_\odot)	P (days)	Changed	Best	Condition	Notes
25	11.25	2.42	case	default	mdot	vc
25	11.25	4.03	case	default	contact	vc
25	11.25	6.7	case	default	mdot	vc
25	11.25	11.14	case	default	contact	
25	11.25	18.54	-	default	none	
25	11.25	30.84	-	default	carbon	
25	15	2.42	case	default	none	s
25	15	4.03	case	default	contact	
25	15	6.7	case	default	contact	
25	15	11.14	-	default	none	
25	15	18.54	-	default	none	
25	15	30.84	-	default	carbon	
25	18.75	2.42	case	default	none	vc
25	18.75	4.03	case	3d-4	contact	vc
25	18.75	6.7	-	default	none	
25	18.75	11.14	case	5d-4	none	
25	18.75	18.54	-	default	carbon	
25	18.75	30.84	case	default	none	
25	22.5	2.42	case	default	contact	
25	22.5	4.03	-	default	contact	
25	22.5	6.7	-	default	none	

Continued on the next page

Continued from previous page

M_1 (M_\odot)	M_2 (M_\odot)	P (days)	Changed	Best	Condition	Notes
25	22.5	11.14	-	default	none	
25	22.5	18.54	case	default	none	
25	22.5	30.84	case	3d-4	mdot	
30	4.5	2.49	case	5d-4	mdot	
30	4.5	3.49	case	default	mdot	
30	4.5	4.88	case	default	none	
30	4.5	6.83	case	5d-4	mdot	
30	4.5	9.57	case	default	none	
30	4.5	13.4	case	3d-4	mdot	
30	9	2.49	case	default	mdot	
30	9	3.49	case	default	contact	
30	9	4.88	case	default	mdot	
30	9	6.83	case	default	mdot	
30	9	9.57	case	default	none	
30	9	13.4	case	default	mdot	vc
30	13.5	2.49	case	5d-4	contact	vc
30	13.5	3.49	case	3d-4	mdot	vc
30	13.5	4.88	case	default	mdot	vc
30	13.5	6.83	case	default	mdot	
30	13.5	9.57	case	default	none	
30	13.5	13.4	-	default	none	

Continued on the next page

Continued from previous page

M_1 (M_\odot)	M_2 (M_\odot)	P (days)	Changed	Best	Condition	Notes
30	18	2.49	case	5d-4	contact	
30	18	3.49	case	5d-4	contact	
30	18	4.88	case	default	contact	vc
30	18	6.83	-	default	contact	
30	18	9.57	-	default	none	
30	18	13.4	-	default	none	
30	22.5	2.49	-	default	contact	
30	22.5	3.49	-	default	contact	
30	22.5	4.88	-	default	none	
30	22.5	6.83	-	default	none	
30	22.5	9.57	case	default	none	
30	22.5	13.4	case	default	none	
30	27	2.49	case	default	contact	
30	27	3.49	case	default	contact	vc
30	27	4.88	-	default	none	
30	27	6.83	-	default	none	
30	27	9.57	-	default	none	
30	27	13.4	case	5d-4	mdot	
40	6	3.02	case	5d-4	mdot	
40	6	4.12	case	5d-4	mdot	
40	6	5.62	ms	4d-4	none	

Continued on the next page

Continued from previous page

M_1 (M_\odot)	M_2 (M_\odot)	P (days)	Changed	Best	Condition	Notes
40	6	7.67	case	default	none	
40	6	10.47	case	default	none	
40	6	14.29	ms	2d-4	none	
40	12	3.02	case	5d-4	contact	
40	12	4.12	case	default	contact	vc
40	12	5.62	case	default	mdot	
40	12	7.67	ms	2d-4	mdot	
40	12	10.47	case	default	mdot	vc
40	12	14.29	case	3d-4	mdot	
40	18	3.02	case	5d-4	contact	
40	18	4.12	case	default	contact	
40	18	5.62	ms	2d-4	mdot	
40	18	7.67	case	default	contact	vc
40	18	10.47	case	default	mdot	
40	18	14.29	-	default	none	
40	24	3.02	-	default	contact	
40	24	4.12	case	5d-4	contact	vc
40	24	5.62	-	default	contact	
40	24	7.67	ms	2d-4	none	
40	24	10.47	ms	4d-4	none	
40	24	14.29	ms	2d-4	none	

Continued on the next page

Continued from previous page

$M_1 (M_\odot)$	$M_2 (M_\odot)$	P (days)	Changed	Best	Condition	Notes
40	30	3.02	case	default	none	vc
40	30	4.12	-	default	none	
40	30	5.62	-	default	none	
40	30	7.67	-	default	none	
40	30	10.47	ms	2d-4	none	
40	30	14.29	case	default	mdot	
40	36	3.02	case	default	contact	
40	36	4.12	case	default	contact	
40	36	5.62	-	default	none	
40	36	7.67	-	default	none	
40	36	10.47	ms	default	no overflow	
40	36	14.29	case	3d-4	mdot	

Table B.1: List of the alpha-enhanced binaries

$M_1 (M_\odot)$	$M_2 (M_\odot)$	P (days)	Changed	Best	Condition	Notes
10	7.5	1.87	case	default	none	
10	7.5	7.47	case	default	mdot	
10	7.5	29.86	case	default	mdot	
10	7.5	119.34	case	default	mdot	

Continued on the next page

Continued from previous page

M_1 (M_\odot)	M_2 (M_\odot)	P (days)	Changed	Best	Condition	Notes
10	7.5	476.89	case	3d-4	carbon	
10	7.5	1905.73	post_ms	3d-4	no overflow	
10	9	1.87	case	default	none	
10	9	7.47	case	3d-4	mdot	
10	9	29.86	case	5d-4	mdot	
10	9	119.34	-	default	carbon	
10	9	476.89	case	3d-4	carbon	
10	9	1905.73	post_ms	5d-4	no overflow	
12	5.4	1.95	case	3d-4	mdot	
12	5.4	8.37	case	default	mdot	
12	5.4	35.92	case	5d-4	carbon	
12	5.4	154.16	case	default	no eject	
12	5.4	661.65	post_ms	default	no overflow	ts
12	5.4	2839.73	post_ms	5d-4	no overflow	
12	7.2	1.95	case	default	none	
12	7.2	8.37	case	default	mdot	
12	7.2	35.92	-	default	carbon	
12	7.2	154.16	-	default	no eject	
12	7.2	661.65	post_ms	5d-4	mdot	
12	7.2	2839.73	post_ms	default	no overflow	
12	9	1.95	case	default	none	

Continued on the next page

Continued from previous page

$M_1 (M_\odot)$	$M_2 (M_\odot)$	P (days)	Changed	Best	Condition	Notes
12	9	8.37	case	5d-4	mdot	
12	9	35.92	case	default	mdot	
12	9	154.16	case	default	no eject	
12	9	661.65	post_ms	default	no overflow	
12	9	2839.73	post_ms	3d-4	no overflow	
12	10.8	1.95	case	3d-4	none	
12	10.8	8.37	case	default	mdot	
12	10.8	35.92	case	default	mdot	
12	10.8	154.16	case	default	carbon	
12	10.8	661.65	case	default	mdot	
12	10.8	2839.73	post_ms	default	no overflow	
15	4.5	2.11	case	default	mdot	
15	4.5	5.32	case	default	no eject	
15	4.5	13.42	case	default	mdot	
15	4.5	33.84	case	default	mdot	
15	4.5	85.33	case	default	mdot	
15	4.5	215.18	case	default	none	
15	6.75	2.11	case	5d-4	contact	
15	6.75	5.32	case	3d-4	contact	
15	6.75	13.42	case	default	carbon	
15	6.75	33.84	case	default	carbon	

Continued on the next page

Continued from previous page

M₁ (M_⊙)	M₂ (M_⊙)	P (days)	Changed	Best	Condition	Notes
15	6.75	85.33	case	3d-4	carbon	
15	6.75	215.18	case	default	mdot	
15	9	2.11	case	default	none	
15	9	5.32	case	default	contact	
15	9	13.42	case	5d-4	carbon	
15	9	33.84	case	5d-4	carbon	
15	9	85.33	-	default	carbon	
15	9	215.18	case	default	carbon	
15	11.25	2.11	case	5d-4	contact	
15	11.25	5.32	case	default	contact	
15	11.25	13.42	case	default	carbon	
15	11.25	33.84	-	default	carbon	
15	11.25	85.33	case	5d-4	carbon	
15	11.25	215.18	case	default	carbon	
15	13.5	2.11	case	default	contact	
15	13.5	5.32	case	default	mdot	
15	13.5	13.42	case	default	carbon	
15	13.5	33.84	case	default	mdot	
15	13.5	85.33	case	default	mdot	
15	13.5	215.18	-	default	carbon	
20	6	2.49	case	5d-4	contact	

Continued on the next page

Continued from previous page

M_1 (M_\odot)	M_2 (M_\odot)	P (days)	Changed	Best	Condition	Notes
20	6	4.36	case	3d-4	none	
20	6	7.65	case	3d-4	mdot	
20	6	13.4	case	default	mdot	
20	6	23.49	case	default	mdot	
20	6	41.17	case	default	mdot	
20	9	2.49	case	5d-4	contact	
20	9	4.36	case	default	mdot	
20	9	7.65	case	3d-4	mdot	
20	9	13.4	case	default	carbon	
20	9	23.49	-	default	carbon	
20	9	41.17	-	default	carbon	
20	12	2.49	case	default	mdot	
20	12	4.36	case	default	contact	
20	12	7.65	case	default	mdot	
20	12	13.4	-	default	carbon	
20	12	23.49	-	default	carbon	
20	12	41.17	-	default	carbon	
20	15	2.49	case	5d-4	contact	
20	15	4.36	case	default	none	
20	15	7.65	case	default	mdot	
20	15	13.4	case	default	none	

Continued on the next page

Continued from previous page

M_1 (M_\odot)	M_2 (M_\odot)	P (days)	Changed	Best	Condition	Notes
20	15	23.49	-	default	carbon	
20	15	41.17	-	default	carbon	
20	18	2.49	case	default	contact	
20	18	4.36	-	default	carbon	
20	18	7.65	-	default	carbon	
20	18	13.4	-	default	carbon	
20	18	23.49	case	default	carbon	
20	18	41.17	case	5d-4	none	
25	3.75	2.42	case	3d-4	contact	
25	3.75	4.03	case	default	none	
25	3.75	6.7	case	default	none	
25	3.75	11.14	case	default	mdot	
25	3.75	18.54	case	default	mdot	
25	3.75	30.84	case	default	mdot	
25	7.5	2.42	case	3d-4	mdot	
25	7.5	4.03	case	default	mdot	
25	7.5	6.7	case	default	mdot	
25	7.5	11.14	case	default	mdot	
25	7.5	18.54	case	default	mdot	
25	7.5	30.84	case	default	mdot	
25	11.25	2.42	case	5d-4	contact	

Continued on the next page

Continued from previous page

M₁ (M_⊙)	M₂ (M_⊙)	P (days)	Changed	Best	Condition	Notes
25	11.25	4.03	case	3d-4	mdot	
25	11.25	6.7	case	default	none	
25	11.25	11.14	case	5d-4	none	
25	11.25	18.54	-	default	carbon	
25	11.25	30.84	-	default	carbon	
25	15	2.42	case	5d-4	contact	
25	15	4.03	case	default	mdot	
25	15	6.7	case	5d-4	none	
25	15	11.14	case	default	none	
25	15	18.54	case	default	mdot	
25	15	30.84	case	default	carbon	
25	18.75	2.42	case	default	contact	
25	18.75	4.03	-	default	none	
25	18.75	6.7	-	default	none	
25	18.75	11.14	-	default	carbon	
25	18.75	18.54	case	default	mdot	
25	18.75	30.84	-	default	carbon	
25	22.5	2.42	-	default	contact	
25	22.5	4.03	-	default	none	
25	22.5	6.7	-	default	none	
25	22.5	11.14	case	default	mdot	

Continued on the next page

Continued from previous page

M₁ (M_⊙)	M₂ (M_⊙)	P (days)	Changed	Best	Condition	Notes
25	22.5	18.54	-	default	carbon	
25	22.5	30.84	case	3d-4	none	
30	4.5	2.49	case	5d-4	mdot	
30	4.5	3.49	case	default	none	
30	4.5	4.88	case	default	none	ts
30	4.5	6.83	case	default	none	ts
30	4.5	9.57	case	default	mdot	
30	4.5	13.4	case	default	mdot	
30	9	2.49	case	5d-4	mdot	
30	9	3.49	case	5d-4	mdot	
30	9	4.88	case	5d-4	mdot	
30	9	6.83	case	default	mdot	
30	9	9.57	case	default	mdot	
30	9	13.4	case	5d-4	mdot	
30	13.5	2.49	case	5d-4	contact	
30	13.5	3.49	case	default	mdot	
30	13.5	4.88	case	default	mdot	
30	13.5	6.83	case	default	mdot	
30	13.5	9.57	case	default	mdot	
30	13.5	13.4	case	5d-4	none	
30	18	2.49	case	5d-4	contact	

Continued on the next page

Continued from previous page

M_1 (M_\odot)	M_2 (M_\odot)	P (days)	Changed	Best	Condition	Notes
30	18	3.49	case	default	no overflow	
30	18	4.88	case	default	mdot	
30	18	6.83	case	default	none	
30	18	9.57	case	default	none	
30	18	13.4	case	3d-4	none	
30	22.5	2.49	case	5d-4	contact	
30	22.5	3.49	case	default	contact	
30	22.5	4.88	case	5d-4	none	
30	22.5	6.83	case	5d-4	none	
30	22.5	9.57	case	default	none	
30	22.5	13.4	case	default	carbon	
30	27	2.49	case	default	contact	
30	27	3.49	case	default	none	
30	27	4.88	case	5d-4	none	
30	27	6.83	case	5d-4	mdot	
30	27	9.57	case	default	none	
30	27	13.4	case	3d-4	none	
40	6	3.02	case	default	contact	
40	6	4.12	case	default	none	vc
40	6	5.62	case	3d-4	mdot	
40	6	7.67	post_ms	default	no overflow	vc

Continued on the next page

Continued from previous page

$M_1 (M_\odot)$	$M_2 (M_\odot)$	P (days)	Changed	Best	Condition	Notes
40	6	10.47	post_ms	default	no overflow	vc
40	6	14.29	post_ms	default	no overflow	vc
40	12	3.02	case	5d-4	contact	
40	12	4.12	case	3d-4	contact	
40	12	5.62	case	default	mdot	
40	12	7.67	ms	2d-4	none	vc
40	12	10.47	ms	2d-4	none	vc
40	12	14.29	post_ms	default	no overflow	vc
40	18	3.02	case	5d-4	mdot	
40	18	4.12	case	3d-4	contact	
40	18	5.62	case	default	mdot	
40	18	7.67	post_ms	default	no overflow	vc
40	18	10.47	ms	2d-4	none	vc
40	18	14.29	ms	2d-4	none	vc
40	24	3.02	case	5d-4	contact	
40	24	4.12	case	5d-4	none	
40	24	5.62	case	5d-4	none	
40	24	7.67	post_ms	default	no overflow	vc
40	24	10.47	post_ms	default	no overflow	vc
40	24	14.29	case	3d-4	none	
40	30	3.02	post_ms	default	contact	

Continued on the next page

Continued from previous page

$M_1 (M_\odot)$	$M_2 (M_\odot)$	P (days)	Changed	Best	Condition	Notes
40	30	4.12	post_ms	3d-4	none	vc
40	30	5.62	ms	2d-4	none	vc
40	30	7.67	post_ms	default	no overflow	vc
40	30	10.47	post_ms	default	no overflow	vc
40	30	14.29	post_ms	default	mdot	
40	36	3.02	case	default	contact	
40	36	4.12	case	default	contact	
40	36	5.62	post_ms	5d-4	none	ts
40	36	7.67	case	default	none	
40	36	10.47	post_ms	default	mdot	
40	36	14.29	post_ms	default	no overflow	vc

Table B.2: List of the solar-scaled binaries.

Appendix C

Probabilities over the interpolated parameter space

For reference, we provide slices of the interpolation space in figure C.1. The parameter space excludes low mass ratios for low-mass primaries and excludes high periods for high-mass primaries.

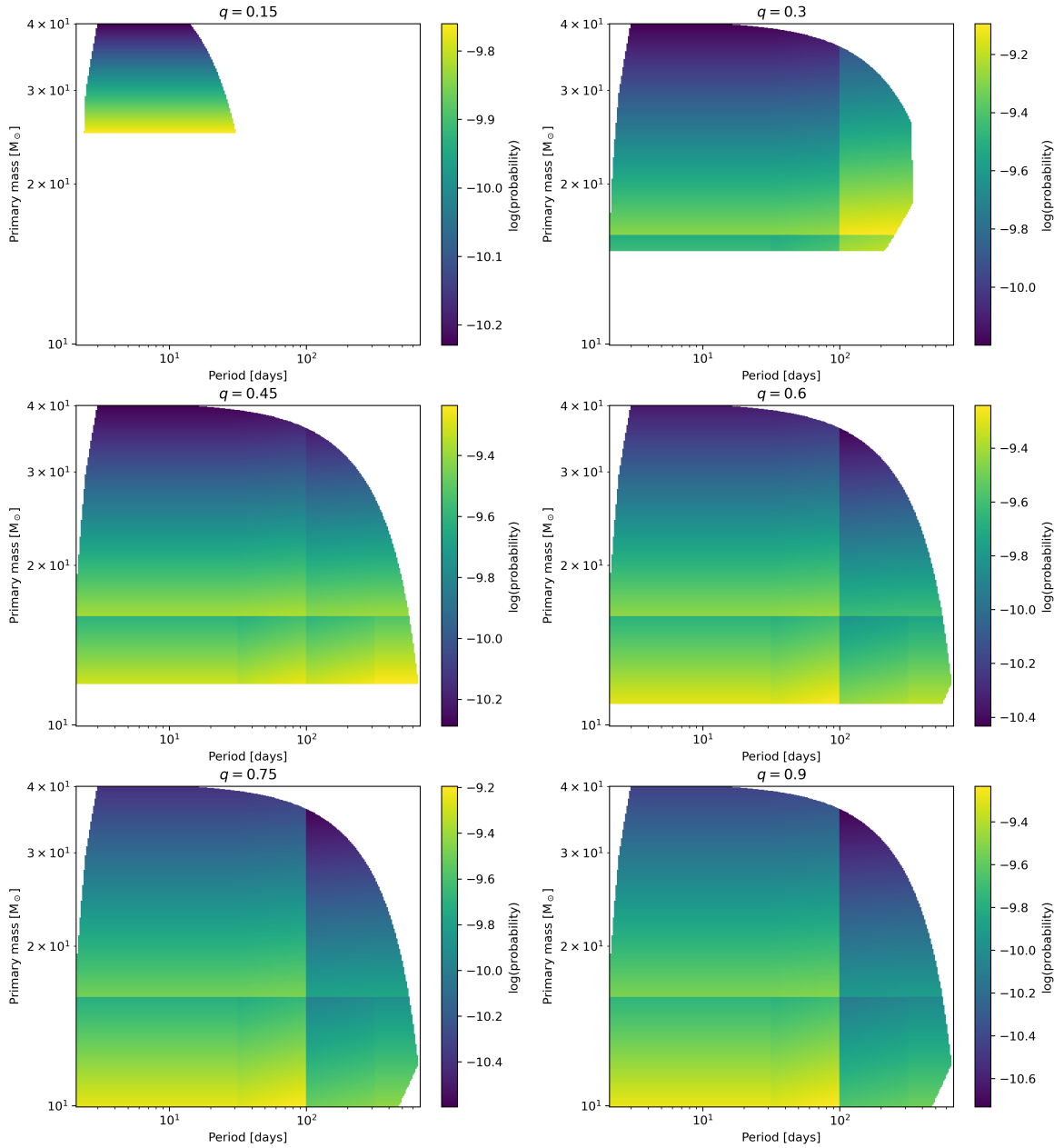


Figure C.1: The interpolation space used for calculating the expected yields for the alpha-enhanced runs. On the x -axis is the initial orbital period. On the y -axis is the initial primary mass. Both are in log-scale. From left to right, then from top to bottom, each slice corresponds to an increasing mass ratio, q . The coloured areas are within the interpolation bounds. Colour corresponds the probability associated with the grid volume shown, indicated by the colour bar.

Bibliography

Adamo A., et al., 2020a, *Space Sci. Rev.*, 216, 69

Adamo A., et al., 2020b, *MNRAS*, 499, 3267

Adamo A., Usher C., Pfeffer J., Claeysens A., 2023, *MNRAS*, 525, L6

Adelberger E. G., et al., 2011, *Reviews of Modern Physics*, 83, 195

Agüeros M. A., et al., 2018, *ApJ*, 862, 33

Aguilera-Gómez C., Monaco L., Mucciarelli A., Salaris M., Villanova S., Pancino E., 2022, *A&A*, 657, A33

Angulo C., 1999, in *Experimental Nuclear Physics in europe: Facing the next millennium.* pp 365–366, doi:10.1063/1.1301821

Asplund M., Grevesse N., Sauval A. J., Allende Prieto C., Kiselman D., 2004, *A&A*, 417, 751

Asplund M., Grevesse N., Sauval A. J., Scott P., 2009, *ARA&A*, 47, 481

Baklanov P. V., Blinnikov S. I., Pavlyuk N. N., 2005, *Astronomy Letters*, 31, 429

Banerjee S., 2021, *MNRAS*, 500, 3002

- Banerjee S., Belczynski K., Fryer C. L., Berczik P., Hurley J. R., Spurzem R., Wang L.,
2020, *A&A*, 639, A41
- Baraffe I., Chabrier G., Allard F., Hauschildt P. H., 1998, *A&A*, 337, 403
- Bastian N., Lardo C., 2018, *ARA&A*, 56, 83
- Bastian N., Pfeffer J., 2022, *MNRAS*, 509, 614
- Bastian N., Cabrera-Ziri I., Salaris M., 2015, *MNRAS*, 449, 3333
- Baumgardt H., Hénault-Brunet V., Dickson N., Sollima A., 2023, *Monthly Notices of the
Royal Astronomical Society*, 521, 3991
- Bekki K., 2017, *MNRAS*, 469, 2933
- Binks A. S., et al., 2022, *MNRAS*, 513, 5727
- Blinnikov S., Sorokina E., 2004, *Ap&SS*, 290, 13
- Blinnikov S. I., Röpké F. K., Sorokina E. I., Gieseler M., Reinecke M., Travaglio C.,
Hillebrandt W., Stritzinger M., 2006, *A&A*, 453, 229
- Böhm-Vitense E., 1958, *ZAp*, 46, 108
- Bonaca A., et al., 2020, *ApJ*, 897, L18
- Bressan A., Marigo P., Girardi L., Salasnich B., Dal Cero C., Rubele S., Nanni A., 2012,
MNRAS, 427, 127
- Brown G., Gnedin O. Y., 2022, *MNRAS*, 514, 280
- Brown J. M., Garaud P., Stellmach S., 2013, *ApJ*, 768, 34

Bruzual G., Charlot S., 2003, MNRAS, 344, 1000

Buzzo M. L., Forbes D. A., Brodie J. P., Janssens S. R., Couch W. J., Romanowsky A. J., Gannon J. S., 2023, MNRAS, 522, 595

Cabrera-Ziri I., et al., 2015, Monthly Notices of the Royal Astronomical Society, 448, 2224

Cadelano M., Dalessandro E., Salaris M., Bastian N., Mucciarelli A., Saracino S., Martocchia S., Cabrera-Ziri I., 2022, ApJ, 924, L2

Cai M. X., Portegies Zwart S., Kouwenhoven M. B. N., Spurzem R., 2019, MNRAS, 489, 4311

Cameron A. G. W., Fowler W. A., 1971, ApJ, 164, 111

Carretta E., 2019, A&A, 624, A24

Carretta E., Bragaglia A., 2021, A&A, 646, A9

Carretta E., Gratton R. G., 1997, A&AS, 121, 95

Carretta E., et al., 2015, A&A, 578, A116

Carroll B. W., Ostlie D. A., 2017, An introduction to modern astrophysics, Second Edition

Cassisi S., Salaris M., 2020, A&A Rev., 28, 5

Castrillo A., et al., 2021, MNRAS, 501, 3122

Chabrier G., 2003, PASP, 115, 763

Chandar R., Fall S. M., Whitmore B. C., Mulia A. J., 2017, ApJ, 849, 128

Chantereau W., Charbonnel C., Meynet G., 2016, A&A, 592, A111

Charbonneau P., 1992, *A&A*, 259, 134

Charbonnel C., Chantereau W., Decressin T., Meynet G., Schaerer D., 2013, *A&A*, 557, L17

Choi J., Dotter A., Conroy C., Cantiello M., Paxton B., Johnson B. D., 2016, *ApJ*, 823, 102

Cournoyer-Cloutier C., et al., 2021, *MNRAS*, 501, 4464

Cournoyer-Cloutier C., et al., 2023, *MNRAS*, 521, 1338

Cox J. P., Giuli R. T., 1968, *Principles of stellar structure*

Cyburt R. H., Fields B. D., Olive K. A., 2008, *J. Cosmology Astropart. Phys.*, 2008, 012

Cyburt R. H., et al., 2010, *The Astrophysical Journal Supplement Series*, 189, 240

Cyburt R. H., Fields B. D., Olive K. A., Yeh T.-H., 2016, *Reviews of Modern Physics*, 88, 015004

D’Antona F., Ventura P., 2010, in Charbonnel C., Tosi M., Primas F., Chiappini C., eds, Vol. 268, *Light Elements in the Universe*. pp 395–404 (arXiv:1002.2037), doi:10.1017/S1743921310004527

D’Antona F., et al., 2022, *ApJ*, 925, 192

D’Ercole A., D’Antona F., Ventura P., Vesperini E., McMillan S. L. W., 2010, *MNRAS*, 407, 854

Decressin T., Meynet G., Charbonnel C., Prantzos N., Ekström S., 2007a, *A&A*, 464, 1029

Decressin T., Charbonnel C., Meynet G., 2007b, *A&A*, 475, 859

- Decressin T., Charbonnel C., Siess L., Palacios A., Meynet G., Georgy C., 2009, *A&A*, 505, 727
- Deger S., et al., 2022, *MNRAS*, 510, 32
- Demarque P., Woo J.-H., Kim Y.-C., Yi S. K., 2004, *ApJS*, 155, 667
- Denissenkov P. A., Herwig F., 2003, *ApJ*, 590, L99
- Dickson N., Hénault-Brunet V., Baumgardt H., Gieles M., Smith P. J., 2023, *MNRAS*, 522, 5320
- Dietz M., et al., 2023, in *European Physical Journal Web of Conferences*. p. 01017, doi:10.1051/epjconf/202328401017
- Doherty C. L., Gil-Pons P., Lau H. H. B., Lattanzio J. C., Siess L., Campbell S. W., 2014, *MNRAS*, 441, 582
- Dotter A., 2016, *ApJS*, 222, 8
- Dotter A., Chaboyer B., Jevremović D., Kostov V., Baron E., Ferguson J. W., 2008, *ApJS*, 178, 89
- Duchêne G., Kraus A., 2013, *ARA&A*, 51, 259
- Eggleton P. P., 1983, *ApJ*, 268, 368
- Eggleton P., 2011, *Evolutionary Processes in Binary and Multiple Stars*
- Ekström S., et al., 2012, *A&A*, 537, A146
- Eldridge J. J., Stanway E. R., 2009, *MNRAS*, 400, 1019

- Eldridge J. J., Fraser M., Smartt S. J., Maund J. R., Crockett R. M., 2013, *MNRAS*, 436, 774
- Erbacher P., et al., 2023, in *European Physical Journal Web of Conferences*. p. 06005, doi:10.1051/epjconf/202327906005
- Ernandes H., Barbuy B., Alves-Brito A., Friaça A., Siqueira-Mello C., Allen D. M., 2018, *A&A*, 616, A18
- Fabry M., Marchant P., Sana H., 2022, *A&A*, 661, A123
- Fabry M., Marchant P., Langer N., Sana H., 2023, *A&A*, 672, A175
- Farmer R., Laplace E., de Mink S. E., Justham S., 2021, *ApJ*, 923, 214
- Farmer R., Laplace E., Ma J.-z., de Mink S. E., Justham S., 2023, *ApJ*, 948, 111
- Fields B. D., Olive K. A., 2022, *J. Cosmology Astropart. Phys.*, 2022, 078
- Forbes D. A., et al., 2018, *Proceedings of the Royal Society A: Mathematical, Physical and Engineering Sciences*, 474, 20170616
- Gieles M., et al., 2018, *MNRAS*, 478, 2461
- Glebbeeck E., Gaburov E., de Mink S. E., Pols O. R., Portegies Zwart S. F., 2009, *A&A*, 497, 255
- Goudfrooij P., Girardi L., Correnti M., 2017, *ApJ*, 846, 22
- Gratton R. G., et al., 2013, *A&A*, 549, A41
- Gratton R., Bragaglia A., Carretta E., D’Orazi V., Lucatello S., Sollima A., 2019, *A&A Rev.*, 27, 8

- Gvozdenko A., Larsen S. S., Beasley M. A., Brodie J., 2022, *A&A*, 666, A159
- Hamers A. S., Glanz H., Neunteufel P., 2022, *ApJS*, 259, 25
- Harris W. E., 1996, *AJ*, 112, 1487
- Harris C. R., et al., 2020, *Nature*, 585, 357
- Heger A., Langer N., Woosley S. E., 2000, *ApJ*, 528, 368
- Heger A., Woosley S. E., Spruit H. C., 2005, *ApJ*, 626, 350
- Heggie D. C., 1975, *MNRAS*, 173, 729
- Heney L., Vardya M. S., Bodenheimer P., 1965, *ApJ*, 142, 841
- Herwig F., 2000, *A&A*, 360, 952
- Hidalgo S. L., et al., 2018, *ApJ*, 856, 125
- Hopkins P. F., 2012, *Monthly Notices of the Royal Astronomical Society*, 428, 1950
- Howard C. S., Pudritz R. E., Sills A., Harris W. E., 2019, *MNRAS*, 486, 1146
- Huerta-Martinez E., Gavetti C., Ventura P., 2023, *Universe*, 9, 84
- Hurley J. R., Tout C. A., Pols O. R., 2002, *MNRAS*, 329, 897
- Iglesias C. A., Rogers F. J., 1993, *ApJ*, 412, 752
- Iglesias C. A., Rogers F. J., 1996, *ApJ*, 464, 943
- Jang S., et al., 2022, *MNRAS*, 517, 5687
- Jermyn A. S., et al., 2023, *ApJS*, 265, 15

- Jiménez S., Tenorio-Tagle G., Silich S., 2021, MNRAS, 505, 4669
- Johnson C. I., Rich R. M., Pilachowski C. A., Caldwell N., Mateo M., Bailey John I. I., Crane J. D., 2015, AJ, 150, 63
- Joyce M., Tayar J., 2023, Galaxies, 11, 75
- Keller B. W., Kruijssen J. M. D., 2022, MNRAS, 512, 199
- Kippenhahn R., Ruschenplatt G., Thomas H. C., 1980, A&A, 91, 175
- Koch A., Côté P., 2019, A&A, 632, A55
- Krause M. G. H., et al., 2020, Space Sci. Rev., 216, 64
- Kroupa P., 2001, MNRAS, 322, 231
- Kroupa P., Weidner C., 2003, ApJ, 598, 1076
- Krumholz M., McKee C., Bland-Hawthorn J., 2019, ARA&A, 57, 223
- Kullmann I., Goriely S., Just O., Bauswein A., Janka H. T., 2023, MNRAS, 523, 2551
- Kummer F., Toonen S., de Koter A., 2023, arXiv e-prints, p. arXiv:2306.09400
- Lahén N., Naab T., Johansson P. H., Elmegreen B., Hu C.-Y., Walch S., Steinwandel U. P., Moster B. P., 2020, ApJ, 891, 2
- Lahén N., et al., 2023, MNRAS, 522, 3092
- Langer G. E., Hoffman R., Sneden C., 1993, PASP, 105, 301
- Lapenna E., et al., 2016, ApJ, 826, L1

- Larsen S. S., Eitner P., Magg E., Bergemann M., Moltzer C. A. S., Brodie J. P., Romanowsky A. J., Strader J., 2022, *A&A*, 660, A88
- Leja J., Speagle J. S., Johnson B. D., Conroy C., van Dokkum P., Franx M., 2020, *ApJ*, 893, 111
- Li C., de Grijs R., Deng L., Milone A. P., 2017, *ApJ*, 844, 119
- Li C., Wang Y., Milone A. P., 2019, *ApJ*, 884, 17
- Lu W., Fuller J., Quataert E., Bonnerot C., 2023, *MNRAS*, 519, 1409
- Lurie J. C., et al., 2017, *AJ*, 154, 250
- Magrini L., et al., 2018, *A&A*, 617, A106
- Marchant P., Pappas K. M. W., Gallegos-Garcia M., Berry C. P. L., Taam R. E., Kalogera V., Podsiadlowski P., 2021, *A&A*, 650, A107
- Marino A. F., et al., 2019, *MNRAS*, 487, 3815
- Martocchia S., et al., 2018, *MNRAS*, 477, 4696
- Masseron T., et al., 2019, *A&A*, 622, A191
- McKenzie M., Bekki K., 2018, *MNRAS*, 479, 3126
- McKenzie M., Bekki K., 2021, *MNRAS*, 507, 834
- Mészáros S., et al., 2020, *MNRAS*, 492, 1641
- Meynet G., Maeder A., 1997, *A&A*, 321, 465
- Meynet G., Maeder A., 2000, *A&A*, 361, 101

Milone A. P., Marino A. F., 2022, *Universe*, 8, 359

Milone A. P., et al., 2012a, *A&A*, 540, A16

Milone A. P., et al., 2012b, *ApJ*, 744, 58

Milone A. P., et al., 2017, *MNRAS*, 464, 3636

Milone A. P., et al., 2018, *MNRAS*, 481, 5098

Milone A. P., et al., 2023, *MNRAS*, 522, 2429

Moe M., Di Stefano R., 2017, *ApJS*, 230, 15

Molero M., Magrini L., Matteucci F., Romano D., Palla M., Cescutti G., Viscasillas Vázquez C., Spitoni E., 2023, *MNRAS*, 523, 2974

Monelli M., et al., 2013, *Monthly Notices of the Royal Astronomical Society*, 431, 2126

Monty S., et al., 2023, *MNRAS*, 522, 4404

Muñoz C., et al., 2018, *A&A*, 620, A96

Muñoz C., et al., 2020, *MNRAS*, 492, 3742

Nandakumar G., et al., 2022, *MNRAS*, 513, 232

Nogueras-Lara F., et al., 2020, *Nature Astronomy*, 4, 377

Norris J. E., Yong D., Frebel A., Ryan S. G., 2023, *MNRAS*, 522, 1358

Nugis T., Lamers H. J. G. L. M., 2000, *A&A*, 360, 227

Offner S. S. R., Moe M., Kratter K. M., Sadavoy S. I., Jensen E. L. N., Tobin J. J., 2023, in Inutsuka S., Aikawa Y., Muto T., Tomida K., Tamura M., eds, *Astronomical Society of the Pacific Conference Series Vol. 534*, Astronomical Society of the Pacific Conference Series. p. 275

Oliveira R. A. P., et al., 2020, *ApJ*, 891, 37

Paxton B., Bildsten L., Dotter A., Herwig F., Lesaffre P., Timmes F., 2011, *ApJS*, 192, 3

Paxton B., et al., 2013, *ApJS*, 208, 4

Paxton B., et al., 2015, *ApJS*, 220, 15

Paxton B., et al., 2018, *ApJS*, 234, 34

Paxton B., et al., 2019, *ApJS*, 243, 10

Perktold J., et al., 2023, statsmodels/statsmodels: Release 0.14.0, doi:10.5281/zenodo.7899735, <https://doi.org/10.5281/zenodo.7899735>

Petrovic J., Langer N., van der Hucht K. A., 2005, *A&A*, 435, 1013

Pignatari M., Gallino R., Heil M., Wiescher M., Käppeler F., Herwig F., Bisterzo S., 2010, *ApJ*, 710, 1557

Piotto G., 2009, in Mamajek E. E., Soderblom D. R., Wyse R. F. G., eds, Vol. 258, *The Ages of Stars*. pp 233–244, doi:10.1017/S1743921309031883

Portegies Zwart S. F., McMillan S. L. W., Gieles M., 2010, *ARA&A*, 48, 431

Rain M. J., Villanova S., Muñoz C., Valenzuela-Calderon C., 2019, *MNRAS*, 483, 1674

Ramírez I., Meléndez J., 2005, *ApJ*, 626, 465

Ramírez I., Allende Prieto C., Lambert D. L., 2013, *ApJ*, 764, 78

Randich S., Magrini L., 2021, *Frontiers in Astronomy and Space Sciences*, 8, 6

Reddy B. E., Lambert D. L., Allende Prieto C., 2006, *MNRAS*, 367, 1329

Reina-Campos M., Kruijssen J. M. D., Pfeffer J., Bastian N., Crain R. A., 2018, *MNRAS*, 481, 2851

Renzini A., 2008, *Monthly Notices of the Royal Astronomical Society*, 391, 354

Renzini A., Marino A. F., Milone A. P., 2022, *MNRAS*, 513, 2111

Ritter H., 1988, *A&A*, 202, 93

Ritter C., Herwig F., Jones S., Pignatari M., Fryer C., Hirschi R., 2018, *MNRAS*, 480, 538

Rizzuti F., Hirschi R., Arnett W. D., Georgy C., Meakin C., Murphy A. S., Rauscher T., Varma V., 2023, *Monthly Notices of the Royal Astronomical Society*, 523, 2317

Roediger J. C., Courteau S., Graves G., Schiavon R. P., 2014, *ApJS*, 210, 10

Rui N. Z., Kremer K., Weatherford N. C., Chatterjee S., Rasio F. A., Rodriguez C. L., Ye C. S., 2021, *ApJ*, 912, 102

Rybicki G. B., Lightman A. P., 1979, *Radiative processes in astrophysics*

Salgado C., Da Costa G. S., Yong D., Salinas R., Norris J. E., Mackey A. D., Marino A. F., Milone A. P., 2022, *MNRAS*, 515, 2511

Salpeter E. E., 1955, *ApJ*, 121, 161

Sana H., 2022, in Decin L., Zijlstra A., Gielen C., eds, Vol. 366, The Origin of Outflows in Evolved Stars. pp 83–95 (arXiv:2203.16332), doi:10.1017/S1743921322001090

Sana H., et al., 2012, *Science*, 337, 444

Saracino S., et al., 2020, *MNRAS*, 493, 6060

Schiappacasse-Ulloa J., Lucatello S., 2023, *MNRAS*, 520, 5938

Scholz F. W., Stephens M. A., 1987, *Journal of the American Statistical Association*, 82, 918

Sekiguchi M., Fukugita M., 2000, *AJ*, 120, 1072

Sen K., et al., 2022, *A&A*, 659, A98

Shao Y., Li X.-D., 2016, *ApJ*, 833, 108

Shenar T., et al., 2022, *A&A*, 665, A148

Sills A., Glebbeek E., 2010, *MNRAS*, 407, 277

Simpson J. D., Cottrell P. L., Worley C. C., 2012, *MNRAS*, 427, 1153

Skowronski J., et al., 2023, *Phys. Rev. C*, 107, L062801

Smith N., 2014, *ARA&A*, 52, 487

Squicciarini V., Gratton R., Bonavita M., Mesa D., 2021, *MNRAS*, 507, 1381

Tacchella S., et al., 2023, *MNRAS*, 522, 6236

Tang B., et al., 2021, *ApJ*, 908, 220

Tayar J., Joyce M., 2022, ApJ, 935, L30

Temmink K. D., Pols O. R., Justham S., Istrate A. G., Toonen S., 2023, A&A, 669, A45

Thygesen A. O., et al., 2016, A&A, 588, A66

Torniamenti S., Ballone A., Mapelli M., Gaspari N., Di Carlo U. N., Rastello S., Giacobbo N., Pasquato M., 2021, MNRAS, 507, 2253

Valle G., Dell’Omodarme M., Tognelli E., 2022, A&A, 658, A141

VandenBerg D. A., 2023, MNRAS, 518, 4517

Ventura P., Di Criscienzo M., Carini R., D’Antona F., 2013, MNRAS, 431, 3642

Ventura P., D’Antona F., Imbriani G., Di Criscienzo M., Dell’Agli F., Tailo M., 2018, MNRAS, 477, 438

Vink J. S., de Koter A., Lamers H. J. G. L. M., 2001, A&A, 369, 574

Virtanen P., et al., 2020, Nature Methods, 17, 261

Wang C., Langer N., Schootemeijer A., Castro N., Adscheid S., Marchant P., Hastings B., 2020, ApJ, 888, L12

Wang L., Tanikawa A., Fujii M. S., 2022, MNRAS, 509, 4713

Wang Y., Tang B., Li C., Baumgardt H., Muñoz R. R., Fernández-Trincado J. G., Geisler D., Fang Y., 2023, ApJ, 943, 86

Winter A. J., Clarke C. J., 2023, MNRAS, 521, 1646

Wirth H., Jerabkova T., Yan Z., Kroupa P., Haas J., Šubr L., 2021, MNRAS, 506, 4131

Ying J. M., Chaboyer B., Boudreaux E. M., Slaughter C., Boylan-Kolchin M., Weisz D.,
2023, AJ, 166, 18

Yong D., Grundahl F., Nissen P. E., Jensen H. R., Lambert D. L., 2005, A&A, 438, 875

Yong D., Grundahl F., Norris J. E., 2015, MNRAS, 446, 3319

Yoon S. C., Langer N., Norman C., 2006, A&A, 460, 199

da Silva A. R., Smiljanic R., 2023, arXiv e-prints, p. arXiv:2307.03588

de Jager C., Nieuwenhuijzen H., van der Hucht K. A., 1988, A&AS, 72, 259

de Mink S., Pols O., Langer N., Izzard R., 2009, A&A, 507

de Wit, W. J. Testi, L. Palla, F. Zinnecker, H. 2005, A&A, 437, 247

di Criscienzo M., Ventura P., D'Antona F., Milone A., Piotto G., 2010, MNRAS, 408, 999